Engineering of impurity doped regions in semiconducting $BaSi_2$ by MBE for thin film Solar cells Application

Muhammad Ajmal Khan

February 2013

Engineering of impurity doped regions in semiconducting $BaSi_2$ by MBE for thin film Solar cells Application

Muhammad Ajmal Khan

Doctorial Program in Applied Physics

Submitted to the Graduate School of

Pure and Applied Sciences

in Partial Fulfillment of the Requirements

for the Degree of Doctor of Philosophy in

Engineering

at the

University of Tsukuba

I certify that I have read this dissertation and that in my opinion it is fully adequate, in scope and quality, as dissertation for the degree of Doctor of Philosophy in Engineering.

末益 崇

Takashi SUEMASU, Principal Advisor

I certify that I have read this dissertation and that in my opinion it is fully adequate, in scope and quality, as dissertation for the degree of Doctor of Philosophy in Engineering.

K. Akimoto

Katsuhiro AKIMOTO, Examiner

I certify that I have read this dissertation and that in my opinion it is fully adequate, in scope and quality, as dissertation for the degree of Doctor of Philosophy in Engineering.

関口 隆史

Takashi SEKIGUCHI, Examiner

I certify that I have read this dissertation and that in my opinion it is fully adequate, in scope and quality, as dissertation for the degree of Doctor of Philosophy in Engineering.

Kazuhiro Marumoto

Kazuhiro MARUMOTO, Examiner

I certify that I have read this dissertation and that in my opinion it is fully adequate, in scope and quality, as dissertation for the degree of Doctor of Philosophy in Engineering.

今井 基晴

Motoharu IMAI, Examiner

Approved for the University Committee on Graduate Studies.

ABSTRACT

Materials for low cost, eco-friendly, and high efficiency solar cell applications have become of great importance. $BaSi_2$ semiconducting material has a large optical absorption coefficient of over 3×10^4 cm^{-1} at 1.5 eV, as compared to crystalline Si, and more than 25% efficiency is expected for a single *p-n* junction solar cell. These features and advantages of $BaSi_2$ qualify it as a novel material in fabricating *p-n* junction diodes for the formation of thin film solar cells. The *p-n* junction diodes can be formed by impurity doping, where the electric field around the *p-n* junction can separate the photo excited electron-hole pairs for photovoltaic power generation.

This dissertation demonstrates the engineering of impurity doped regions for *p-n* junctions of $BaSi_2$ for application to thin film solar cells. The results will be beneficial to the design of multi-junction solar cells in the near future and the improvement of the solar cell module conversion efficiency at low cost. Impurity type from group 13 and 15 of the periodic table, like, indium (In), antimony (Sb), gallium (Ga), and aluminum (Al), have already been attempted as potential doping candidates for the formation of $BaSi_2$ *p-n* structure. Among these candidates, epitaxial growth of Sb, Ga, and In-doped *n*(*p*)-$BaSi_2$ were achieved successfully by MBE growth. The hole concentration was limited up to 10^{17} cm^{-3} at room temperature (RT) in In and Al -doped $BaSi_2$ layers. In contrast, the electron concentration of Sb-doped $BaSi_2$ was controlled in the range between 10^{17} and 10^{20} cm^{-3} at RT by changing the temperature of the Sb Knudsen cell crucible. After achieving this, the remaining process was the formation of *p*-type $BaSi_2$ on the undoped *n*-type $BaSi_2$ layer (n=5×10^{15} cm^{-3}) to complete the $BaSi_2$ *p-n* junction diode. Copper (Cu), silver (Ag) and boron (B) are attractive *n*-type or *p*-type impurity candidates to fabricate *n*(n^+)-layer and *p*(p^+)-layer of *p-n* junction including tunnel junction (TJ) of $BaSi_2$ thin film solar cells.

In-situ epitaxial growth, crystalline quality, depth profiles of impurity atoms and comprehensive studies about electrical characterization of Cu and Ag-doped $BaSi_2$ were carried out. It was found that Cu atoms do not show any segregation tendency even when the Cu-doped $BaSi_2$ layers were embedded in the $BaSi_2$ over layers. The electron concentration in Cu-doped $BaSi_2$ remained unchanged, even when the Cu temperature was increased to 950 °C, but increased sharply to 10^{20} cm^{-3} around 1000 °C. These results suggest that control of electron concentrations in Cu-doped $BaSi_2$ is difficult. This is probably due to the fact that the insertion site of Cu atoms in $BaSi_2$ is an interstitial site. Hall measurements show that the hole density increases gradually from 3×10^{15} to 3×10^{16} cm^{-3} with increasing Ag-source temperature, showing that the hole concentrations can be controlled. However, a heavily doped *p*-type layer was necessary for $BaSi_2$.

In this dissertation some remaining and important research problems associated with Sb-doped $BaSi_2$ *n*(n^+)-layer of $BaSi_2$ are further tackled, like confirmation of ohmic behavior even at low temperatures and the negative differential resistance (NDR) effect across the TJ of Sb-doped n^+-$BaSi_2$/p^+-Si as a function of temperature. The Hall measurement at low temperature revealed a donor energy level (E_D) of 47 meV.

In order to quantify the defect level in the impurity doped-$BaSi_2$, the transport mechanisms of the carriers are reported in this dissertation. The temperature dependence of resistivity indicated that the carrier transport in Ga, Al, Ag, and Cu-doped $BaSi_2$ can be well explained by both SE-and Mott-type variable-range hopping (VRH) conduction. In contrast, temperature dependent resistivity in Sb, In and

B-doped $BaSi_2$ gives a non-linear behavior, which confirms that the carrier transport could not be explained by SE-& Mott-type VRH hopping conduction mechanism.

Next, investigated in detail, was the process to achieve p^+-layer of $BaSi_2$ with boron (B)-impurity as a dopant. We have successfully grown *a*-axis-oriented lightly, moderately and heavily B-doped $p(p^+)$-type $BaSi_2$ films on Si(111) by MBE growth. SIMS measurements show that the average B concentration, N_B for $BaSi_2$ prepared with B-source temperature T_B at 1350 °C is approximately 3×10^{20} cm^{-3}, while that at 1450 °C is 2×10^{21} cm^{-3} and at 1550 °C is approximately 1×10^{22} cm^{-3}. This result is explained relatively well by the difference in vapor pressure of B. The vapor pressure of B at 1550 °C is approximately 7 times larger than that at 1450 °C. These results indicate that the concentration of B-atoms in a $BaSi_2$ substrate can be controlled by manipulating T_B. Hole concentration was found to be in the range of 10^{16} to $2\times10^{20}cm^{-3}$ with increasing T_B and varying growth temperature, while T_S was controlled for the first time after RTA treatment. The acceptor level was estimated to be approximately 23 meV. However, during TEM observation the B-clusters having sizes of 3-5 nm were found. The grain size in the $BaSi_2$ films was found to be approximately 0.5 μm, which is the highest value ever reported for doped-$BaSi_2$.

TEM observation revealed precipitation of B-atoms and that B-atoms were not fully activated in the $BaSi_2$. Therefore, we tested many samples through substrate temperature optimization like 650 °C in the MBE, keeping T_B around 1350 to 1380 °C. From this we found new growth conditions that give precipitation-free B-doped $BaSi_2$ grown layers. Hole concentrations in B-doped $BaSi_2$ above 10^{19} cm^{-3} at RT were achieved successfully in those samples having no diffusion and precipitation problem. The acceptor level was estimated to be approximately 20 meV. This new growth condition could possibly define the solid solubility limit of atoms in $BaSi_2$ host materials. The highest activation efficiency, exceeding 40%, was achieved successfully with this new growth condition.

By using this optimized growth condition the absorption edge of the B-doped *p*-$BaSi_2$ on the SOI substrate was found to be about 1.23 eV, yielding 0.1 eV shrinkage in band gap energy of B-doped $BaSi_2$. The new and optimized growth condition gives no segregation and diffusion tendencies toward the un-doped $BaSi_2$/Si structure.

Due to the discovery of the novel p^+-layer, the fabrication of Sb-doped $n(n^+)$-type (10^{17}-$10^{20}cm^{-3}$) and B-doped $p(p^+)$-type(10^{16}-$10^{20}cm^{-3}$) regions of the next generation *p-n* junction in $BaSi_2$ solar cells are possible. The novel p^+-layer is one step behind the practical semiconducting $BaSi_2$ solar cells *p-n* junction.

ACKNOWLEDGMENTS

First and foremost, I must thank the Almighty Allah (God) for blessing, protecting and guiding me throughout my life. This work would not have been possible without the support and prayers from a number of people. I would like to express my profound gratitude to my advisor, the honorable Professor Takashi SUEMASU, also known as a “kind sensei” to the students working with him. I thank him for creating a unique research environment that maximizes the student’s freedom to explore their own research objectives and to utilize the extensive pool of knowledge available to them in the various departments and research labs around Japan that his lab brings together. His perseverance towards ZEMI meetings and independent problem-solving skills as well as the spirit of teamwork he fosters will benefit me for the rest of my life. I will always remember his calm and relaxed nature, and the way he responds “YES! How can I help you?” He has always been caring, a source of wisdom and motivation. I am really very thankful to Almighty Allah for giving me a kind mentor like him.

I would like to thank my oral and reading committee members, the honorable professors Dr. Katsuhiro AKIMOTO, Dr. Takashi SEKIGUCHI, Dr. Kazuhiro MARUMOTO, Dr. Imai and Dr. Motoharu IMAI. Being an experimentalist, I always find their comments, questions and suggestions towards my dissertation very challenging, but I always felt very relaxed after answering their concerns. Their insightful and supportive feedback has been very helpful in shaping the final form of this work. I would especially like to thank Dr. Kaoru TOKO for his continuous guidance and demonstration of the true spirit of scientific research over the past few years. He has taught me “how to write error-free research articles for journal publication.” I would also like to express some special words of sincere thanks for Dr. M. Suzuno, Mr. Y. Matsumoto, Mr. T. Saito, Mr. K. Sadakuni, and Mr. K. Ito, who always show me the best direction for experiments as well as providing me with scientific knowledge of semiconductor devices. I thank them all, for their kind help and guidance during my earlier days in the RIBER MBE lab. I thank Mr. T. Saito and Dr. M. Suzuno for guiding me through the intimidating learning curve of becoming an MBE and Hall measurement guru, and for their friendship and support over the years.

Madam Emiko Itoh not only did a great job in keeping such a large group functional, but has also helped myself and other students far beyond her administrative responsibilities. I would like to thank past and present members of the Suemasu & Toko lab M. Takeishi, Y. Matsumoto, R. Sasaki, G. H. Lee, K. Akutsu, H. Kawakami, A. Okada, K. Toh, K. Harada, W. Du, M. Baba, T. Yaguchi, Y. Funase, T. Yoneyama, K. Nakamura, S. Koike, H. Mushu, T. Sanai, Zhang Ning, Nurul Amal, R. Takabe, N. Shimada and R. Numata. They have made my life much easier and happier at Tsukuba and I am truly grateful to their work. I also thank everyone else in the group for making it such a fun place to work. Much of the material characterization was performed in the MST corp., NIMS, Tohoku University and AIST for Advanced Materials investigation. I thank Prof. Noritaka USAMI, Dr. Hara, Mr. N. Saito and Mr. Kawabata for facilitating RTA, TEM, Spectroscopic and SIMS measurement of my samples. Among our neighbors in the Institute of Applied Physics, I would like to thank Mr. Mamiya for facilitating liquid nitrogen acquisition for our RIBER MBE chambers whenever I needed. I also give my sincere words of thanks to Miss Libby Maret and Mr. Andrew for improving the final draft of this dissertation. Kind support and sincere effort of Miss Ono Naoko will be remembered forever. Especially her contribution for WP’s volunteer activity is highly acknowledged.

It is very important to have a nice social environment outside the school and university. The city of

Tsukuba itself has taught me several good lessons and also has given me several good friends along with good experiences in social life. In Tsukuba science city, very rarely, I have felt that I am away from my home country. In this regard, I would like to thank senior PhD students Dr. Nisar Bangash, Dr. Sirzameen, Dr. Asad Jan, Dr. Tufail, Dr. Dinar, Dr. Sharif and many others whose names are not mentioned here for creating a wonderful social platform in the name of PSAJ. Inspired by the enthusiasm of TISA members, I started participating in TISA activities, and also served as a volunteer during the Great Eastern Earthquake of Japan 2011. TISA leaders Rina, Chosho-Hiro, Mami, Seioh and small brother Yusaku Fukuhara always entertained us in TISA events during the weekend after a week of tiring work. The weekends were usually the times I recharged myself by playing soccer and interacting with the friends around Tsukuba. These interactions aided in improving my cross-cultural harmony and understanding about social life. I would like to thank my sweet friends Aziz Nazaryal, Chihiro, Mari Kekuchi, Mihaela Butnariu, Israr Ali, Farrukh, Farzik and Rouitaro. These interactions helped to improve my skills as a good listener, taught me how to organize my thoughts, and phrase my points during any intellectual activity as well as presentation. I am especially grateful to Mr. Masood Hyder Hashmi and Mr. Ayub sab, who helped me a lot during my starting days in Japan.

I am grateful to my school, college and university teachers, specially, Uncle Ghualm Nabi Eistooz, Rehmatullah Ustad, Qadar Ustad, Prof. Sultan, Prof. M. Iqbal, Prof. G. Murtaza, Prof. Arshid Majid Mirza, Dr. Anisa Qamar, Dr. Hanada, Miss Ikue and Miss Mari Kikuchi. I cannot imagine my current position without the love and support from my all family members and relatives. I thank my parents, the honorable Abdur-Rehman (Baba) and respectable Kamal Bibi (Adhaka), for striving hard to provide a good education for me and their consistent moral support along with prayers. I always fall short in telling them how I feel and find it impossible to describe their support in words. If I have to mention one thing about them, among many, then I would proudly mention that my parents are very simple, honest and they taught me how to lead a good life. I would simply say, “Baba, Adhaka are great support for me!” I still remember my mother’s care, when she was suffering from consumption sickness during my childhood. She brought many cakes and cookies from Lahore city whenever she visited there. I am thankful to darling Raheela, Ahamd, Zakia, Anisa, late-Bushra, late-Muhammad, Ammar and Laima, who always show patience during my PhD research. They all are my loving dolls. My brother Ahmad Nawaz, Late-Baitullah Shaheed, Ramtahlay, Haji Sadak, G. Hyder, Mushtaq Wazir, Hassan Wazir, Tariq Wazir, Idress, Fazal, G. Muhammad, Dr. Ahmad Noor, Hayat Wazir, Abdurehman, Asif, Gulawer, Nasir, Nasir, Khan Salam, Dr. Najiba, Liaqat Ali, Dr. Inam-Ullhaq and Hafeez. I would like to thank them for guiding me throughout my life. Thank you to all my cousins for their kind support, respect and patience during my stay in Japan. My parents, cousins, and uncles are always excited to hear my success and that inspires me to perform better and be successful. I acknowledge my entire family for providing us with a very educated atmosphere in our village. Last but not the least, I would like to remember and thank my late paternal grandfather Haji Sherzaman (Mama), late parental grandmother Abai, and late maternal grandmother Gulnaseeba “Neukai” for their prayers. I strongly believe that their prayers played very important role in my life. My late relatives, Amir Mirzaman, Sakhi Marjan uncle, Shahabudin uncle, Haleema, Gohar, Luqman and Muqrameen will be remembered time again. They are not here with us anymore but their prayers are, and good memories will always be with us. Insha-Allah Taa’la.

List of Journal papers

(1) M. Ajmal Khan, K. O. Hara, W. Du, M. Baba, K. Nakamura, M. Suzuno, K. Toko, N. Usami, and T. Suemasu, "In-situ heavily p-type doping of over 10^{20} cm^{-3} in semiconducting $BaSi_2$ thin films for solar cells applications, " **Applied Physics Letters 102, 112107 (2013).**

(2) K. Nakamura, M. Baba, M. Ajmal Khan, W. Du, K. Toko, and T. Suemasu, "Lattice and grain-boundary diffusions of boron atoms in $BaSi_2$ epitaxial films on Si(111), "**Journal of Applied Physics 113 (2013) 05311.**

(3) M. Ajmal Khan, K. O. Hara, K. Nakamura, M. Baba, K. Toh, M. Suzuno, K. Toko, N. Usami, and T. Suemasu, "Molecular beam epitaxy of boron doped p-type $BaSi_2$ epitaxial films on Si(111) substrates for thin-film solar cells, " **Journal of Crystal Growth,** http://dx.doi.org/10.1016/j.jcrysgro.2012.12.153

(4) K. Nakamura, K. Toh, M. Baba, M. Ajmal Khan, W. Du, K. Toko, and T. Suemasu, "Lattice and grain-boundary diffusions of impurity atoms in $BaSi_2$ epitaxial layers grown by molecular beam epitaxy, " **Journal of Crystal Growth,** http://dx.doi.org/10.1016/j.jcrysgro.2012.12.051

(5) M. Ajmal Khan, T. Saito, K. Nakamura, M. Baba, W. Du, K. Toh, K. Toko, and T. Suemasu, "Electrical characterization and conduction mechanism of impurity-doped $BaSi_2$ films grown on Si(111) by molecular beam epitaxy, " **Thin Solid Films 522 (2012) 95.**

(6) M. Baba, K. Nakamura, W. Du, M. Ajmal Khan, S. Koike, K. Toko, N. Usami, N. Saito, N. Yoshizawa, and T. Suemasu, "Molecular Beam Epitaxy of $BaSi_2$ Films with Grain Size over 4 μm on Si(111), " **Japanese Journal of Applied Physics 51 (2012) 098003.**

(7) Weijie Du, M. Suzuno, M. Ajmal Khan, K. Toh, N. Nakamura, M. Baba, K. Toko, N.Usami, and T. Suemasu, "Improved photoresponsivity of semiconducting $BaSi_2$ epitaxial films grown on a tunnel junction for thin-film solar cells, " **Applied Physics Letters 100 (2012) 152114.**

(8) Weijie Du, T. Saito, M. Ajmal Khan, K. Toko, N. Usami, and T. Suemasu, "Effect of Solid-Phase-Epitaxy Si Layers on Suppression of Sb Diffusion from Sb-Doped n^+-$BaSi_2$/p^+-Si Tunnel Junction to Undoped $BaSi_2$ Overlayers," **Japanese Journal of Applied Physics 51 (2012) 04DP01.**

(9) M. Ajmal Khan, T. Saito, M. Takeishi, and T. Suemasu, "Molecular Beam Epitaxy of Cu-Doped $BaSi_2$ Films on Si(111) Substrate and Evaluation & Qualification of Depth Profiles of Cu Atoms for the Formation of Efficient Solar Cells," **Advanced Materials Research (Advanced Materials for Applied Science and Technology) 326 (2011) 139.**

(10) T. Suemasu, T. Saito, K. Toh, A. Okada, and M. Ajmal Khan, "Photoresponse properties of $BaSi_2$ epitaxial films grown on the tunnel junction for high-efficiency thin-film solar cells, " **Thin Solid Films 519 (2011) 8501.**

(11) M. Ajmal Khan, M. Takeishi, Y. Matsumoto, T. Saito, and T. Suemasu, "Al- and Cu-doped $BaSi_2$ films on Si(111) substrates by molecular beam epitaxy and evaluation of depth profiles of Al and Cu atoms," **Physics Procedia 11 (2011) 11.**

(12) K. Toh, T. Saito, M. Ajmal Khan, A. Okada, and T. Suemasu, "Fabrication of $BaSi_2$ films on transparent CaF_2 substrates by molecular beam epitaxy for optical characterization, " **Physics Procedia 11 (2011) 23.**

List of International Conferences

(1) (Oral) M. Ajmal Khan, T. Saito, M. Takeishi, and T. Suemasu, "Cu-doped $BaSi_2$ films on Si (111) substrate by molecular beam epitaxy and evaluation & qualification of depth profiles of Cu atoms for the formation of efficient solar cells," **8th International Bhurban Conference on Applied Sciences & Technology, OP-22, Jan. 12, 2011, Islamabad, Pakistan.**

(2) (Oral) M. Ajmal Khan, T. Saito, K. Toh, M. Baba, K. Nakamura, Du Weijie, and T. Suemasu," Optimization and control of electron and hole concentrations in Cu- and Ag-doped $BaSi_2$ grown by molecular beam epitaxy for the formation of efficient solar cells," **Asian School-Conference on Physics and Technology of Nanostructured Materials, X.25.01o, August 25, Vladivostok, Russia.**

(3) (invited**)** T. Suemasu, M. Ajmal Khan, T. Saito, K. Toh, A. Okada, M. Baba, K. Nakamura, Du Weijie and T. Sekiguchi, and N. Usami, "Operation principles of solar cells - solar radiation, material requirements, photocurrent, photoresponse, and device configuration using semiconducting silicide $BaSi_2$, **"Asian School-Conference on Physics and Technology of Nanostructured Materials, August 21-27, Vladivostok, Russia.**

(4) M. Ajmal Khan, T. Saito, K. Nakamura, M. Baba, K. Toh, W. Du, K. Toko, N. Usami, and T. Suemasu, " Electrical characterization of Cu, Ag doped $BaSi_2$ layers on Si(111) grown by molecular beam epitaxy for thin film solar cells, " **2011 International Photovoltaic Science and Engineering Conference (PVSEC), Fukuoka, Japan, Nov.28-Dec. 2, 2011.**

(5) Weijie Du, M. Suzuno, M. Ajmal Khan, K. Toh, M. Baba, K. Nakamura, K. Toko, N. Usami, and T. Suemasu,"Improved internal quantum efficiency in high-quality $BaSi_2$ films grown by molecular beam epitaxy , " **38th IEEE Photovoltaic Specialists Conference, Austin, USA, June 5, 2012.**

(6) (Oral) M. Ajmal Khan, K O. Hara, K. Nakamura, M. Baba, K. Toh, M. Suzuno, K. Toko, N. Usami, and T. Suemasu, "Molecular beam epitaxy of boron doped p-type $BaSi_2$ epitaxial films on Si(111) substrates for thin-film solar cells, " **International Conference of Molecular Beam Epitaxy, WeA-1-2, Nara, Japan, Sept.26, 2012.**

(7) **(invited)** W. Du, M. Baba, K. Nakamura, M. Ajmal. Khan, K. Toko, N. Usami, and T. Suemasu, "Large internal quantum efficiency exceeding 70% in semiconducting $BaSi_2$ for thin-film solar cell applications, " **22th Photovoltaic Science and Engineering Conference (PVSEC), Hangzhou, China, Nov. 6, 2012.**

TABLE OF CONTENTS

LIST OF TABLES

Number ***Page***

LIST OF FIGURES

Number ***Page***

CHAPTER 1: INTRODUCTION

Environmentally friendly materials for the next generation are the primary motivation behind the green energy revolution, like thin film semiconducting $BaSi_2$ solar cells and super-mono-Si. Due to the high level of carbon emission into the atmosphere, global warming as well as deforestation, nuclear disasters, and the natural cycle of water the available energy has been badly disturbed. In order to decrease the levelized cost of electricity (LCOE) of solar power generation, there is a need for high efficiency and low manufacturing cost solar cells. Many advanced solar cell companies are focussing on high efficiency, low cost Si based thin film solar modules and hetero-junction of back contact solar modules. Therefore, the demand for low cost, high efficiency eco-friendly and safe energy resources imposes strict requirements on the choice of materials selection. As is well known, the photovoltaic industry, almost 90% of solar cells are Si-based. Among such materials semiconducting $BaSi_2$ was found to be one of the most promising candidates to fulfill desired requirements of this century. $BaSi_2$ has a simple orthorhombic structure [1,2], with the indirect band gap of approximately 1.3 eV matching the solar spectrum [3,4]. It has a large absorption coefficient of 3×10^4 cm^{-1} at 1.5 eV [5]. The key candidate for solar cells, like Si, are well known in the published literature and it is also well established that the band gap (E_g) of crystalline Si is 1.1 eV at room temperature (RT), which is approximately 0.3 eV smaller than the ideal E_g of approximately 1.4 eV [6,7]. Optical absorption measurements have shown that the E_g value of $BaSi_2$ can be increased to 1.4 eV by replacing half of the Ba atoms in $BaSi_2$ with isoelectric Sr atoms [8], which is in agreement with the theoretical result presented by Imai *et al.,* [9]. The $BaSi_2$'s conduction-band minimum and the valence-band maximum are identified to be at T(0 1/2 1/2), and around (0 1/3 0) along the Γ-Y(0 1/2 0) direction, respectively [4,9]. It is abundant in nature, having small lattice mismatch 1%, [10,11] and stable at RT. It is non-toxic material for thin film solar cells applications [12,13]. The photo responsive properties of epitaxial $BaSi_2$ layers on Si(111) and polycrystalline $BaSi_2$ layers on Si(111) layers formed on SiO_2 by the Al-induced crystallization (AIC) method have shown that $BaSi_2$ is a very promising and novel material for the formation of thin-film solar devices [14-16].

However, thin film solar cells require the fabrication of good quality of *p-n* junction diodes, where the electric field around the *p-n* junction can separate the photo excited electron-hole pairs for photovoltaic power generation. To make a *p-n* junction, we need good quality of impurity doped *n*-layer and *p*-layer regions of $BaSi_2$. One of the key fabrication processes is the incorporation of dopants into the *p-n* junction regions of thin film solar cells [6]. This chapter introduces the motivation behind this dissertation, including the need for precise and heavy doping in silicon-based $BaSi_2$ materials, and current challenges in utilizing the dopant-of-choice for *p*-type $BaSi_2$, in such structures.

Undoped $BaSi_2$ exhibits *n*-type conductivity, where the electron density is approximately 5×10^{15} cm^{-3} and the carrier mobility is 820 $cm^2/V\cdot s$ at RT [4]. However, the number of experimental reports on impurity doping of $BaSi_2$ have been quite limited so far. According to Imai and Watanabe,

substitution of Si in the $BaSi_2$ lattice is more favorable than substitution of Ba from an energetic perspective, according to first-principle calculations [17]. The electron concentration of Sb-doped *n* (n^+)-$BaSi_2$ was controlled successfully in the range from 10^{16} to 10^{20} cm^{-3} at RT [18,19]. One interesting aspect was also discovered in case of Sb-doped $BaSi_2$, where the Sb-atomic concentrations do not strongly depend on the Sb Knudsen cell temperature [18]. But the hole concentration in the *p*-layer of *p*-*n* junction of $BaSi_2$ by impurity doping like In and Al were limited up to 10^{17} cm^{-3} at RT Ref [18,20]. The remaining problem is the formation of p^+-layer of $BaSi_2$ thin film layer on the undoped *n*-$BaSi_2$ layer ($n = 5\times10^{15}$ cm^{-3}, mobility=820 cm^2/V. s) to complete the $BaSi_2$ *p*-*n* junction diode structure for solar cell operation [4].

In the few next sections the main content of the introductory part will be individually and systematically will be elaborated.

1.1 GLOBAL WARMING AND ROOT CAUSES OF ENERGY CRISES

Global warming caused by the release of greenhouse gases into the atmosphere has created an energy shortage in the world. Population explosion is another cause of the energy crises and global warming in the expanding world.

Burning of fuels like coal, natural gas and oil produces greenhouse gases in excessive amounts. The earth's temperature has risen about 1 degree Fahrenheit over the century. During the past 100 years global sea levels have risen 4 to 8 inches. The past 50 years of warming has been attributed to human activities, like driving, manufacturing, electricity generation, and clearing of forests, all of which contribute to greenhouse gas emissions and warming the planet. Such warming of the planet further caused melting of ice cap regions, which in turn causes severe non-linear weather effects like hurricanes and unpredictable weather phenomenon. Some predictions for local changes include increasingly hot summers with intense thunderstorms, draughts and other weather related phenomena, which cause increases in economic and health problems around the world [23,24]. Hence, we can say that global warming by direct or indirect means is contributing to the energy crises around the world.

In 2010, according to some reliable statistic by BP [22,26], the world proved reserve to production ratio is only 43 years for oil, 60 years for natural gas, and 119 years for coal. In addition to the limited reserves of these fossil fuels, the emission of greenhouse gases like carbon dioxide, nitrous oxide and chlorofluorocarbons (CFCs) from burning oil or coal is another critical issue to the environment. Ozone layers depletion, caused by CFCs and other toxic gases have added more miseries to human lives. These gases trap and hold infrared radiation, which gradually increases the temperature of the Earth's surface and the air in the lower atmosphere. Some evidence shows that the average global temperature has increased by about 0.6 degrees Celsius during the 20^{th} century [23,24]. Therefore it is predicted that the average global temperature will increase by 1.4 degrees to 5.8 degrees Celsius by the year 2100. The increase of global temperature will lead to significant climate problems and weather changes, affecting cloud cover, precipitation, wind patterns, the frequency and severity of storms as well as sever energy crises and the duration of the seasons. It will also cause the rising of ocean levels and extinction of some already endangered species.

To combat this scenario, we have to pursue green energy options, and it is possible that solar cells may significantly control or reduce the effect of global warming. This is because the sun radiation energy is converted into the power generation energy, while other sources for power generation may add to the global warming instead of reducing or controlling it.

1.1.1 NUCLEAR DISASTER AND EXIGENCY OF GREEN ENERGY

The nuclear accidents like "The 1986 Chernobyl accident (Russia)", and "In 1979 at Three Mile Island nuclear power plant (USA)" and "Fukushima Daiichi nuclear disaster (Japan) 2011" forced the people to think about renewable and safest green energy solutions [24,25]. The nuclear disasters not only caused serious health problems to the human being but also brought serious implications to the environment, economic conditions and eco-systems of the affected areas. The cesium and iodine are very lethal chemicals and can cause cancer. If we have more safe and clean way of energy then why, we are opting for unsafe sources of energy, like nuclear and carbon based resources.

1.1.2 THE RENEWABLE ENERGY REVOLUTION

According to the analysis of BP and Royal Dutch Shell Group [22,26], the decline of fossil fuel will started after 2020 and the clean and green energy resources like Biomass, Wind, Geo and solar cells will be the key candidates for alternatives solution of energy crises. Among these green solutions, photovoltaic could be the leading candidates, as shown in Fig. 1.

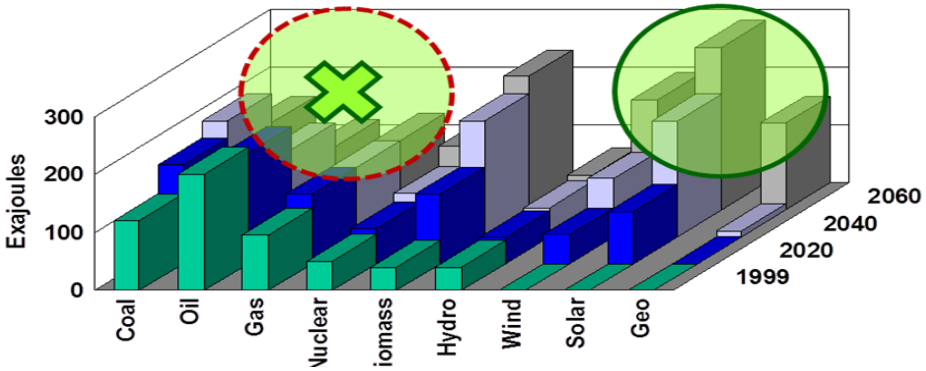

Fig. 1 gives energy in (Exajoules) as a function of available energy resources and future time (years).

According to Refs [21, 22, 25, 26,27], the renewable energy resources will achieve magnificent share in the Global Energy Market (GEM) in the next 25 years.

Possible driving forces could be:

- Falling costs for renewable energy
- Declining of fossil fuel production
- Increasing energy demand worldwide
- Environmental concerns

1.1.3 PORTFOLIO OF SOALR CELLS MATERAILS AND MODULES

As we know that the global photovoltaic (PV) product is increasing exponentially in recent years, and the total installation amount has exceeded 13 GW in 2008 and in the means while, PV industrial community faced to some short lived crises caused by world recession [27]. This means that we are

now entering the PV era and the PV will surely play an important role of the infrastructure energy sources in the near future. In order to continue with these rates of progress, we have to make even greater efforts in the fundamental and applied subjects of scientific and engineering fields in PV developments. The tremendous disaster has induced the paradigm shift in the worldwide energy system, and we have to build the new energy solutions containing photovoltaic as an indispensable one. In the current senario and with the aim to decrease LCOE [27] of solar power generation we need

- High efficiency
- Lower manafacturing Cost

Many advanced solar cell's company are focussing on:

- Si based thin film solar module for very low cost.
- Hetero-junction Back contact solar module for very high efficiency.

Figure 2 gives the trend of many kind of solar cell module efficiency (%) and module cost ($/W) [27]. Which further confirm that the PV module having low cost and high efficiency are the most important concerns of PV industrialists. Among such PV concerns, novel Si-based materials have potential interest for high-efficiency thin-film solar cells. Large absorption coefficient in $BaSi_2$ comes from its specific electronic band structure of a direct transition a few (k_BT) above the indirect band edge. Indirect band gap tends to reduce radiative recombination considerably and hence results in larger minority-carrier diffusion length. In conventional semiconductors devices, either absorption coefficient or minority-carrier diffusion length is large, or the other one tends to be small. However, we can utilize both large absorption coefficient and large minority-carrier diffusion length at the same time in $BaSi_2$ thin film solar cells.

Based on the band gap and absorption coefficient of $BaSi_2$, we expect that the thin film solar module based on Sb and B-doped *p-n* junction of $BaSi_2$ could give more than 25 % efficiency for a single junction [3,4]. This efficiency could be possibly enhanced more than 40 % by tandem structure or multi-junction solar cells.

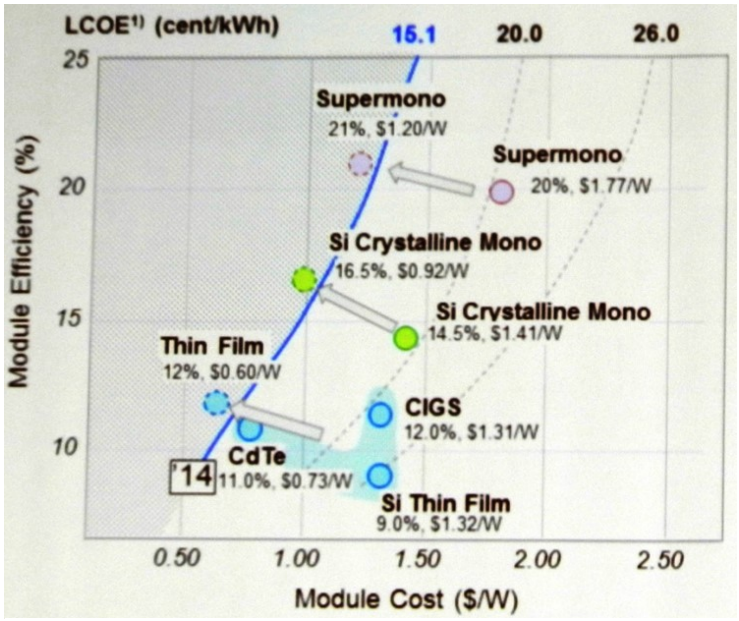

Fig. 2 solar cell module efficiency (%) vs module cost ($/W).

1.2 FEASTURES OF $BaSi_2$

1.2.1 Abundance & Absorption Co-efficient

$BaSi_2$ is safe for environment and also abundant in nature [28,13]. The Clarke number of Si(2) and Ba(14), shows that both materials are abundant in the Earth's crests, as shown in Fig.3(a).

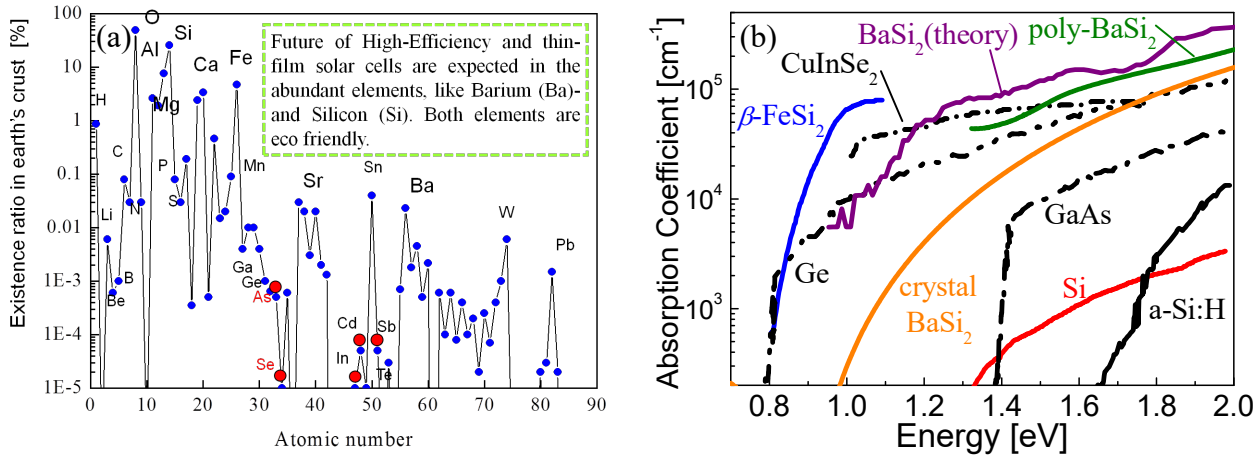

Fig. 3(a) existence ratio of elements in the earth crust vs atomic number and (b) absorption coefficient of $BaSi_2$ as a function of band gap energy.

In contrast the Clarke numbers for CIGS are Cu (26), In(66), Ga(35), S(16), and Se(69), which shows that all the materials used in CIGS are expensive, as shown in Fig. 3(a) [28].

The optical absorption coefficient reaches to $\alpha \sim 3\times10^4$ cm^{-1} at 1.5 eV, which is tens of times larger than crystalline Si, as shown in Fig. 3(b), Ref [5].

1.2.2 Ideal Band Gap and Efficiency

Semiconducting $BaSi_2$ has an ideal band gap energy Eg ~ 1.4 eV ($Ba_{0.5}Sr_{0.5}Si_2$) Ref [8]. This E_g matches the solar spectrum and indicates the possibility of a high efficiency solar cell [3-5], as shown in Figs. 4(a)-(b).

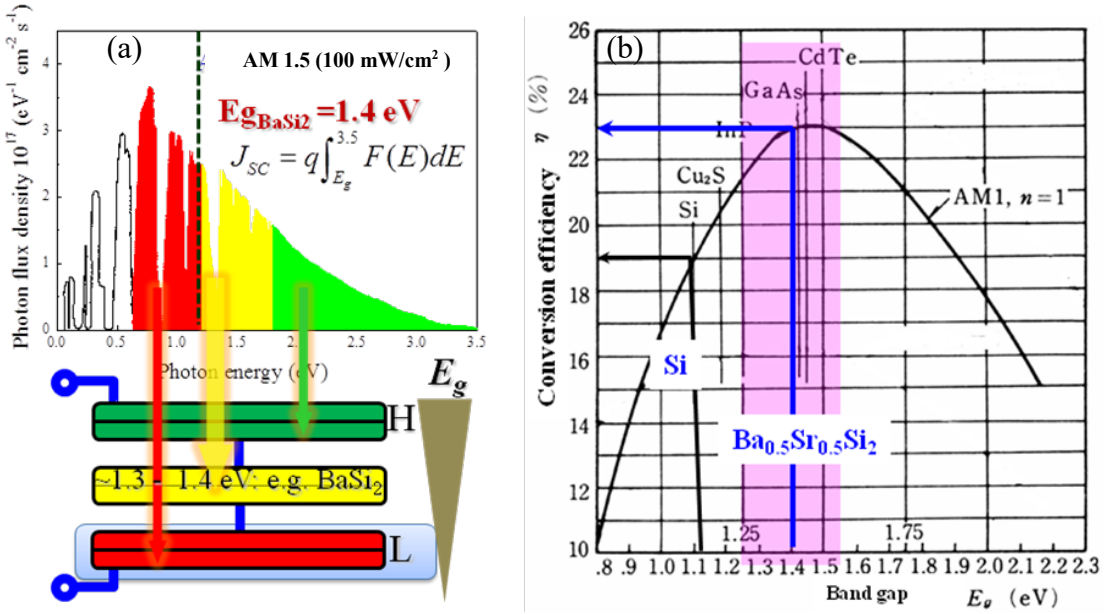

Fig. 4(a) solar spectrum as a function of photon energy (eV) and (b) gives the expected conversion efficiency as a function of Energy band gap (eV) of $BaSi_2$.

1.2.3 Crystal structure and Choice of Epitaxial growth

$BaSi_2$ has a simple orthorhombic structure, and is considered a Zintl phase (A_aX_x), where Si-Si composed of covalent bond and Ba-Si composed of ionic bond.

.

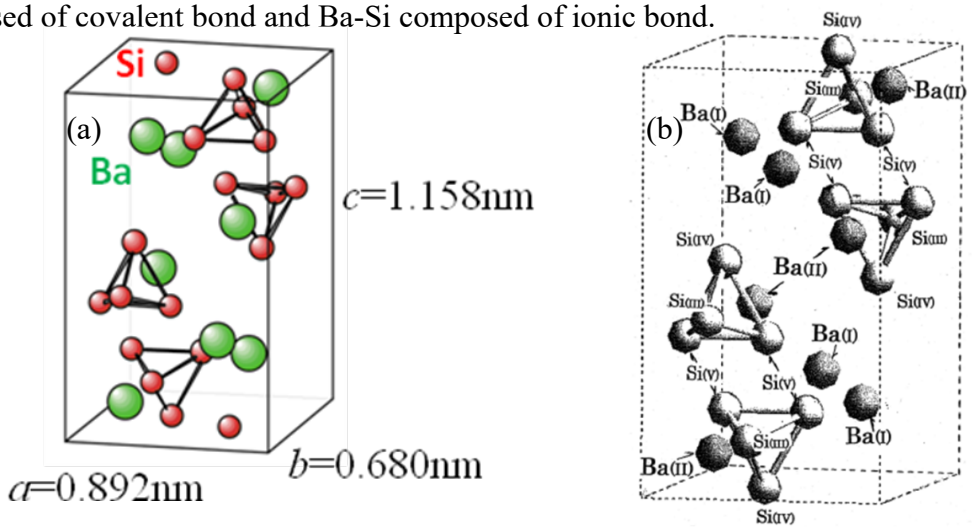

Fig. 5 shows the unit cell of an orthorhombic $BaSi_2$ crystal: where, (a) gives lattice parameters *a*, *b* and *c* of unit cell and (b) depicts different sites of Ba and Si atoms during crystallization.

The $BaSi_2$ contains 8 Ba atoms and 16 Si atoms, 80 valence electrons (2 electrons from each Ba atom and 4 electrons from each Si atom) are contained in the unit cell, as shown in Fig. 5(a).

Energetic calculation shows that the Ba atoms in site (I) will be replaced by Sr or Ca atoms more easily than those in site (II). Substitution of Ba in site (I) by Ca or Sr broadens the band gap, while substitution of Ba in site (II) by Ca or Sr narrows the gap [9]. Figure 5(b) gives various locations (sites) of Ba atoms and Si atoms in the orthorhombic $BaSi_2$ unit cell.

High-quality of *a*-axis-oriented $BaSi_2$ crystal growth on a Si(111) with lattice mismatch less than 1% is possible as shown in Fig. 6(a). Furthermore, three distinct (A, B and C-type) but crystallographically equivalent epitaxial variants at 120° are also possible, as shown in Fig. 6(b)

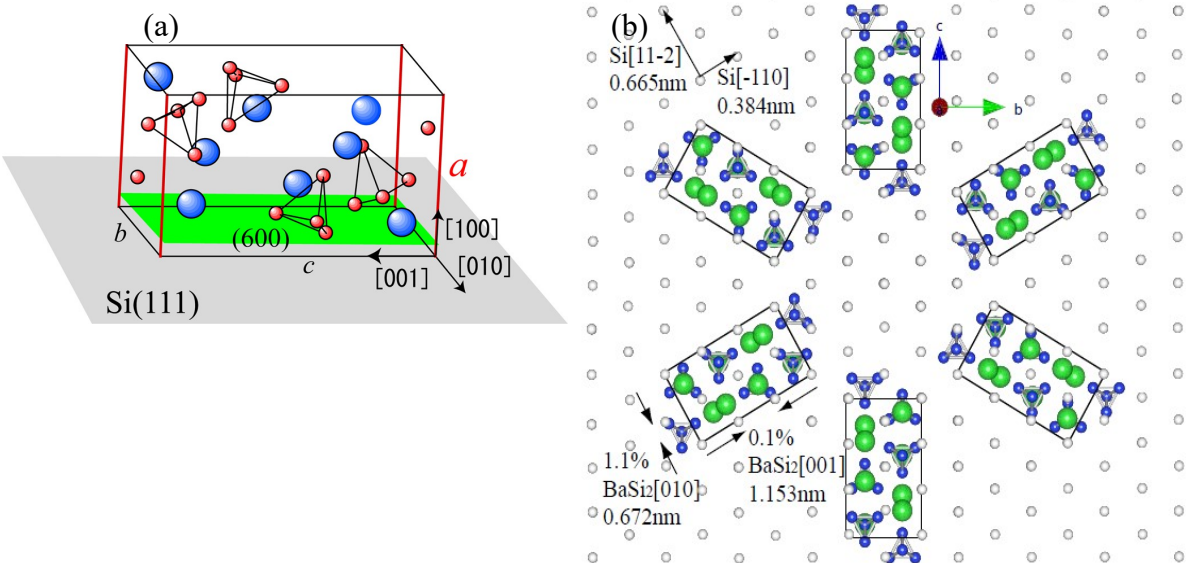

Fig. 6(a) gives *a*-axis oriented $BaSi_2$ structure on Si(111) substrate and (b) shows three distinct but crystallographically equivalent epitaxial variants of $BaSi_2$ crystal.

The photoresponse properties of epitaxial $BaSi_2$ layers on Si(111) and polycrystalline $BaSi_2$ layers on Si(111) layers formed on SiO_2 by the Al-induced crystallization (AIC) method have shown that $BaSi_2$ is a very promising and novel material for the formation of thin-film solar devices [14,15].

All the desired experiments and remaining research problems in $BaSi_2$ thin film will be accomplished by growing samples in MBE chamber. It is worthwhile to write few golden words about the comparison of the doping mechanism for ex-situ and in-situ doping into $BaSi_2$. It is necessary to compare MBE growth techniques with that of ion-implantation method. In the next section comparison of ex-situ and in-situ growth techniques are explained.

1.3 COMPARISON OF AVAILABLE IMPURITY DOPING MECHANISM AND IONIZATION ENERGY

The electrical properties of the semiconductors devices could be tailored and changed by desired level of impurity doping into the host materials. In some cases, we need some good quality of crystal and highly activated dopant atoms in the host materials. For the engineering of *n*-layer and *p*-layer of *p-n* junction, many techniques or methods could be used, like MBE, MOCVD and ion-implantation [6]. In this dissertation, MBE growth techniques for the incorporation of impurity in $BaSi_2$ thin films will be used rigorously. We will also talk about ionization energy as well as solid solubility limit of impurity doping in Si and subsequently in $BaSi_2$. Let us first discuss briefly about the ion implantation technique in the next subsection and then subsequently MBE growth technique.

1.3.1 ION-IMPLANTATION METHOD

There are several ways of introducing dopant atoms into any semiconducting host materials like Si and $BaSi_2$ lattice structure. Among these incorporation methods ion implantation is one of the possible techniques for this purpose because of its controllability and reproducibility features. But this method has its own limitation and drawbacks. In this method, impurity atoms are accelerated to certain energy level and targeted to the Si or $BaSi_2$ sample, as shown in Fig. 7. The dopant atoms collide with host atoms of the sample and eventually lose all their energy. Implantation distributes dopant atoms over a range of distances from the surface and could possible follow some statistical distribution functions depending upon the energy of the colliding dopant and the thickness of the target sample. Such collisions damage the crystalline structure of $BaSi_2$ and possibly create point defects along with amorphous regions that require post-anneal to activate the dopant and repair the damages caused by implanted atoms to the host sample. In conventional ion implantation followed by rapid thermal anneal (RTA), a dopant profile is formed that is either Gaussian as expressed by Eq. (1) or exponential, neither of which is the optimum rectangular box-shaped form.

Gaussian distribution function can be used to explain the doping profile in the host materials after ion-implantation and can be expressed as in Ref [6]:

$$N(x) = \frac{N_i}{\sqrt{2\pi}.(\Delta R)} e^{-(x-R)^2/2\Delta R^2} \qquad (1)$$

In equation 1 N_i, R and ΔR are the dose (cm^{-2}), range or depth and spread or sigma respectively.

During the annealing the dopant diffusion phenomena can be explained by the following mathematical relation (distribution function) [6]:

$$N(x,t) = \frac{N_o}{\sqrt{\pi \cdot Dt}} e^{-x^2/4Dt} \tag{2}$$

In equation 2, $N = N_d$ or N_a (cm^{-3}), N_o = dopant atoms/cm^2, t=diffusion time, and D= diffusivity, which is the approximate distance of dopant diffusion.

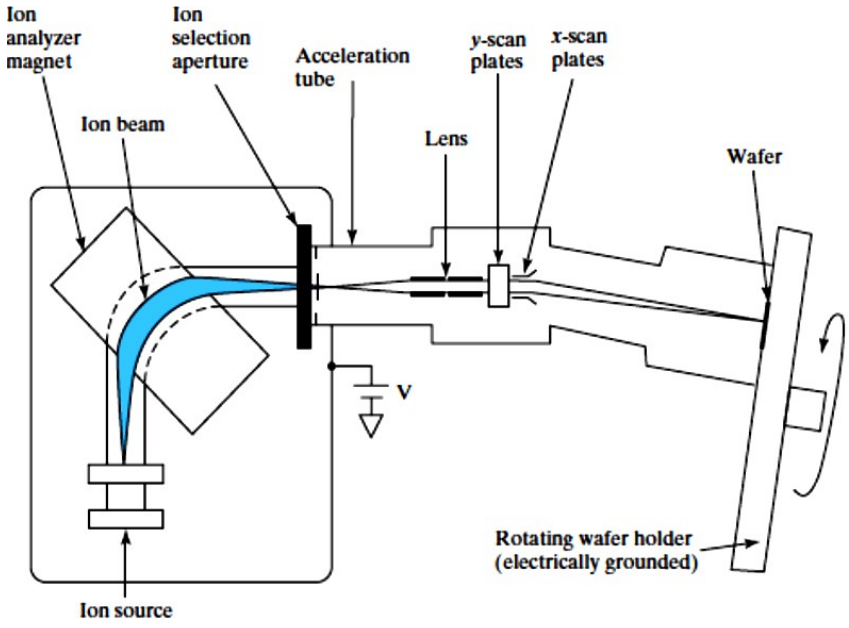

Fig. 7 gives the experimental setup of the ion-implantation technique.

Dopant diffusion during this anneal is significant due to implant-induced crystal defects. These pose limits on the depth resolution. Additionally, ion-implantation could not achieve abrupt buried layers, which is needed for modulation doping.

By using Ion implantation of elemental Boron into $BaSi_2$/Si (111) with dose amount $1.5x10^{12}$ cm^{-2}) were accomplished and then using RTA treatment (800ºC, 1min) were used for boron activation. After RTA treatment the hole concentration (p) 1.6×10^{18} cm^{-3}, resistivity 0.08 Ω-cm and mobility 65 cm^2/V.s were measured by Hall measurement [29] but, the hole concentration were could not enhanced beyond 1.6×10^{18} cm^{-3} and also could not achieve rectangular box-shaped form of the B depth profile in the $BaSi_2$, therefore we opted for MBE technique to grow the doped regions in the proposed *p-n* junction of $BaSi_2$ thin film solar cells.

1.3.2 IMPURITY DOPING BY USING MOLECULAR BEAM EPITAXY (MBE)

Molecular beam epitaxy (MBE) is a versatile epitaxy technique with the monolayer-scale control growth capabilities one typical RIBER MBE machine is shown in Fig. 8. With the advent of MBE a well-controlled abrupt doping profiles and alloy hetero-junctions/*p-n* junction offer many opportunities to implement device structures which have not been practical in the past. The development of Si based MBE technology is particularly important since there is already well developed Si based technology already existing in the industry and research laboratories. Instead of premixed source gases uniformly flowing through the chamber, individual atoms could be gases injected toward the substrate from separate Knudsen cell as molecular beams. In MBE, wide choice

of substrate temperature variation as well as Knudsen cell temperature optimization provision is available. The beam nature of MBE offers several advantages. First, it eliminates the possibility of thickness and composition non-uniformity. Secondly, it also minimizes any chemical reactions between the gas species before they impinge on the substrate surface due reasonable mean free path before reaching the substrate. Additionally, it reduces no-uniform distribution of atoms in the sample which is difficult in ion-implantation method. Finally, the refined crystalline structure of $BaSi_2$ could be achievable and possibly create less point defect along with amorphous regions. In MBE, excellent control of epilayer thickness and abruptness for hetero-structure growth is possible.

In MBE the main material sources are typically Knudsen effusion cells from which molecular beams are generated by thermal evaporation or sublimation process, as shown in Fig. 8. The solid or liquid elemental sources of materials are held in an inert crucible typically made of pyrolytic boron-nitride and heated by filaments or radiation. The vapor pressure of each species is controlled by setting the temperature of the effusion cell and is monitored with a beam-flux ion gauge that can be inserted to the nearest possible place of the substrate. The term "beam" means that evaporated atoms do not interact with each other or vacuum chamber gases until they reach the substrate film, due to the long mean free paths of the atoms and species that miss or desorb from the substrate are pumped away immediately.

Tantalum made shutters in front of each cell can be opened and closed to control the deposition of individual elements with monolayer accuracy in ultra-high-vacuum (UHV) environment. The pressure in MBE growth chamber could be maintained in the UHV level, typically ranging 10^{-11} to 10^{-8} torr, by a combination of different pumps, including ion pump, cryogenic pump, turbo molecular pump, and liquid-nitrogen-filled cryo shroud). During the MBE, the slow deposition rate ($\leq 1\mu$m/h) is excellently controlled, which allows the films to grow epitaxially. The UHV environment allows deposition with extremely low impurity concentrations and enables the use of *in-situ* surface analysis tools.

In the case of conventional silicon MBE, electron-beam evaporators (E-guns) are usually used for producing silicon beams, since the vapor pressure of silicon is extremely low, and conventional effusion cells cannot generate sufficient silicon vapor. It offers simple growth control due to the unity sticking coefficient of elemental silicon, and a wide temperature range for growth. However, E-guns have problems, such as poor growth rate control, electronic shut-down due to electrical discharge in e-beam source, and generation of surface defects due to charging of particles in the chamber. In the early work on gas source MBE, these problems were found to be easily eliminated by introducing gas sources instead of E-guns. Solid-source MBE work on *n*-type doping of silicon has focused on antimony because of the ease of source control [30-32]. Similar to arsenic, antimony suffers from severe surface segregation during growth at elevated temperatures. It was demonstrated that antimony surface segregation can be effectively suppressed and very abrupt transitions achieved in delta δ-doped layers by using low substrate temperatures and SPE. The similar trend was also achieved in Sb-doped $BaSi_2$ by using SPE technique in MBE. Although active concentrations higher than the equilibrium solid solubility can be achieved by this low

temperature process, deactivation during subsequent thermal treatment is likely. Arsenic and phosphorous, on the other hand, have high equilibrium vapor pressures at relatively low temperatures, in the 100 – 200 ºC range, making precise flux control difficult when they are used as dopant sources.

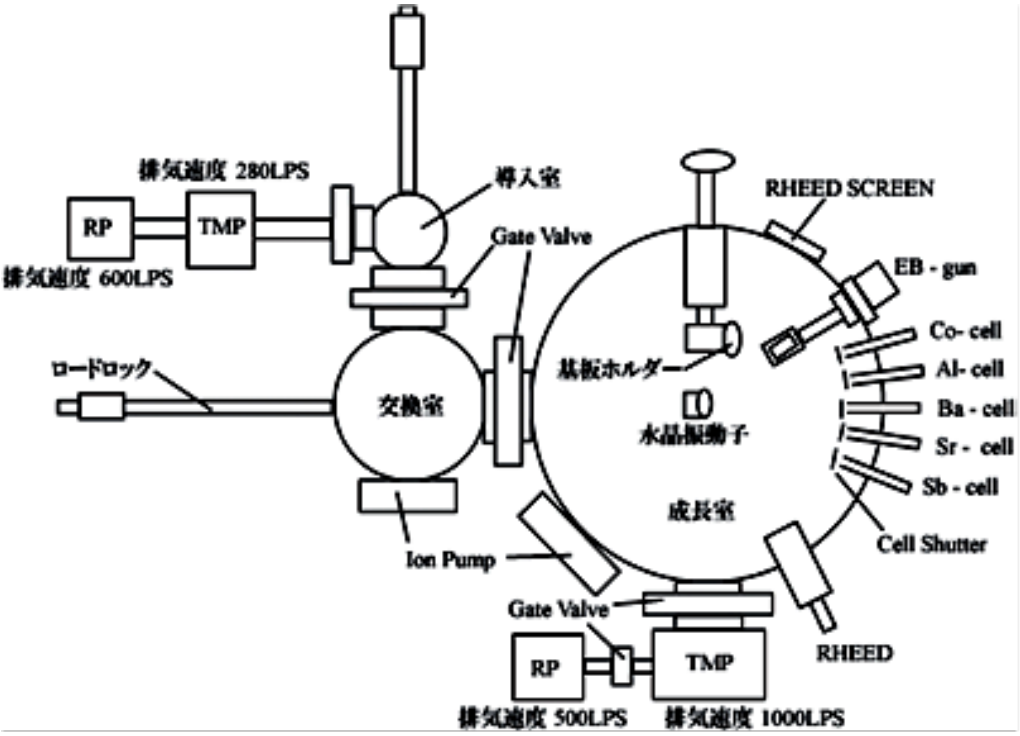

Fig. 8 gives the experimental setup of RIBER MBE machine.

Furthermore, arsenic vapor generated at such low temperatures is mainly composed of As_4, which has low sticking probability and tends to remain in the ambient for a prolonged time period and cause memory effects. Arsenic-delta-doping was demonstrated in (111) silicon epitaxy using a thermally evaporated As_4 source, and Pb was used as a surfactant [33]. However the background arsenic concentration was relatively high, estimated to be in the 10^{19} cm^{-3} ranges, because of the arsenic memory effect. Such a high doping level leads to significant conduction in the capping layer and complicates electrical evaluation of the δ-doped layer

As we know that MBE uses evaporation method in vacuum systems. In such system the molecular or atomic impingement rate is very important to be controlled. The impingement rate means that how many molecules or atoms impinge on a unit area of the substrate per unit time.
The impingement rate ϕ is a function of the molecular weight, temperature and pressure in the chamber and can be expressed as [6]:

$$\phi = 2.64 \times 10^{20} \left(\frac{P}{\sqrt{MT}} \right) \text{ molecules/cm}^2 - s \qquad (3)$$

In equation 3, P is the pressure in Pa, M is the molecular weight and T is the temperature in Kelvin.

Table I. Period systems of Elements

Dimitri Mendeleev (1869)

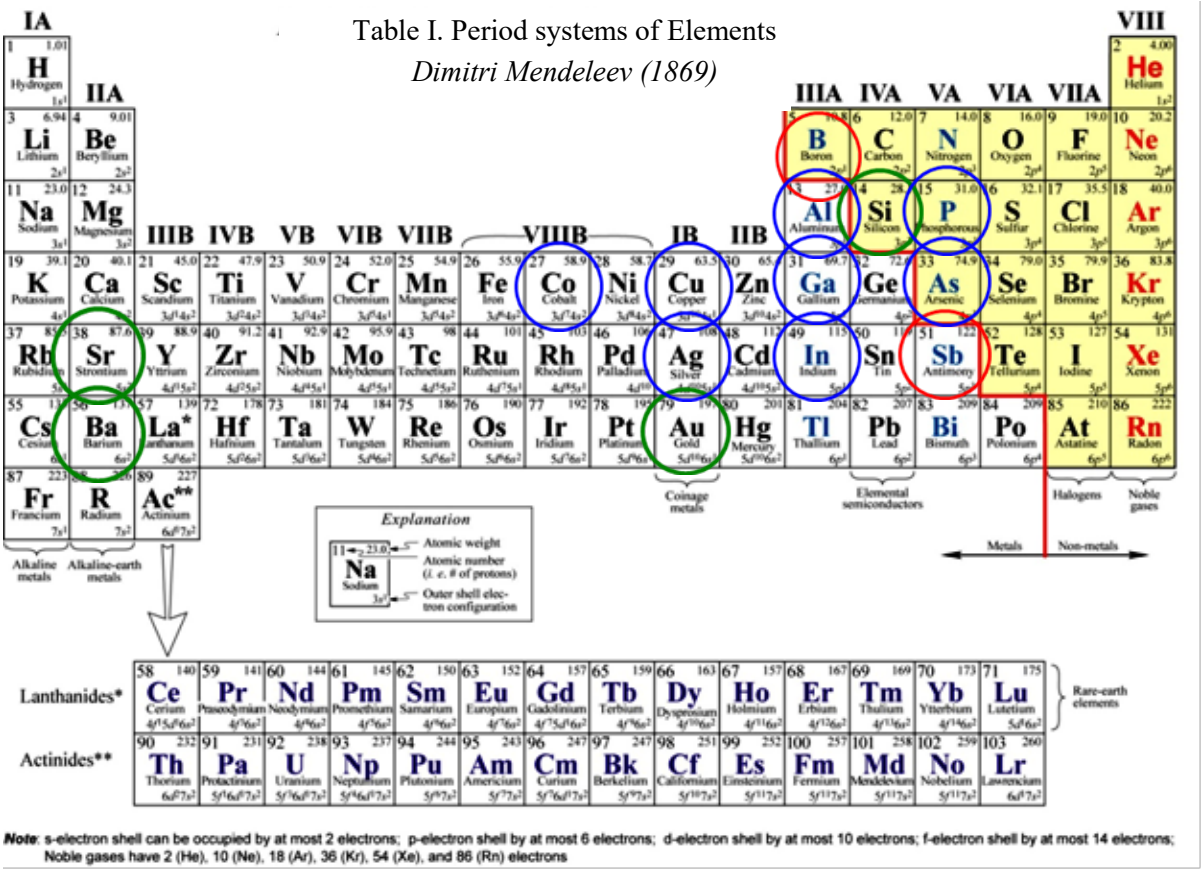

In this research, we choose group-III and -V elemental candidates from the periodic table of elements as listed in Table I, and aimed to form *n, n* $^{+}$*, p* and p^{+}-$BaSi_2$ by MBE growth for the formation of *p-n* junction thin film solar cells. There is no report on the conduction mechanism of impurity-doped $BaSi_2$ whether the temperature dependent resistivity gives us non-linear behavior or linear behavior in semiconducting $BaSi_2$. For the grain size and dopant precipitation study the best candidates among the potential dopant candidates will be chosen by using AFM and TEM investigation. Subsequently we will focus on the formation of good quality of *p-n* junction solar cells by using Sb-doped *n-* and n^{+}*-layer* as well as new dopant candidates-doped *p and* p^{+}*- layer,* respectively for novel next generation $BaSi_2$ thin film solar cells structure. In the next section the importance of doping and challenges to doping in $BaSi_2$ films.

1.3.3 IONIZATION ENERGY AND IMPORTANCE OF IMPURITY DOPING INTO $BaSi_2$

Many semiconductor technologies and devices rely on the ability to fabricate two different types of electrically conducting layers: *n*-type and *p*-type. An electrically active dopant atom provides a free carrier to the conduction or valence band by creating an energy level that is very close to one of the bands (shallow levels). In other words good quality *p-n* junction diodes could be formed by impurity doping, where the electric field around the *p-n* junction can separate the photo excited electron-hole pairs for photovoltaic power generation. An ideal dopant should therefore have a shallow donor/acceptor level and high solid solubility limit.

Ionization energy in Si can approximately be calculated by using Pseudo-hydrogen atomic

model for donors and acceptors levels in Si. The Pseudo-hydrogen atomic model has been shown in Fig. 9(a).

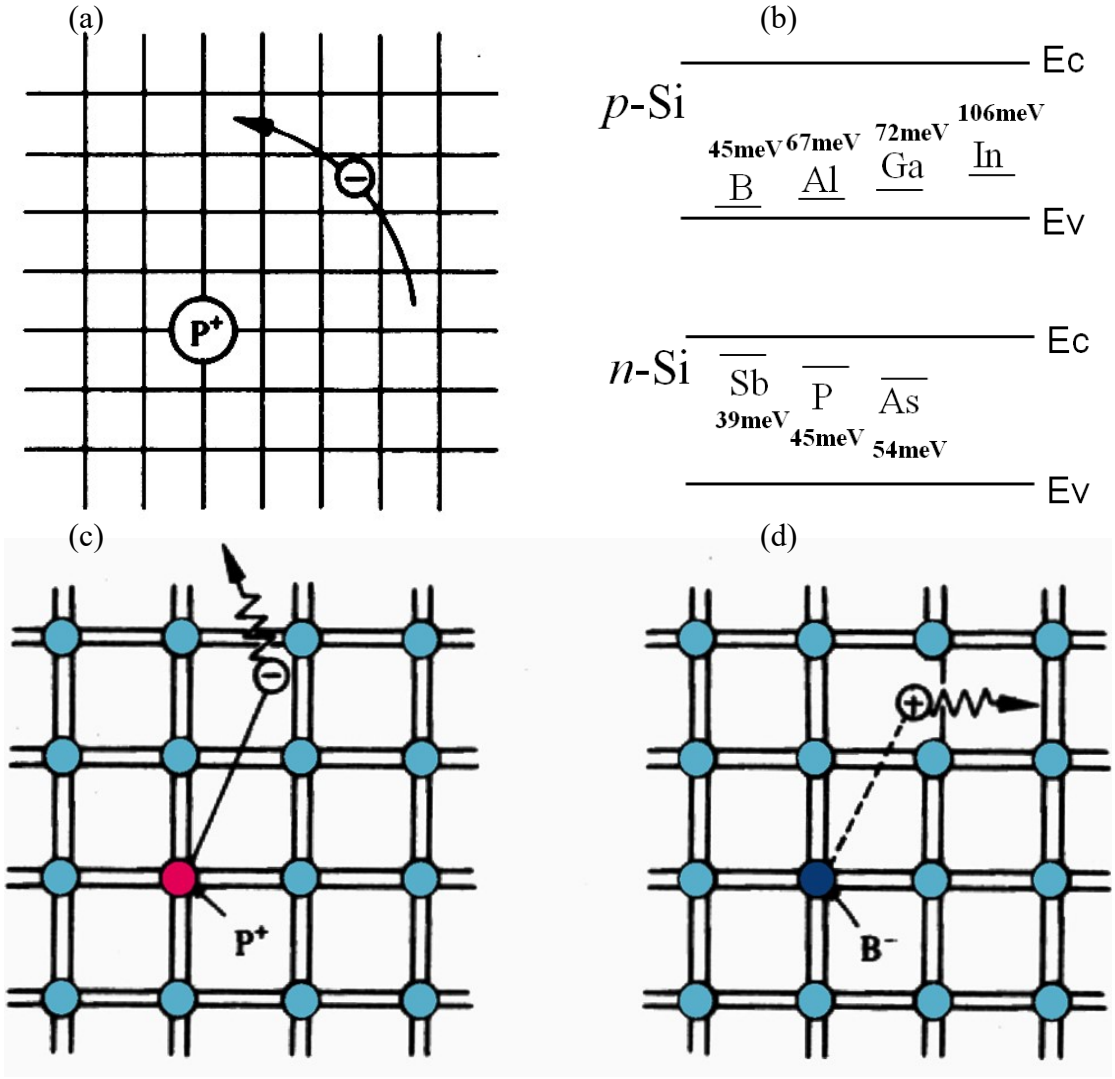

Fig. 9(a) gives hydrogen model of single P-atoms, (b) gives the ionization energy values of various dopants in silicon, (c) depicts the P-atoms in the host Si crystal as a dopant, and (d) depicts B-atoms in a Si crystal as dopant.

By using the data for P in this model of Eq. (4)

$$E_d = -\frac{m_n^* q^4}{2(4\pi K_s \varepsilon_0 \hbar)^2} = -13.6\ \text{eV}\ \frac{m_n^*}{m_0}\left(\frac{\varepsilon_0}{K_s \varepsilon_0}\right)^2 \approx -0.05\ \text{eV} \qquad (4)$$

In equation 4, K_s is the relative dielectric constant of Si ($K_{s,\,Si}$ = 11.8).

Figure 9(b) gives the lists of ionization energy values for various dopants candidates in silicon. Arsenic and phosphorous stand out as the best choices for *n*-type doping into Si based devices. For deep-submicrometer devices that require abrupt doping profiles, an additional requirement is a small diffusion rate of the dopant, which minimizes profile smearing during subsequent thermal processing steps. Compared to phosphorous, arsenic has a clear advantage of a much smaller diffusion coefficient. For the above reasons, arsenic has become the best choice for

heavy *n*-type doping of silicon. It is important to study and understand its incorporation and activation mechanism.

It is very challenging and crucial to incorporate the choice of dopant incorporation into $BaSi_2$ epitaxial film at the moment. The choice of available impurity incorporation is the most challenging job, even we have good freedom to vary the substrate temperature and optimize the Knudsen cell temperature during the MBE growth. The deep theoretical understanding of the $BaSi_2$ under the influence of different dopants atoms is inevitable. Energetic and the electronic structural consideration of the group 13 element like In and Ga -impurity doping to control the conductivity of $BaSi_2$ were discussed by Imai *et.al* [9]. The In-impurity type is inclined with the experimental result [9]. The Sb-doped $BaSi_2$ Knudsen cell temperature does not contribute magnificently to the variation of Sb-concentration in the $BaSi_2$ rather than the substrate temperature. It is very interesting finding that the Sb-atomic concentration is almost independent of the Knudsen cell temperature but strongly depends on the substrate temperature only, if we compare with the other available impurity candidates.

When In-dopant is used for *p*-type doping into $BaSi_2$, heavily doping levels and abrupt transitions were difficult to realize. The potential reason might be the high diffusion coefficient, interstitial incorporation, precipitation and surface segregation.

Solid-solubility limit mean that at a given temperature, there is an upper limit to the amount of an impurity-atoms, which can be absorbed by silicon or any other materials like $BaSi_2$. This quantity is called the solid-solubility limit for the impurity and is indicated by solid lines in the figure below for B, P, Sb, and As at normal diffusion temperature. Precipitation occurs if the concentration of one solid atom is above the solid solubility limit in the host solid materials, due to e.g., rapid quenching or ion implantation, and the temperature is high enough that diffusion can lead to segregation into precipitates. Other causes may be the high Knudsen cell temperature to provide more dense atomic fluxes during deposition. Especially in MBE some time low growth temperature can cause precipitation due to lower energy distribution for crystallization.

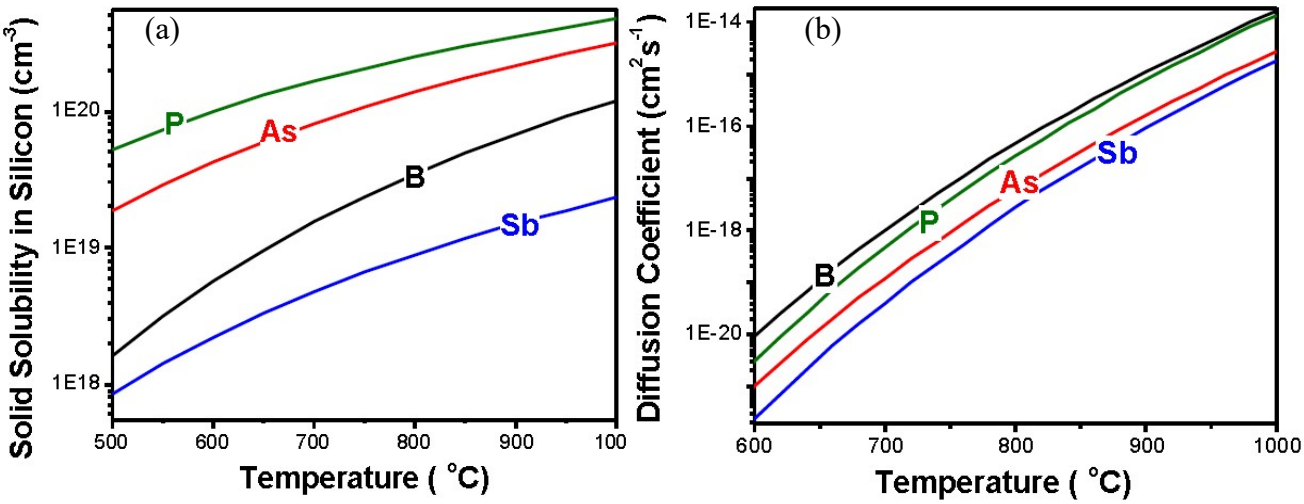

Fig. 10 (a) gives solid solubility limits of commonly used dopants in silicon and (b) gives intrinsic diffusion coefficients of commonly used dopants in silicon.

Solid solubility limit is indicated by solid lines in Fig. 10(a), for B, P, Sb, and As at normal diffusion temperature [34]. For example, the solid-solubility limit for boron is approximately 1×10^{20} cm^{-3} at 1000°C and 3.3×10^{20} cm^{-3} for phosphorus at the same temperature. Figure 10(b) compares the diffusion coefficients of boron, phosphorus, antimony, and arsenic. As compared to phosphorous, arsenic has a clear advantage of a much smaller diffusion coefficient [35]. For the above reasons, arsenic has become the best choice for heavy *n*-type doping of silicon. It is important to study and understand its incorporation and activation mechanisms in $BaSi_2$ too.

1.4 BASIC STRUCTURE OF SEMICONDUCTING BASED THIN-FILM SOLAR CELLS

The basic structure of $BaSi_2$ thin film solar cell structure can be divided into three major parts. First to develop good quality of Si(111) on transparent conducting oxide (TCO) and SiO_2. Secondly to grow good quality of n^+-$BaSi_2$ layer before the un-doped *n*-$BaSi_2$ by using Sb-doping into $BaSi_2$. Subsequently to grow a bit thicker epitaxially un-doped *n*-$BaSi_2$ layer before the growth of the top p^+-$BaSi_2$ layer for good ohimic contact as well as stronger electric field across the *p-n* junction to separate the electron-hole pair smoothly, which were generated in the un-doped $BaSi_2$ absorption layers by solar irradiation. Thirdly, to grow anti-reflecting (AR) coating on the top layer of the cell for light harvesting and subsequently grow surface electrodes for grid generation on AR surface.

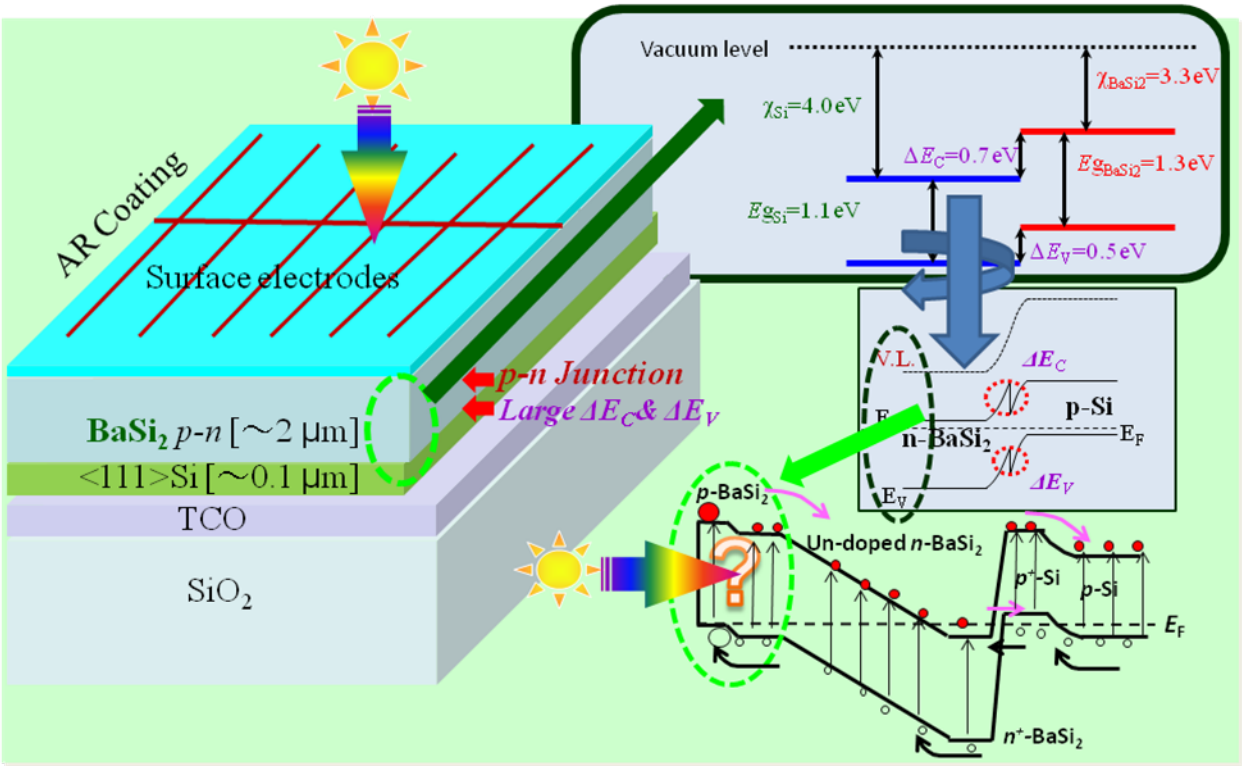

Fig. 11 shows the basic structure of $BaSi_2$ solar cell including *p-n* junction, energy band diagram and tunnel junction.

Now the most important part is the formation of *p-n* junction, where the electron affinity as well as band gap of Si is 4.0 eV, and 1.1 eV respectively whereas of $BaSi_2$ is 3.3 eV and 1.3 eV respectively, as shown in Fig. 11. One can easily see the band gap off-set at valance band as well as at conduction band of the order of 0.5 eV and 0.7 eV respectively [24]. This problem was solved and overcome by introducing tunnel junction (TJ) by heavy Sb-doping into n^+-$BaSi_2$ (n=10^{19} cm^{-3}) by using MBE growth [18,24], as shown in Fig. 12(b). The remaining problem is the formation of p^+-type $BaSi_2$ thin film layer on the un-doped n-$BaSi_2$ layer (n=5×10^{15} cm^{-3}, mobility=820 cm^2/V-s, shown in Fig. 12(a)), to complete the $BaSi_2$ *p-n* junction diode structure.

1.5 BACKGROUND OF THE RESEARCH

However, the number of experiments on impurity doping into $BaSi_2$ research has been quite limited so far. According to Imai and Watanabe, substitution of Si in the $BaSi_2$ lattice is more favorable than substitution of Ba from an energetic perspective, according to first-principle calculations [17].

The electron concentration of Sb-doped $n(n^+)$-$BaSi_2$ was controlled successfully in the range between 10^{16} and 10^{20} cm^{-3} at RT, as shown in Fig. 12(b) [18,20]. In case of Sb-doped $n(n^+)$-type $BaSi_2$, the electron concentration was excellently controlled in the range from 10^{16} and 10^{20} cm^{-3}. The problem of band offset at TJ has been solved to some extent. But the tunneling current mechanism is still not known and therefore the existence of negative differential resistance (NDR) across the TJ is necessary. The donor levels of Sb-doped $BaSi_2$ are still open research problem. Determination of conduction mechanism in Sb-doped $BaSi_2$ is really essential for the quantification of defects levels in the bad gap. The identification of solid solubility limit of Sb-doping into $BaSi_2$ is very important for controlling and efficient activation of the donor's atoms. Until now there is no report about the solid solubility limit in $BaSi_2$.

However, Ga-doped $BaSi_2$ displays *n*-type conductivity, in contrast to the theoretical prediction [18], as shown in Fig. 14(c). In case of Al-doped *p*-$BaSi_2$, we found diffusion problems in both the surface and *p*-$BaSi_2$/Si interface regions. The hole concentration was limited up to 10^{17} cm^{-3} in both In and Al-doped *p*-$BaSi_2$ respectively and it is therefore intensively realized to find another impurity atom which could be more favorable to form $p(p^+)$-type $BaSi_2$ with less diffusion tendency, good crystalline quality, having shallow energy levels and having large grain size for significant photo current flow across the *p-n* junction. In the next section the purpose of this research is given.

1.6 PURPOSE OF THIS RESEARCH

Electron concentration in Ga doped *n*-$BaSi_2$ was not controlled and it also behaves contrary to the theoretical conductivity, which is predicted by using DFT model.

In case of Sb-doped $n(n^+)$-type $BaSi_2$, the electron concentration was excellently controlled in the range from 10^{16} and 10^{20} cm^{-3}. The problem of band offset at tunnel junction has been solved to some extent. But the tunneling current mechanism is still not yet cleared. The donor levels of Sb-doped $BaSi_2$ need to be accomplished. Determination of conduction mechanism in Sb-doped is very important after the achievement of precipitated free Sb-doped $BaSi_2$.

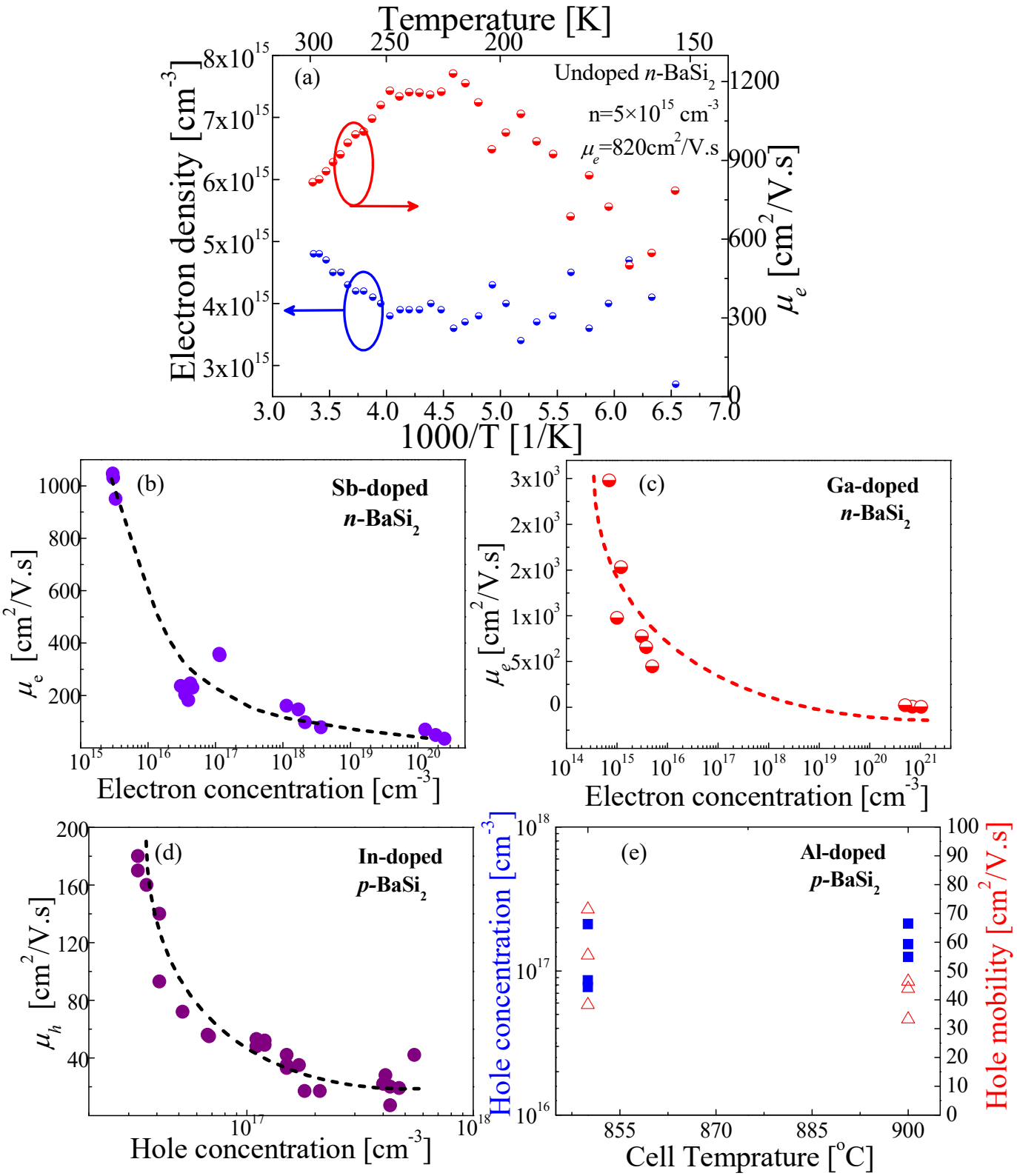

Fig. 12(a) mobility versus electron concentration relations for un-doped *n*-$BaSi_2$, [4] (b), (c) gives mobility versus electron concentration relations for Sb and Ga doped *n*-$BaSi_2$ films measured at RT [18,19] and (d), (e) gives mobility versus hole concentration relations for In and Al doped *p*-$BaSi_2$ films, measured at RT [18,20].

$BaSi_2$ is really essential for the quantification of defects levels in the bad gap. The solid solubility limit for Sb-doped is really important for the good quality of shallow donor level and to avoid localized precipitation of Sb-atoms in $BaSi_2$.

The hole concentration in In and Al-doped *p*-$BaSi_2$ were limited to $10^{17}cm^{-3}$ with some diffusion tendency toward the Si substrate as well as toward the un-doped $BaSi_2$ layer. But we need more hole concentration for shallow energy levels and low diffusion tendency for the formation of top *p*-layer of *p-n* junction structure.

Therefore, in this work, we chose Cu, Ag & B as a potential dopant candidate and aimed to form *p* & p^+-$BaSi_2$ thin film layers for different regions of *p-n* junction of efficient solar cells structure. Furthermore it was also aimed to investigate in detail about crystalline quality, surface morphology, micro-structure and electrical characterizations of doped $BaSi_2$ layers. The band gap and solubility limit of the impurity doped *p*-type layers are inevitable for the *p-n* junction and light absorption. Activation of the dopant atoms in the $BaSi_2$ is crucial problems and very little attention was paid in the past. In this dissertation Eg and solid solubility limit will also be attempted. We also consider the conduction mechanisms, NDR effect across the TJ & E_D of Sb-doped $BaSi_2$ for further improvement and band engineering of solar cell.

Therefore, in this research, we choose group-III and -V elemental candidates from the periodic table of elements as marked in Table I, and then choose the Knudsen cell temperature for each element based on the standard vapor pressure and temperature chart for elements. It was aimed to form *n, n* $^+$*, p* and p^+-layers of $BaSi_2$ solar cells parts by MBE growth to form good quality of *p-n* junction, TJ and ohmic contact. There is no report on the conduction mechanism of impurity-doped $BaSi_2$ whether the temperature dependent resistivity gives us non-linear behavior or linear behavior in semiconducting $BaSi_2$. For the grain size and dopant precipitation studies the best candidates among the potential dopant candidates will be chosen by using XRD, AFM and TEM investigation. Subsequently we will focus on the formation of good quality of *p-n* junction solar cell by using Sb-doped *n*- and n^+*-layer* as well as new dopant candidates-doped *p and* p^+*- layer,* respectively for novel next generation $BaSi_2$ thin film solar cell structure. In the next section, the importance of doping and challenges to doping mechanism in $BaSi_2$ films are discussed.

At last but not the least, we will focus on the fabrication and operation of $BaSi_2$ thin film solar cell operation based on the Sb-doped and optimized B-doping. The dark and light I-V characteristic will be considered at the end of this research for open circuit voltage and short circuit current density Jsc calculation.

1.7 ORGANIZATION OF THIS WORK

The main objective and aim of this dissertation is to report about the growth, crystalline quality and detailed study of electrical characterization of Ag, Cu, B-doped $BaSi_2$ thin films for different regions of $BaSi_2$ based Solar cells, including *p-n* junction, Tunnel junction and top p^+-layer for ohmic contacts. The focus is on enhancement of hole concentration and subsequently the activation energy levels (shallow levels) of the doped regions in thin film $BaSi_2$ solar cells. Microstructure

investigation of the impurity-doped regions is inevitable. In more simple words the remaining and challenging problems associated with the *p-n* junction regions of $BaSi_2$ thin film solar cells.

Chapter 2 presents results about the Au, Cu and Sb incorporation and surface segregation during the MBE growth into $BaSi_2$. Comprehensive studies were carried out to investigate, crystallinity, electrical characterization and SIMS measurement of the grown samples. New growth model is proposed for Ag and Cu-doped $BaSi_2$ to explain the most optimized impurity incorporation into $BaSi_2$ in accordance to the theoretical predictions for the solar cell application. Effects of Knudsen cell temperature variation of Ag and Cu sources on the electrical properties and subsequently the activation energy levels are also discussed. In the same chapter some remaining issue of Sb-doped *n*-layer of $BaSi_2$ were also addressed.

Chapter 3 presents results about the engineering of p^+-layer of $BaSi_2$ solar cells by using solid-source MBE of elemental Boron (B)-doped $BaSi_2$ and Si(111). It also examines electrical properties of these lightly doped and heavily doped $BaSi_2$ materials. This chapter also discusses about the growth, crystalline quality, and electrical characterization of B-doped $BaSi_2$ for the *p* and p^+-layers of thin film solar cells structure, detailed studies were attempted. The influence of both growth temperature variation as well as RTA treatment for boron activation, precipitation and B-solubility limit determination were discussed. At the end the most optimized growth condition and hole enhancement along with activation ratio will were discussed.

In Chapter 4, low temperature Hall measurement studies about the conduction mechanism and carrier transport mechanism in impurity doped-$BaSi_2$ were investigated. We choose very carefully the most suitable and optimized samples from each impurity doped $BaSi_2$ thin film based on the crystalline quality and electrical characterization at RT. It was not sure whether carrier transport mechanism in impurity doped $BaSi_2$ could be explained by Shklovskii-Efros (SE)-type and Mott-type variable range hopping (VRH) conduction mechanism or not. Therefore conduction mechanisms were studied in impurity doped $BaSi_2$ to quantify the existence of defects levels in the forbidden gap.

Chapter 5 discusses about the most important work of this dissertation. It gives nice flavor of B-doping optimization in $BaSi_2$ and formation of *p-n* junction for thin film solar cells. In more simplified words B could be a good dopant for different region of *p-n* junction of $BaSi_2$ solar cells. But we also need the band gap energy measurement of B-doped $BaSi_2$ for the formation of *p-n* junction and its most reliable acceptor energy level for thin film solar cells application having no precipitation. At the end of this chapter one fine *p-n* junction structure based on Sb-doped $BaSi_2$ and B-doped $BaSi_2$ under dark and light condition I-V characterization will be discussed along with efficiency measurement.

Finally, Chapter 6 summarizes contributions made in this dissertation and makes recommendations for future work.

CHAPTER 2: GROWTH AND CHARACTERIZATION OF SILVER (Ag), COPPOR (Cu)–DOPED AND SOME ISSUE OF ANTIMONY (Sb) DOPED *n*-$BaSi_2$

In this chapter, growth, crystalinity, atomic concentration and electrical characterization of Ag and Cu-doped $BaSi_2$ are discussed in detail. Special emphases were given to activation energy level, mobility as a function of Knudsen cell temperature and carrier concentration measurement. The core objective is to hunt suitable dopant candidates for the top *p*-layer as well as other regions of *p*-*n* junction. In the same chapter some unaddressed issues of Sb-doped *n*-layer of $BaSi_2$ are also tackled. In the next section, first Ag-doped $BaSi_2$ thin films is considered.

2.1 GROWTH AND HALL MEASURMENT OF Ag-DOPED $BaSi_2$ THIN FILMS

In the previous studies about In and Al doped *p*-type $BaSi_2$, where hole concentrations were limited up to $10^{17}cm^{-3}$ along with diffusion tendency and segregation problems [19,20]. The main objective of this research work is to grow, investigate and compare the electrical properties of Ag-doped $BaSi_2$ thin films with In, Al, and Sb-doped $BaSi_2$. Furthermore, to enhance hole concentration and control diffusion tendency in the $BaSi_2$ films, without compromising on good crystalline quality. In the next subsection experimental procedures are given in detail.

2.1.1 EXPERIMENTAL PROCEDURES

High-resistive (ρ=1000-5000 Ω-cm) *n*-type floating-zone (FZ)-Si(111) wafer substrates were cleaned by organic washing before RCA washing. During the organic washing, first the wafers were cleaned with a pure Acetone in the supersonic wave cleaner for 10 min and then cleaned in with methanol supersonic wave cleaner for 10 min. At the end the wafer were washed in pure water in supersonic wave cleaner for 10 min. During the RCA washing first the wafers were cleaned for 30 seconds in a H_2O:HF (50:1) bath at RT, and then 5 min in a H_2O:H_2O_2:HCl (4:1:1) bath maintained at 80°C, with 3 cycles of dump DI water rinse following each step. At the end the wafers were cleaned for 50 min in a H_2O:H_2O_2:NH_3 (4:1:1) bath maintained at 90°C, with 3 cycles of dump DI water rinse following each step. This cleaning procedure leaves a thin and volatile oxide protection layer on the surface. After wet cleaning, wafers are spun-dry and immediately loaded into MBE growth chamber. Immediately before the growth, the protective oxide is desorbed *in-situ* in the growth chamber at 850 °C to yield a clean, well-ordered (7 × 7) surface as observed by RHEED shown in Figure 13.

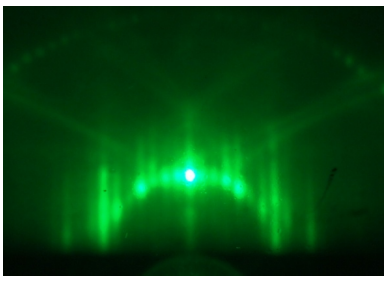

Fig. 13 a 7×7 RHEED pattern of Si substrate after thermal cleaning observed along <110> azimuth.

During growth, the substrate is heated radiatively and the temperature is monitored with a thermocouple located in the close proximity to the back side of the wafer. The thermocouple temperature reading is calibrated with a pyrometer, and verified. During the MBE growth first, reactive deposition epitaxy (RDE; Ba deposition on a hot Si substrate), of a 10-nm-thick $BaSi_2$ epitaxial film was carried out on Si(111) at 550 ˚C and then it was used as a template for $BaSi_2$ overlayers growth. During the MBE growth of Ag-doped $BaSi_2$ the Ba, Si, and, Ag (T_{Ag}= 600-900˚C) were co-evaporated on the $BaSi_2$ template at 600 ˚C after considering the standard range of vapour pressure and temperature chart for silver (Ag) element. The thickness of the grown layers including the template was 230–310 nm, which was thick enough for electrical measurements of impurity-doped $BaSi_2$ films. This is because most of the depletion region stretches toward the Si substrate at the $BaSi_2$/Si *p–n* junction due to a very small carrier concentration of approximately 10^{11} cm^{-3} of the Si substrates. The amount of Ag atoms doped in $BaSi_2$ was varied by changing the temperature of the Ag (T_{Ag}) sources. The ratio of the Ag to Ba vapor pressure (Ag/Ba ratio) was varied from approximately 10^{-5} to 1 by changing T_{Ag} from 600 to 900 °C.

The samples were investigated by RHEED, *θ-2θ* XRD, SIMS, AFM and Hall measurement (Van der Pauw method)[59]. In this dissertation the detailed discussion about the working principles of all these equipment and machines were skipped. The Au/Cr electrodes were evaporated in the high vacuum environment, provided by diffusion pump, which is supported by RT-pump. Magnetic field of 0.7 T, normal to sample surface was used for Hall measurement at RT and cryogenic condition (27-300K). In the next subsection experimental results will be discussed.

2.1.2 RESULTS AND DISCUSSION

2.1.2.1 *Crystallinity by RHEED, XRD and AFM*

Figures 14(a)-(c) show the RHEED patterns of the Ag-doped $BaSi_2$ along Si[11-2] and shows spotty or streaky pattern, which indicates that samples with *a*-axis oriented $BaSi_2$ were successfully grown. The RHEED patterns changed from ring to halo when T_{Ag} was further increased from 800 to 900 °C, shown in Fig. 14(d). These results indicate that Ag doping beyond 800 °C source temperature can deteriorated crystalline quality of the grown layers.

Figure 15(a) gives the basic structure of Ag-doped $BaSi_2$ thin film samples, which were grown at T_{Ag}=600-900°C. Fig. 15(b) shows *θ-2θ* XRD patterns of Ag-doped $BaSi_2$ films grown at T_{Ag}=600-900 °C. The diffraction peaks of (100)-oriented $BaSi_2$, such as (200), (400) and (600), are dominant in the *θ-2θ* XRD patterns, matching the epitaxial relationship between $BaSi_2$ and Si for the samples grown at T_{Ag}=600 and 800 °C. However, further increasing the Ag temperature resulted decrease in intensity of the (100)-oriented peaks, and several other diffraction peaks other than those of (100)-oriented $BaSi_2$ became pronounced.

Figures 16(a)-(b) show AFM images of the epilayer topography corresponding to the two samples grown at T_{Ag}=700 and 800 °C, with lower Ag concentration (T_{Ag}=700 °C) and higher Ag concentration (T_{Ag}=700 °C) respectively. While the surface remained flat in the former case, significant roughening is observed in the latter case, with a maximum roughness variation 1.8 nm from 3.3 nm to 5.1 nm.

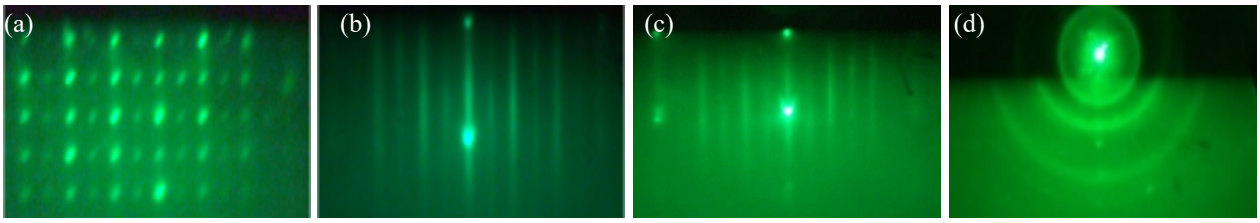

Fig. 14 RHEED pattern along Si[11-2] after MBE growth, for sample grown at T_{Ag}= (a) 600 ºC, (b) 700 ºC, (c) 800 ºC and (d) 900 ºC.

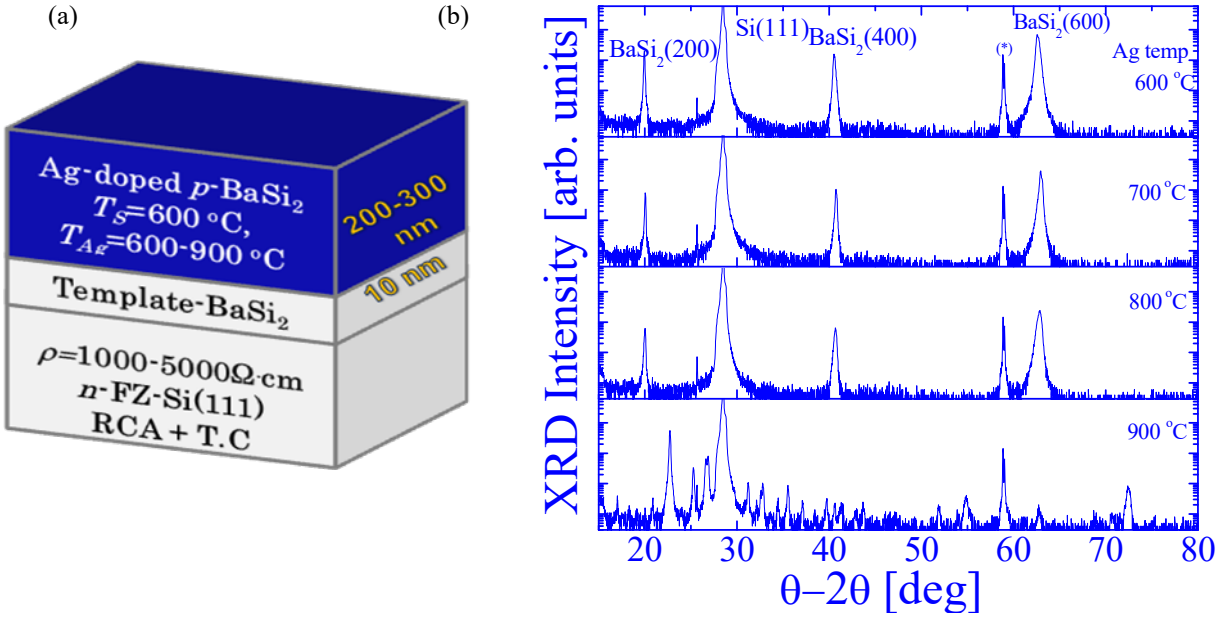

Fig. 15(a) basic structure of the Ag-doped $BaSi_2$ thin film samples grown at T_{Ag}=600-900 ºC and their corresponding (b) θ-2θ XRD patterns.

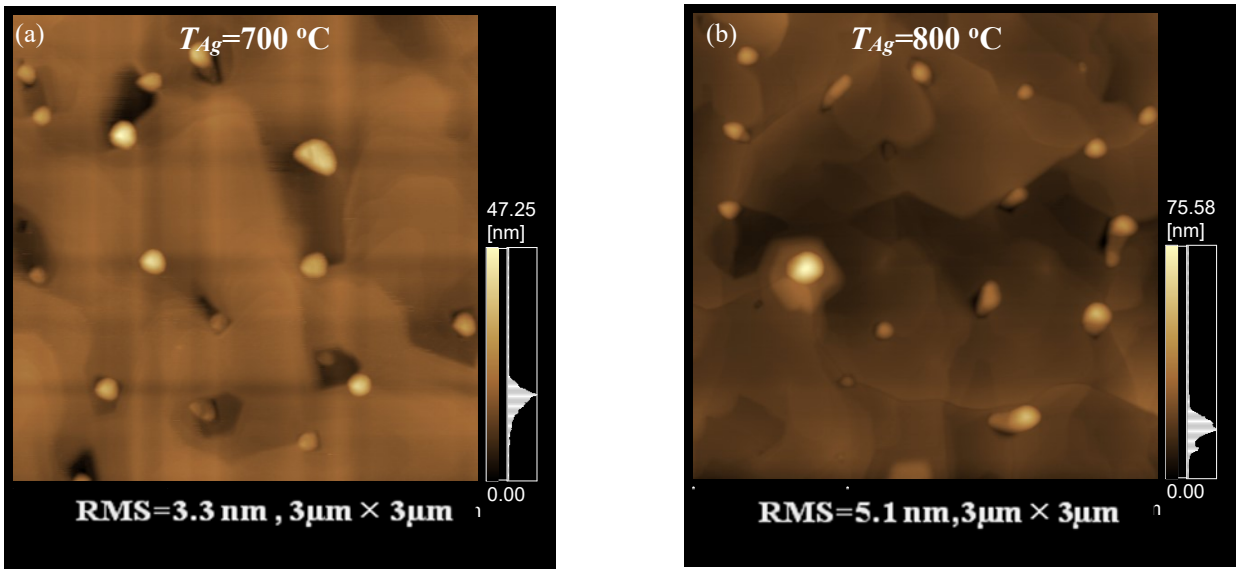

Fig. 16 surface morphology of Ag-doped $BaSi_2$: after MBE growth at, T_{Ag} = (a) 700ºC and (b) 800 ºC. Size of both AFM image are 3 μm × 3 μm.

2.1.2.2 Atomic concentration and Diffusion tendency by SIMS

Figure 17 (a) gives the SIMS profiles of Ag-doped $BaSi_2$ sample grown with T_{Ag}=600 °C. SIMS measurements revealed that the Ag-atoms are not uniformly distributed within the $BaSi_2$ layers and diffused or segregated toward the surface $BaSi_2$. The average Ag-atomic concentration, N_{Ag}, 10^{18} cm^{-3} was found in the same layer.

2.1.2.3 Electrical Characterization

Figure 17 (b) shows the mobility versus hole concentration relations for Ag-doped *p*-$BaSi_2$ films at RT, where hole density in increases gradually from 3×10^{15} to 3×10^{16} cm^{-3} with increasing Ag temperature, showing that the hole concentrations can be controlled as a function Knudsen cell temperature. However, the hole concentration is less than those in In and Al-doped $BaSi_2$ [18,20]. We speculate that this is attributed to a smaller ionization rate of Ag atoms in BaS_2 than In and Al atoms. In case of Ag-doped $BaSi_2$ films grown with 700 ºC, carrier density and mobility behavior are almost the same as those for Ga-doped $BaSi_2$ as shown in Fig. 12(c). The temperature dependent mobility behavior shows that the mobility contribution is not coming from the scattering of impurity atoms but comes from the Coulomb's lattice scattering mechanism, which is supported by low hole concentration in the grown sample.

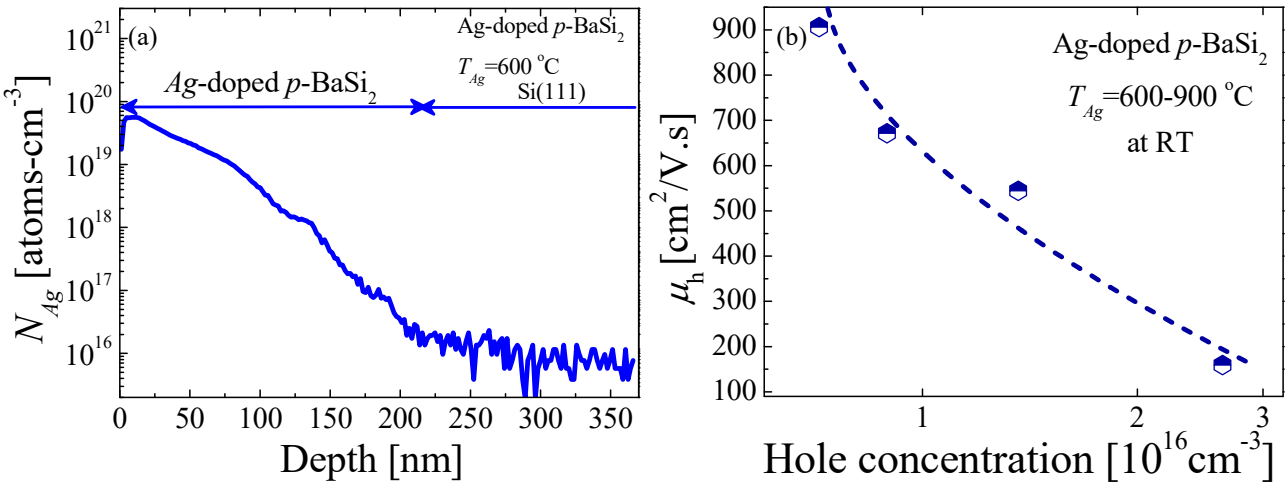

Fig. 17 (a), gives depth profiles of Ag-atoms in samples, grown at T_{Ag}= 600 °C and (b) gives the mobility versus hole concentration relations at RT for Ag-doped *p*-$BaSi_2$ grown at T_{Ag}= 600 °C.

Figure 18 (a) gives temperature dependence of hole mobility in Ag-doped $BaSi_2$. The mobility is higher when temperature is lower. The temperature dependent mobility behavior in Fig. 18(a) shows that the mobility contribution is not coming from the ionized impurity scattering of atoms but comes from the lattice scattering mechanism, which is supported by low hole concentration in the grown sample as explain by Matthiessen's rule :

$$\frac{1}{\mu}=\frac{1}{\mu_s}+\frac{1}{\mu_i}=\frac{q}{m^*}\left(1/\left[AT^{3/2}+BN_iT^{-3/2}\right)\right) \quad (5)$$

Figure 18 (b) gives temperature dependence of hole concentration in Ag-doped $BaSi_2$. The mobility is higher when temperature is lower Therefore, we can approximate that the hole density

behave, like, $p \propto \exp(-\frac{E_A}{2k_B T})$ and therefore the accepter energy level, E_A=0.12 eV for Ag-doped *p*-BaS_2 were measured.

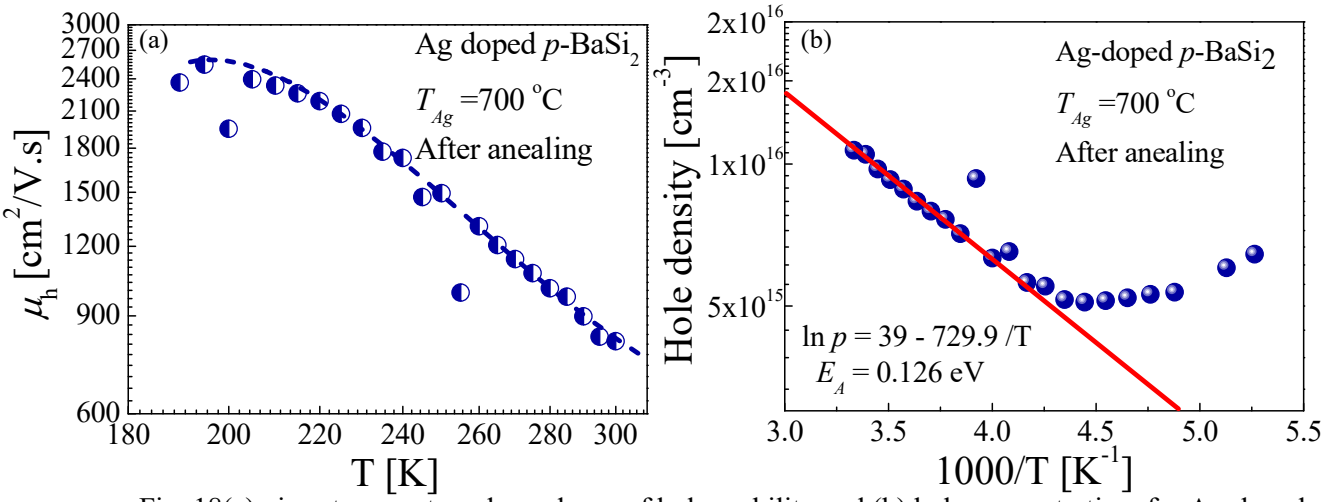

Fig. 18(a) gives temperature dependence of hole mobility and (b) hole concentration, for Ag-doped *p*- $BaSi_2$ grown at T_{Ag}=700 °C.

2.2 GROWTH, CRYSTALLINITY, AND ELECTRICAL CHARACTERIZATION OF Cu-DOPED $BaSi_2$

In case of Ag-doped *p*-$BaSi_2$, the hole concentrations were found to be limited upto 10^{16} cm^{-3} and we could not successfully grow the heavily doped $BaSi_2$ *p*-layer for the top part of solar cells structure. The basic structure of $BaSi_2$ solar cell is shown in Fig. 11,which demands strongly to get heavily doped p^+-layer for the top-layer of the cell. In this persuasion, we continue the effort to use an alternate dopant candidate from the group-IB like Cu to achieve the desired target. In this part of research it was aimed to grow lightly doped *p*(*n*)-type and heavy doped $p^+(n^+)$-layers by MBE technique for the *p*-*n* junction regions of thin film solar cells by using Cu as a potential candidates and then to investigate the crystallinty and electrical characterization at room as well as at cryogenic conditions. Recently Imai and Watanabe theoretically predicted that Cu behaves as an *n*-type dopant in $BaSi_2$ [9]. In the last experiment of Cu-doped $BaSi_2$, where (100)-oriented $BaSi_2$ was not satisfied completely [21]. After this result we realized that the Cu Knudsen cell temperatures can be reduced and Cu-doped $BaSi_2$ can be developed to overcome these two issues of minor diffusion tendency as well as crystalline quality and aimed to investigate and control the electrical properties of Cu-doped $BaSi_2$ films for *p*-*n* junction. In the next subsection we briefly discussed about experiment.

2.2.1 EXPERIMENTAL PROCEDURES

High-resistive *n*-type floating-zone (FZ)-Si(111) substrates were cleaned by RCA washing, by using the same procedure as discussed for Ag-doped $BaSi_2$ growth. Reactive deposition epitaxy (RDE; Ba deposition on a hot Si substrate), of a 10-nm-thick $BaSi_2$ epitaxial film was carried out on Si(111) at 550 ˚C and then it was used as a template for $BaSi_2$ overlayers. First, Ba, Si, and Cu (T_{Cu}= 800-1200˚C), were co-evaporated on the $BaSi_2$ template at 600 ˚C to form Cu doped *n*-$BaSi_2$ film

by MBE. The amount of Cu atoms doped in $BaSi_2$ was varied by changing the temperature of the Cu (T_{Cu}) source. The ratio of the Cu to Ba vapor pressure (Cu/Ba ratio) was varied from approximately 10^{-4} to 1 by changing T_{Cu} from 800 to 1200 °C. In order to investigate the diffusion tendency and atomic concentration of Cu atoms in $BaSi_2$ completely, one additional sample of Cu-doped $BaSi_2$ structure (undoped $BaSi_2$ (100nm)/Cu-doped $BaSi_2$ (50nm)/Si(111)) at 600 ºC was prepared. The RHEED, *θ-2θ* XRD, SIMS, AFM and Hall measurements were used to characterize the crystalline quality, atomic concentration and electrical properties of the grown layers. The hall measurements were conducted at RT as well as at cryogenic conditions (27-300 K). Magnetic field of 0.7 T, normal to sample surface was used for Hall measurement. In the next subsection experimental results were discussed.

2.2.2 RESULTS AND DISCUSSION

2.2.2.1 *Crystallinity by RHEED, XRD and AFM*

Figures 19(a)-(d) shows the RHEED patterns after MBE growth of the Cu-doped $BaSi_2$ along Si[11-2] and shows spotty or streaky patteren, which indicates that samples with *a*-axis oriented $BaSi_2$ were successfully grown. The RHEED patterns changed from ring to halo when T_{Cu} was further increased from 1000 to 1200 °C. These results show that Cu doping beyond 1000 °C deteriorate the crystalline quality of the grown thin film.

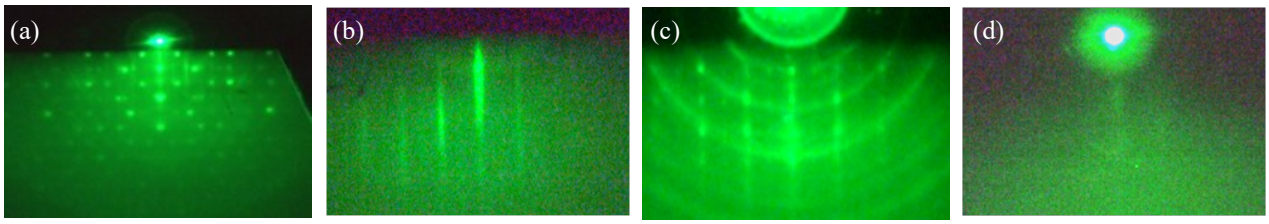

Fig. 19 displays RHEED pattern along Si[11-2] after MBE growth, for sample grown at, T_{Cu} (a) =800, (b) = 975, (c) =1000 and (d) =1200 ºC.

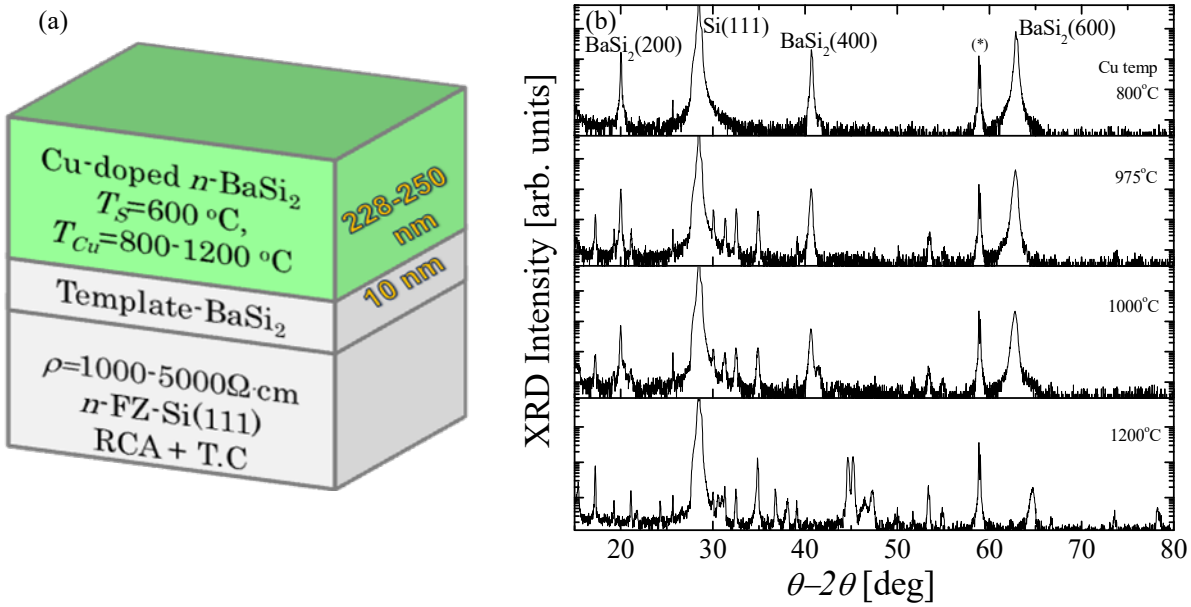

Fig. 20 (a) gives structure of the Cu-doped $BaSi_2$ grown thin film samples, grown at T_{Cu}=800-1200 ºC and (b) shows *θ-2θ* XRD patterns of Cu-doped *n*-$BaSi_2$.

Figure 20(a) gives the basic structure of the grown layers based on the growth condition, T_s=600°C and T_{Cu}=800-1200 °C. Figure 20(b) shows θ-2θ XRD patterns of Cu-doped $BaSi_2$ films grown at T_{Cu}=800-1200 °C. The diffraction peaks of (100)-oriented $BaSi_2$, such as (200), (400) and (600), are dominant in the θ-2θ XRD patterns, matching the epitaxial relationship between $BaSi_2$ and Si for the samples grown at T_{Cu}=800 and 1000 °C. In these samples some small number of extra peaks near to Si(111) and $BaSi_2$(400) were also observed. However, increasing the Cu temperature beyond 1000°C resulted in a decrease of intensity for (100)-oriented peaks, and several other diffraction peaks other than those of (100)-oriented $BaSi_2$ became pronounced.

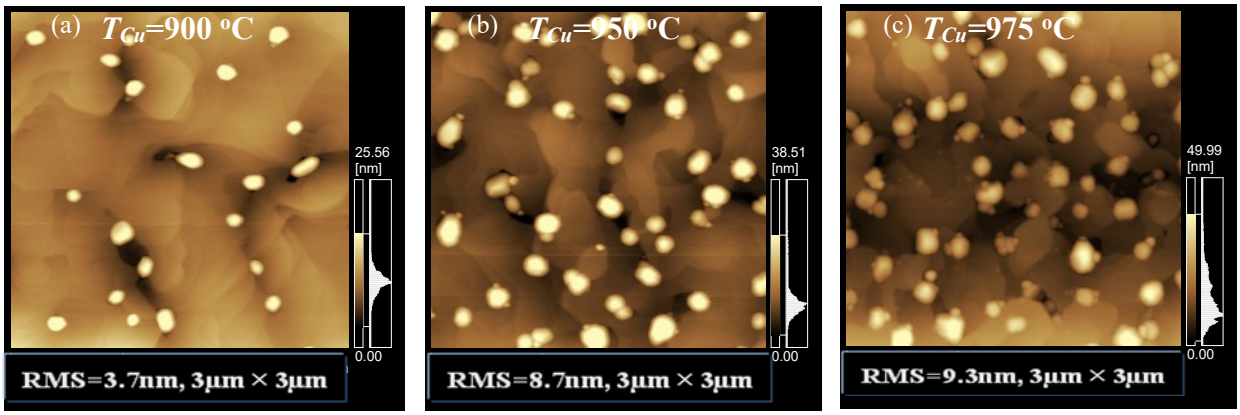

Fig. 21(a) gives the Cu-doped $BaSi_2$ surface morphology: after MBE growth, at T_{Cu}=(a) 900 °C,(b) 950 °C and (c) 975 °C. All AFM images are 3 μm × 3 μm in size.

Figures 21(a)-(c) show AFM images of the epilayer topography corresponding to the samples grown at T_{Cu}=900 to 975 °C, with lower Cu concentration (T_{Cu}=900 °C) and higher Cu concentration (T_{Cu}=975 °C). While the surface remained flat in the former case, significant roughening is observed in the latter case, with a maximum roughness variation of the order of 5.6 nm, while changing Knudsen-cell temperature from 900 °C to 975 °C with corresponding roughness change from 3.7 nm to 9.3 nm. We speculate that the white spot could be arises due to Cu-atomic precipitation or surface segregation.

2.2.2.2 Atomic concentration and Diffusion tendency by SIMS

Figure 22(a) shows the SIMS profiles of Cu-doped $BaSi_2$ film grown at T_{Cu}=900 °C.

SIMS measurements revealed that the doped Cu atoms are almost uniformly distributed within the $BaSi_2$ layers and some could be segregated toward the surface $BaSi_2$. The average Cu atomic concentration, N_{Cu}, was found to be approximately 10^{20} cm^{-3}. The relationship between Cu atoms could be confirmed from the Hall measurement data. Figure 22(b) shows the SIMS profile of the undoped $BaSi_2$ (100nm)/Cu-doped $BaSi_2$ (50nm)/Si(111) structure, where the Cu atoms do not show any segregation tendency even when the Cu-doped $BaSi_2$ layers were embedded in the $BaSi_2$ over layers.

2.2.2.3 Electrical Characterization

Figure 23(a) gives mobility versus electron concentration relations for Cu-doped *n*-$BaSi_2$ films at RT, where mobility decreases with increasing electron concentrations. This trend is usually

predicted by ionized impurity scattering in conventional semiconductors.

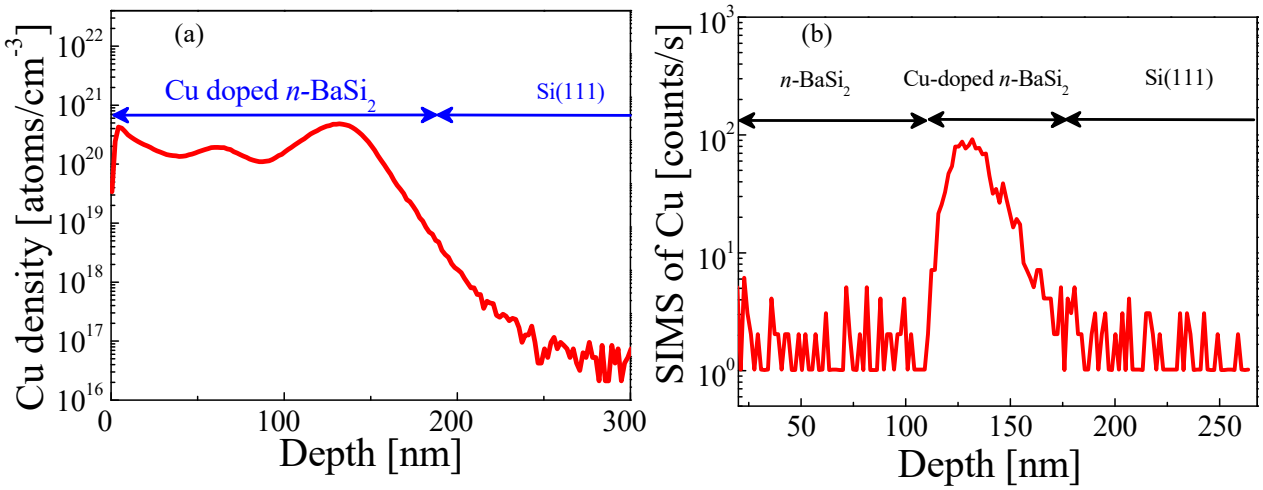

Fig. 22(a) SIMS depth profiles of Cu atoms in samples, grown at T_{Cu}= 900 °C and (b) SIMS depth profiles of Cu atoms in un-doped $BaSi_2$ (100nm)/Cu-doped $BaSi_2$ (50nm)/Si(111).

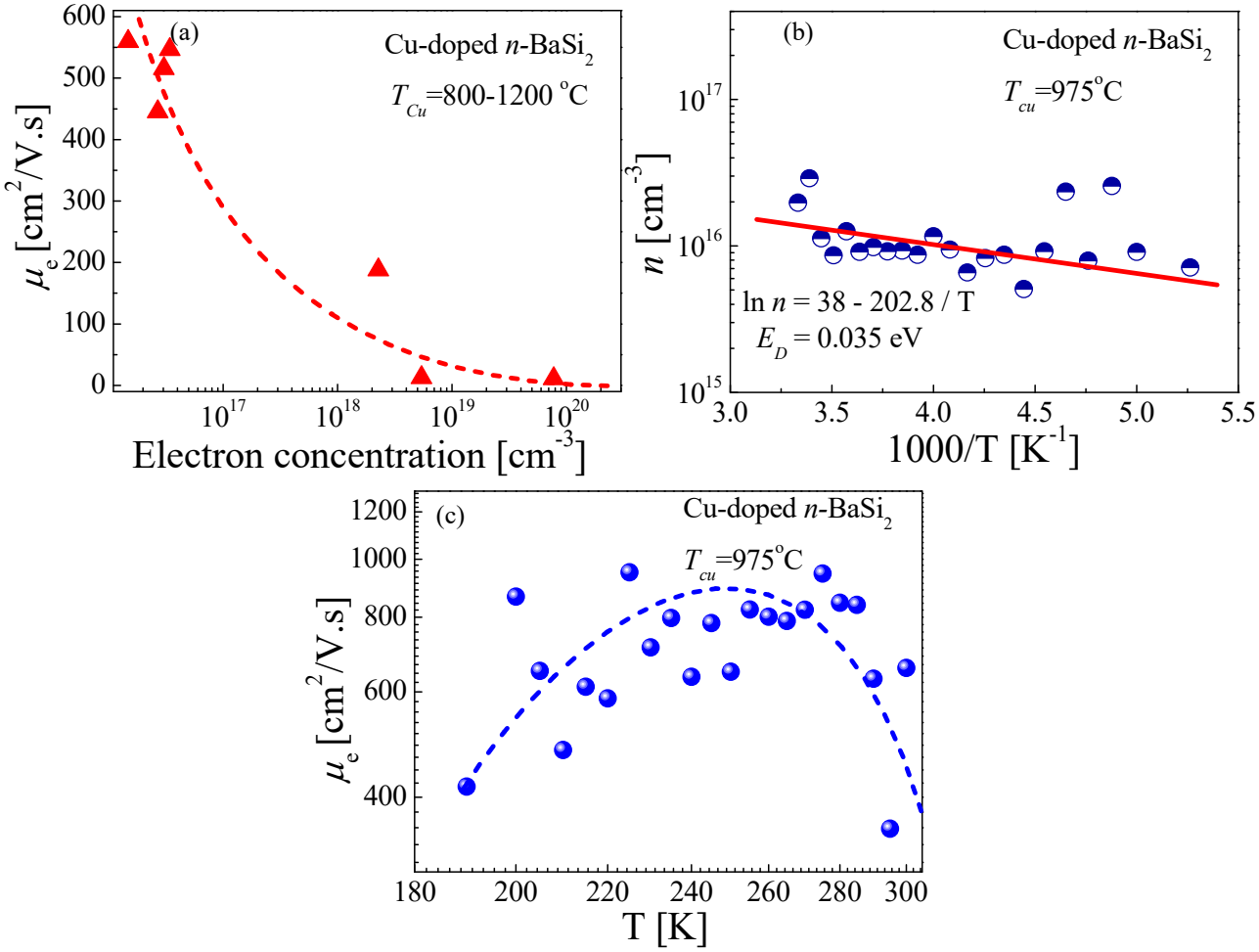

Fig. 23(a) relationship of measured mobility and electron concentrations for Cu-doped *n*-$BaSi_2$, grown at T_{Cu}=800-1200 °C, (b) Temperature dependence of electron concentration for Cu-doped *n*-$BaSi_2$ grown at T_{Cu}=975 °C, and (c) mobility for Cu-doped *n*- $BaSi_2$ grown at T_{Cu}=975 °C.

The electron concentration in Cu-doped $BaSi_2$ remained unchanged, even when the Cu temperature was increased to 950 °C, but increased sharply up to more than 10^{20} cm^{-3} around 1000 °C. These

results suggest that control of electron concentrations in Cu-doped $BaSi_2$ is little difficult. This is probably due to the fact that the insertion site of Cu atoms in $BaSi_2$ is interstitial site [23].
Our claim based on the experimental results that the doping of Cu into $BaSi_2$ is giving rise to *n*-type semiconductor, is consistent with the theoretical prediction by Imai and Watanabe [23]. Temperature dependence of electron concentrations for Cu-doped *n*-BaS_2 is given in Fig. 23(b) and the accepter energy level, E_D=0.035 eV were calculated

Figure 23(c) gives the temperature dependence of electron mobility in Cu-doped $BaSi_2$ and probably it follows Matthiessen's rule, where the mobility trend shows both ionized impurity scattering mechanism as well as lattice scattering mechanism in the grown sample. Cu dopant was found not suitable for $BaSi_2$ because of controllability problem of carriers as a function of Knudsen cell temperature and more detailed reason is still unknown.

After the unsuccessful results of Cu-doping into $BaSi_2$ it became more challenging scientific problem for us to develop *p*-layer of $BaSi_2$ thin film but science need perseverance and strong motivation. Therefore an effort was made to hunt more suitable dopant candidates from periodic table to make p^+-layer of $BaSi_2$ solar cell. But before starting another hunt, it was seriously realized to solve some important problems associated with already successful achievement of Sb-doped $BaSi_2$ $n(n^+)$-layer of $BaSi_2$. In case of Sb-doped $BaSi_2$, we were not sure about the ohmic contact, donor energy level as well as negative differential resistance across TJ of Sb-doped *n*-$BaSi_2$ as a function of temperature [18]. Therefore it was decided to see the ohmic behavior for relatively low doping level of Sb-doped *n*-$BaSi_2$ on Si(111) 3°-off angle at low temperature and E_D measurement. The NDR effect across the TJ was also attempted. In the next section these three important issues associated with Sb-doped $n(n^+)$-$BaSi_2$ will be attempted.

2.3 Sb-DOPED $BaSi_2$ GROWTH, HALL MEASUREMENT AND NDR EFFECT AT TJ

Kobayashi *et al.,* established that the Sb-doping is suitable for n (n^+)-layer of $BaSi_2$, and the highest number of electrons concentration over 10^{20} cm^{-3} were achieved. Suemasu *et al.,* [38] successfully produced heavily Sb-doped n^+-$BaSi_2$ ($n>10^{19}cm^{-3}$)/p^+-Si hetero-structure, which behaves as a tunnel junction, and could be used to overcome the large band offsets at $BaSi_2$/Si, *p-n* junction. Du *et al.,* [16] found that Sb-atoms do not show any segregation tendency even when the Sb-doped $BaSi_2$ layers were embedded in the $BaSi_2$ overlayers. But we have no detail information about the activation energy level of Sb-doped $BaSi_2$, NDR effect across the TJ and the ohmic behavior as a function of temperature.

The issue of NDR was further investigated to see the tunneling current flow mechanism across the TJ. In the next subsections, the experimental procedures and measurements are presented.

2.3.1 TEMPRATURE DEPENDENCE OF OHMIC I-V AND E_D OF Sb-DOPED $BaSi_2$

It was uncertain, whether heavily Sb-doping beyond 10^{19} cm^{-3} is necessary to form ohmic contacts on *p*-Si(111) 3°-off angle substrate or not. It is therefore aimed to grow relatively low Sb-doped $BaSi_2$ on *p*-Si(111) 3°-off angle substrate, and then measure the temperature dependent Hall effect as well as I-V characteristics to confirm the ohmic behavior on the surface-surface electrodes. It was also realized to measure the activation energy level for Sb-doped $BaSi_2$. In this persuasion, let

us move to the next subsection for experiment.

2.3.1.1 EXPERIMENTAL PROCEDURES

An ion-pumped MBE system equipped with standard Knudsen cells (K-cells) for Ba and Sb (T_{Sb} =250°C), and an electron-beam evaporation source for Si was used. For electrical measurements, low-resistive *p*-Si(111), 3º-off angle substrate (>1 Ω· cm) substrates were washed through the same procedure as mentioned in section 2.1 and then used for epitaxial growth. During MBE growth, firstly, a 10-nm-thick $BaSi_2$ epitaxial film was grown on *p*-Si(111) at 555 °C by RDE and this was used as a template for the $BaSi_2$ overlayers. Next, Ba, Si, and Sb were co-evaporated at 500 °C onto the $BaSi_2$ template to form impurity-doped $BaSi_2$. The thickness of the grown layers including the template was approximately 140 nm. The Au/Cr electrodes were fabricated in the Vacuum evaporation machine. Magnetic field of 0.7 T was applied normal to sample surface during the Hall measurement at RT as well as at cryogenic condition (27-300K).

2.3.1.2 RESULTS AND DISCUSSION

Figure 24(a) shows the RHEED patterns after MBE growth of the Sb-doped $BaSi_2$ along Si[11-2] and shows spotty pattern, which indicates that samples with *a*-axis oriented $BaSi_2$ were successfully grown. Figure 24(b) shows the dominant diffraction peaks of *a*-axis oriented-Si $BaSi_2$ (200), (400), and (600) on Si in the grown samples.

To secure the ohmic contacts on the surface at lower temperatures, first the temperature dependence of current-voltage (*I-V*) characteristics were measured as shown in Fig. 25(a). Ohmic behavior was confirmed over the wide temperature range between 30 and 300 K. Resistance increases with decreasing temperature, which is typical in semiconductors materials.

Figure 25(b) shows the temperature dependence of electron concentration and resistivity in the Sb-doped *n*-$BaSi_2$. The electron concentration is about 3.3×10^{18} cm^{-3} at 300K, and decreases gradually with decreasing temperature and goes down to 2.8×10^{17} cm^{-3} at 27 K.

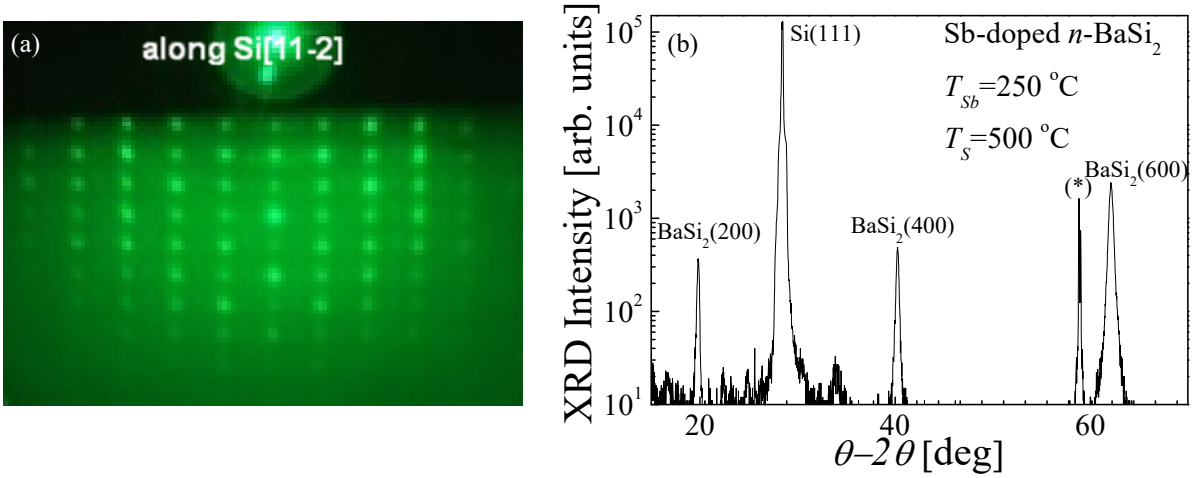

Fig. 24 (a) RHEED pattern along Si[11-2] azimuth after MBE growth and (b) XRD intensity for sample grown at T_{Sb}= 250 ºC, and T_S= 500 ºC.

As shown in Fig. 25(a), the resistance between the two electrodes, which consists of contact at the $BaSi_2$/AuCr and $BaSi_2$ bulk resistance, decreases by a factor of 3 when the temperature decreases

from 300 K to 27 K during *I-V* measurement. This change can be well explained by the change in resistivity as shown in Fig. 25(b). This means that the contact resistance is smaller than the bulk

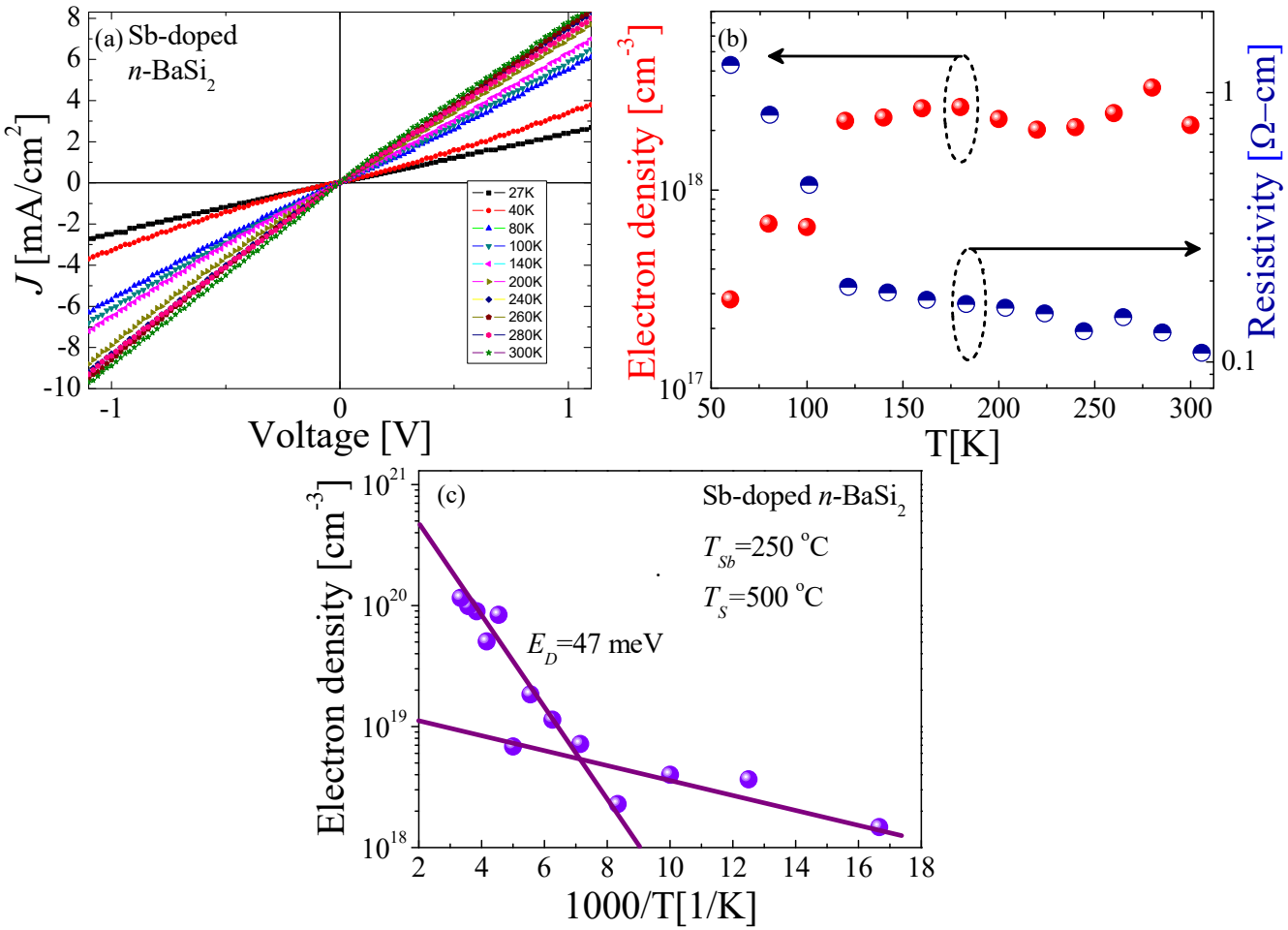

Fig. 25(a) temperature dependence of *I-V* characteristics in Sb-doped *n*-$BaSi_2$/*p*-Si, (b) temperature dependence of resistivity and electron concentration and (c) Temperature dependence of electron concentration in Sb-doped *n*-$BaSi_2$ only.

resistance in this temperature range, there by showing that good electrical ohmic contacts are formed.

Furthermore the resistivity is decreasing with increasing temperature as shown in Fig. 25(b). This is because the Fermi level might be in the band gap and the supplies of free carrier density are varying with varying temperature [6]. This temperature dependence is typical in semiconductors materials. This behavior confirm that the Sb doped $BaSi_2$ is non-degenerated semiconductor material as shown in Fig. 26. If the impurity concentration increases, the distance between impurity atoms decreases and a point will be reached when donors electrons, will began to interact with each other. When this happens, the single discrete donors energy will split into a band of energies. As the donor concentration further increases, the band of donors states becomes more widens and may overlap with the bottom of the conduction band. This overlap may happen when the donor's concentration becomes comparable with the effective density of states (host atoms). When the concentration of the electrons in the conduction band exceeds the effective density of states, N_c, the Fermi energy lies within the conduction band. At this level the resistivity will not

change with the variation of temperature. Figure 25(c) shows that the electron concentration is about 3.3×10^{18} cm^{-3} at 300K, and then decreases gradually with decreasing temperature and goes down to 2.8×10^{17} cm^{-3} at 27 K. The resistivity increases gradually accordingly. The donor level of Sb-doped $BaSi_2$ was calculated approximately to be 47 meV. This level shows that the donor level is shallow in the Sb-doped $BaSi_2$. The solid solubility limit and precipitation of Sb atoms in $BaSi_2$ materials are stil open research problems.

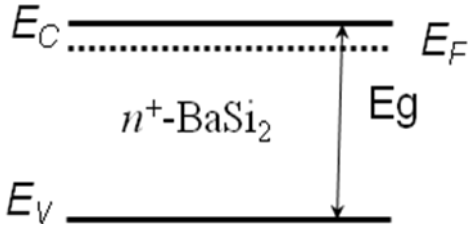

Fig. 26 gives depiction of non-degenerate levels in band gap of n^+-$BaSi_2$.

The $BaSi_2$ solar cell structure is shown in Fig. 11, which need good quality of TJ at the hetro-junction to overcome the band off-set discontinuity. Suemasu *et al.,* [38], and Kobayashi *et al.,* [18] successfully achieved heavy doped n^+-$BaSi_2$ layer on the p^+-Si (111) but the detailed tunneling mechanism across the TJ is still unknown, as shown in Fig. 31. In the next section NDR effect will be discussed in the context of tunneling phenomenon across the TJ.

2.3.2 GROWTH OF Sb-DOPED $BaSi_2/p^+$-Si(111)(TJ) TO MEASURE NDR EFFECT

NDR effect in the J–V characteristics in the forward bias is often observed, like in heavily doped n^+/p^+ Esaki, diodes, but in some cases not [36]. The potential reasons might be the existence of defect levels at the n^+-$BaSi_2/p^+$-Si hetero interface because of the difference in both crystal structure and lattice constants. Therefore, it can be speculated that the tunneling currents can flow via localized states in the forbidden gap, rather than by a band-to-band direct transition [24]. In this part of the dissertation NDR effect was further investigated. In the next subsection the experimental procedure are given.

2.3.2.1 EXPERIMENTAL PROCEDURES

An ion-pumped MBE system equipped with standard Knudsen cells (K-cells) for Ba and Sb (T_{Sb} =250°C), and an electron-beam evaporation source for Si was used. For electrical measurements, low-resistive p^+-Si(111), substrate (>0.1 Ω-cm) substrates were washed through the same procedure as mentioned in section 2.1 and then used for epitaxial growth. During MBE growth, firstly, a 10-nm-thick $BaSi_2$ epitaxial film was grown on p^+-Si(111) at 550 °C by RDE and this was used as a template for the $BaSi_2$ overlayers. Next, Ba, Si, and Sb were co-evaporated at 560-600 °C onto the $BaSi_2$ template to form two samples of impurity-doped $BaSi_2$ tunnel structure. RHEED, XRD and low temperature I-V characterizations were used to investigate the grown samples. The thickness of the grown layers including the template was approximately 78 nm.

The Al contact were formed on the back side of the TJ structure by using sputtering machine and Au/Cr electrodes were evaporated on the front surface of the samples as shown in Figure 27. Temperature dependent I-V characterizations were measured in a cryogenic environment

(27-300K).

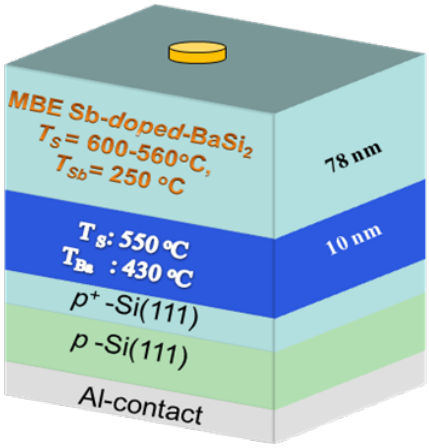

Fig. 27 gives tunnel junction (TJ) structure for $BaSi_2$ *p-n* junction.

2.3.2.2 RESULTS AND DISCUSSION

Figure 28(a), shows the RHEED patterns after MBE growth of the Sb-doped $BaSi_2$ grown at T_S=560 °C along Si[11-2] azimuth and shows streak and ring pattern, which indicates that samples with *a*-axis oriented $BaSi_2$ were successfully grown but the crystalline quality need to be improved. Figure 28(b) shows the RHEED patterns after MBE growth of the Sb-doped $BaSi_2$ grown at T_S=600 °C along Si[11-2] azimuth and shows very clear spotty pattern, which indicates that samples with *a*-axis oriented $BaSi_2$ were successfully grown and having good crystalline quality.

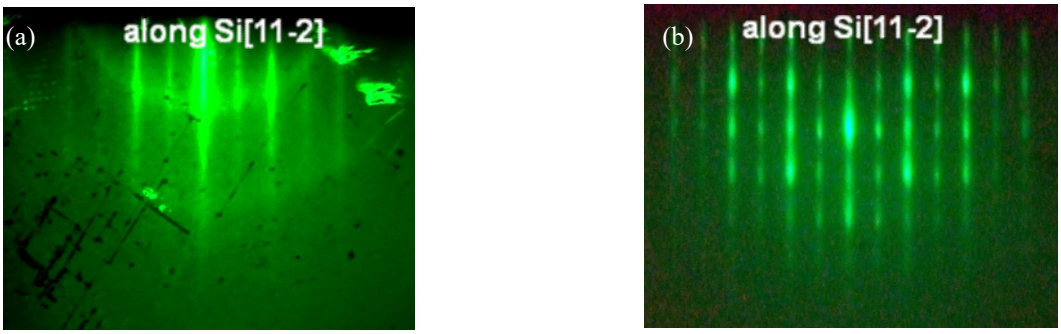

Fig. 28 RHEED pattern along Si[11-2] azimuth, for the samples grown at (a) T_S= 560 °C, and (b), T_S= 600 °C.

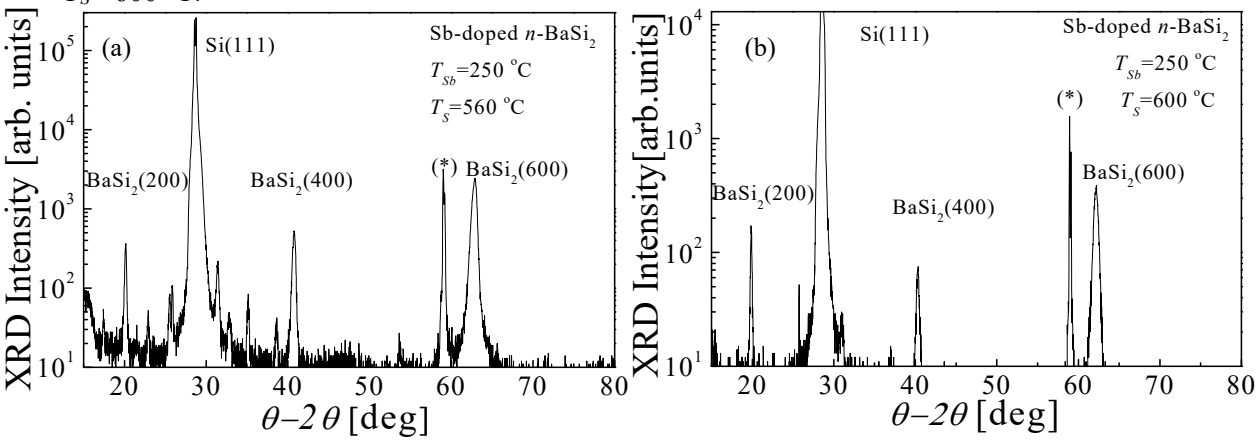

Fig. 29 XRD pattern after MBE growth of Sb-doped $BaSi_2$ for samples grown at (a) T_S= 560 °C, and (b), T_S= 600 °C.

Figure 29(a) and (b) show the dominant diffraction peaks of a-axis oriented-Si $BaSi_2$ (200),

(400), and (600) on Si in the grown samples.

Figure 30(a) gives the temperature dependent I-V characteristics of samples A and B, where the resistance between the two electrodes, which consists of contact at the $BaSi_2$/AuCr and $BaSi_2$ bulk resistance, increases when the temperature decreases from 300 K to 27 K during *I-V* measurement. It shows that the series resistance tends to be large at the low temperature

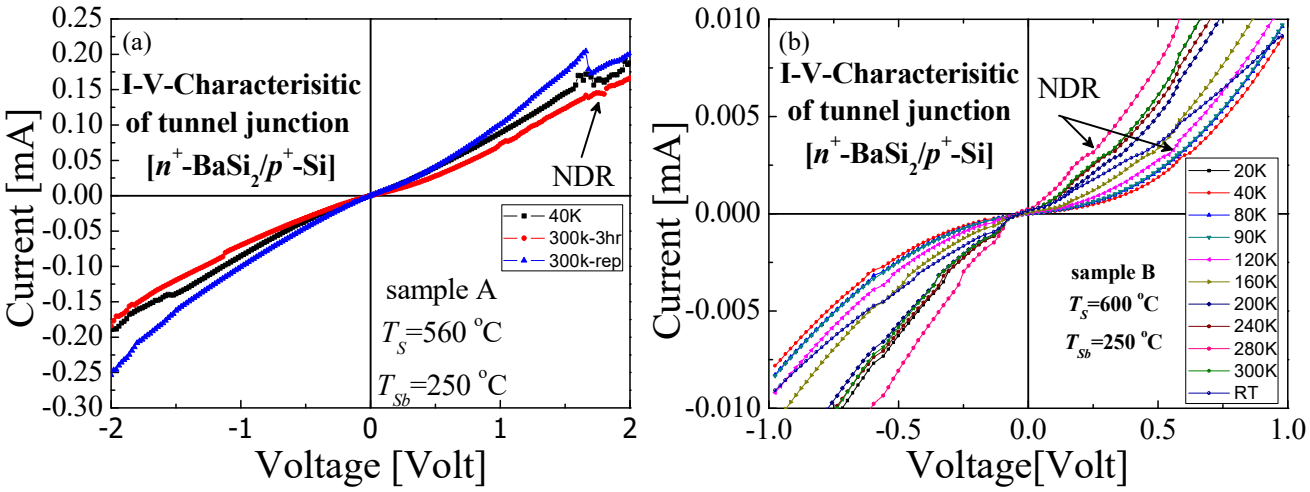

Fig. 30 I-V characterization of the sample grown at (a) T_S= 550 ºC, and (b), T_S= 600 ºC.

The resistivity of electrode, *p*-Si substrate, and n^+-$BaSi_2$ films decreases at the low temperature. There may be some defects level across the TJ and the tunneling process through these defect levels may happen.

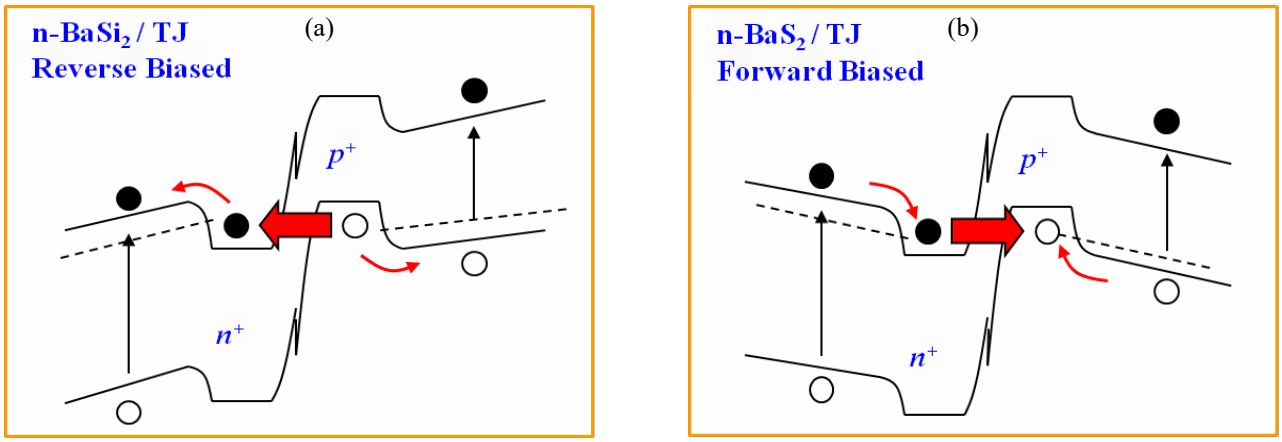

Fig. 31 gives depiction of tunneling current flow through *TJ* structure, (a) in a reverse biased mode, and (b) in a forward biased mode.

The tunneling process may happen on relatively low temperature due to the un-activation of the defects levels. It shows that small amount of tunneling current happened across the TJ at 0.8 V and 0.4 V respectively in Fig. 30(a) and 30(b) respectively.

The energy band diagram of the TJ in $BaSi_2$ in forward as well as in reverse biased shows current tunneling phenomena are given in Fig. 31(a) and 31(b) respectively. In the next chapter the most challenging issue of the B-precipitation free p^+-layer of B-doped $BaSi_2$ thin films is presented in detail.

CHAPTER 3: MBE GROWTH AND CHARACTERIZATION OF B–DOPED $BaSi_2$

In this chapter the epitaxial growth, crystalline quality, microstructure and electrical characterization of B-doped $BaSi_2$ for the *p* and p^+-layers of thin film solar cell structures are explained in detail. The influence of both growth temperature variation and RTA treatment for boron activation, precipitation and B-solubility limit determination are discussed. Optimized growth conditions and hole enhancement along with activation ratio are discussed at the end.

3.1 BACKGROUND

In chapter 2 it was established that Cu and Ag are not suitable dopant candidates for the formation of *n*-layers and *p*-layers of *p-n* junctions including tunnel junction (TJ) structure. The electron concentration of Sb-doped $BaSi_2$ was well controlled in the range between 10^{17} and 10^{20} cm^{-3} at RT by changing the temperature of the Sb-Knudsen cell crucible [18]. In contrast, the hole concentration was limited up to $3\text{-}4\times10^{17}$ cm^{-3} at RT for In, Al, and Ag-doped $BaSi_2$ layers [18,19, 20,39]. Electron concentrations could not be controlled in Cu-doped $BaSi_2$ as a function of Knudsen cell temperature [40]. It is therefore necessary to use impurity atoms, with heavily p^+-type doping in $BaSi_2$. In this research, we will attempt to achieve the desired level of hole concentrations in $BaSi_2$, by incorporating B-atoms into $BaSi_2$.

3.2 DETAILED ANALYSIS OF B-INCORPORATION IN $BaSi_2$ THIN FILMS

In this research, boron (B) was chosen as an alternative impurity candidate from Group-III-A with the aim to achieve $p(p^+)$-type doping ranging 10^{16} -10^{20} cm^{-3} in $BaSi_2$ for the engineering of smart *p-n* junction. Special emphasis was given to the formation of p^+-layer for the top part of solar cell structure.

It is also important to grow high quality crystals having no precipitation of B-clusters and large grain size. Diffusion as well as segregation phenomena are also important points of investigation for studying impurity-doped $BaSi_2$. As was previously established, $BaSi_2$ thin films can be grown epitaxially on a Si(111) substrate with the orientation alignment of $BaSi_2$ (100)//Si(111), and small lattice mismatch of 1.0% for $BaSi_2$ [010]//Si[11-2] and 0.1% for $BaSi_2$ [001] // Si[-110] [10]. The smallest grain size of $BaSi_2$ is approximately 0.1 μm [41], due to three epitaxial variants rotating around each other by 120° with respect to the surface normal [13,42]. Many grain boundaries (GBs) and other defects in a film typically deteriorate the optical and electrical properties of the film. As was previously mentioned, the poly crystalline Si, GBs enhance carrier recombination due to their high defect densities and gettering impurities [15]. At the same time, it is thought that recombination of carriers is suppressed by the local built-in potential at the GBs as reported in $Cu(InGa)Se_2$ [43]. The grain size in the un-doped *n*-$BaSi_2$ films was found to be approximately 0.1–0.3 μm [44]. Detailed investigation of bright-field (BF) and dark-field (DF) TEM images and selected-area electron diffraction (SAED) patterns showed that the GBs in the $BaSi_2$ epitaxial layers consist mostly of $BaSi_2$ {011} planes [43,44]. However, there have been no reports available about GBs in impurity-doped *p*(*n*)-$BaSi_2$ epitaxial films. Therefore, this

investigation aims to study the plane view BF TEM image and SAED pattern of some potential samples by using TEM, to find the diameter, size and density of B-atoms in the precipitated B cluster structure of *p*-$BaSi_2$ regions. Furthermore, it aims to stud the B- activation efficiency in the grown samples. Experimental arrangements are given in the next subsection.

3.2.1 EXPERIMENTAL PROCEDURES

Details of the growth procedure for impurity-doped $BaSi_2$ films were previously described for In, Sb, Al, Cu and Ag-doped $BaSi_2$ [4,18,20,39,40]. For electrical measurements, high-resistivity FZ-*n*-Si(111) (ρ> 1000 Ω· cm) substrates were used. Substrates prior to each experiment were washed by the same standard procedure as presented in Sec.2.1 for Ag-doped $BaSi_2$. The method carried out for MBE growth of B-doped $p(p^+)$-$BaSi_2$ films are briefly described as follows. First, a 10-nm-thick $BaSi_2$ epitaxial film was grown on Si(111) at 510 °C by RDE. This was used as a template for the $BaSi_2$ overlayers. Next, Ba, Si, and B were co-evaporated at 600 °C onto the $BaSi_2$ template to form impurity-doped $BaSi_2$. The temperature of B, T_B, was varied from 1250 to 1575 °C in samples A-G. The thicknesses of the grown layers including the template were approximately 250 nm. Ohmic contacts with Au/Cr on as-grown samples of B-doped $BaSi_2$ films grown at $T_B \leq 1500$°C could not be performed. Thus rapid thermal annealing (RTA) was performed at 800 °C for 0.5 min, 1 min and 2 min in an Ar atmosphere (samples C-G). Crystalline structure details as well as atomic concentration of B-doped $BaSi_2$ were examined using, RHEED, XRD, AFM, SIMS, and TEM. Depth profiles of B-doped $BaSi_2$ films were characterized by secondary ion mass spectroscopy (SIMS) using O_2 ions.

To observe the grain size of B-doped *p*-$BaSi_2$ and GBs, plan-view TEM samples prepared by mechanical polishing. Ion milling was observed by using TOPCONEM-002B operated at 120 kV. Hole concentration and mobility in lightly and heavily doped B-doped $BaSi_2$ epilayers were obtained from conductivity and Hall measurements using the van der Pauw configuration. Hall measurements were performed under a magnetic field of 0.7 T, normal to the sample surface.

3.2.2 RESULTS AND DISCUSSION

3.2.2.1 *Crystallinity by RHEED, XRD, AFM and TEM*

Figures 32(a)-(h), show streaky RHEED patterns of B-doped as-grown $BaSi_2$ films prepared with T_B=1250-1575 °C and T_S=600 °C as observed along the Si[11-2] azimuthal axis, which indicates that the $BaSi_2$ films were successfully grown. The RHEED patterns changed from streak to spot patterns for the sample grown with, T_B =1300 °C. Figure 33(a) shows the θ-2θ XRD patterns of B-doped as-grown $BaSi_2$ films with T_B=1250-1575 °C. The diffraction peaks of (100)-oriented $BaSi_2$, such as (200), (400) and (600), are dominant, for the samples grown with T_B=1250-1450 °C which confirms the epitaxial relationships between $BaSi_2$ and Si, without extra peaks from B-nano □lusters. However, further increasing T_B beyond 1450°C resulted in two new diffraction peaks of rhombohedral B(110) around 2θ=36° and B(220) at 2θ=77°. This indicates that the crystalline quality begins to deteriorate with increasing B-atomic concentrations in the $BaSi_2$ films.

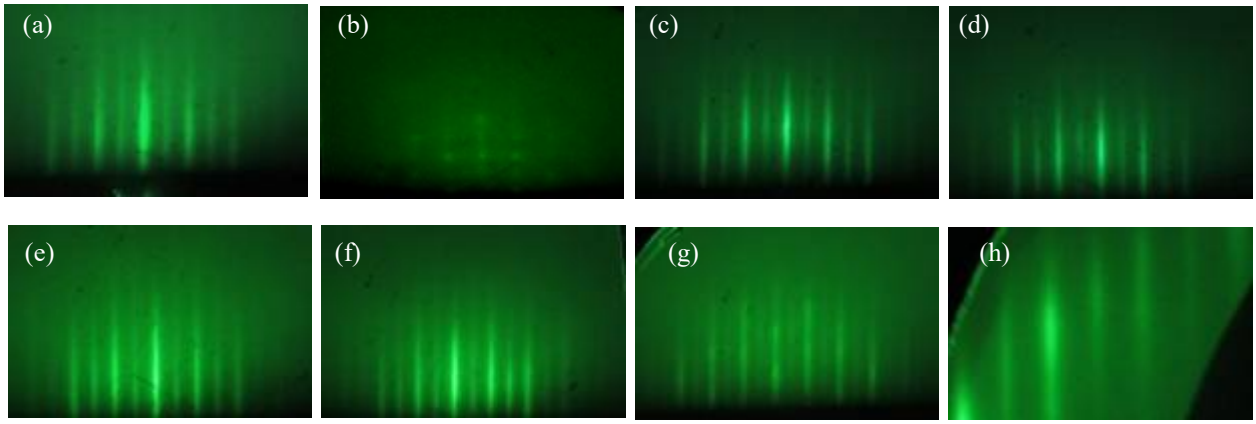

Fig. 32 RHEED patterns of B-doped $BaSi_2$ samples when T_B is (a) 1250, (b) 1300, (c) 1350,(d) 1400,(e) 1450,(f) 1500, (g) 1550 and (h) 1575 °C, observed along the Si[11-2] azimuth.

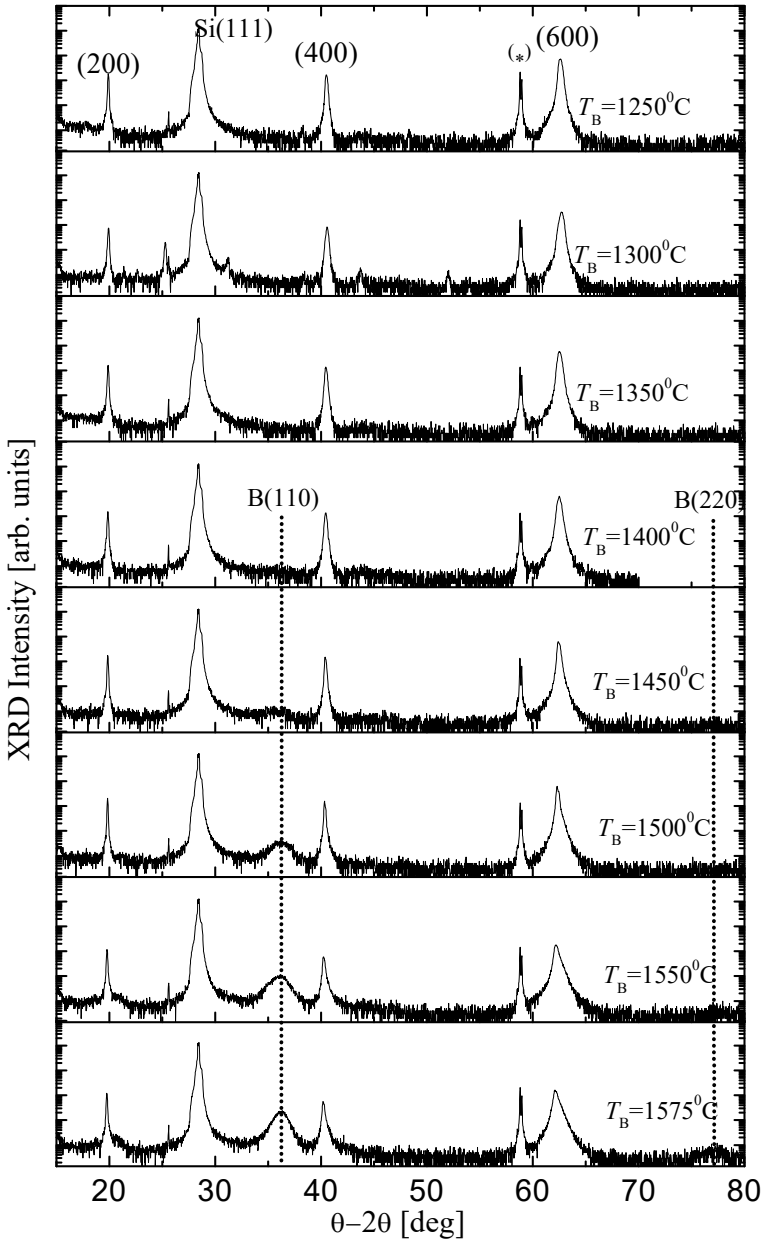

Fig.33 θ-2θ XRD patterns of B-doped $BaSi_2$ films grown at T_B=1250-1575 °C.

It can be supposed that the B-nano cluster influences the electrical properties of the *p-n* junction and can potentially resolve precipitation either by RTA or variation of growth temperature.

Figures 34(a)-(d) show AFM images of the epilayer topography corresponding to the samples grown with T_B=1450 °C, with lower B concentrations having an RMS value of 1.1 nm and higher B concentrations (T_B=1550 °C) obtained at RMS 1.7 nm conditions. It shows that the surface remains flat and smooth for low B-concentration than the higher B-concentration as shown in the 3D surface morphology, shown in Fig. 34(b)-(d). It can be speculated that the white clusters could arise due to B-atomic precipitation or segregation.

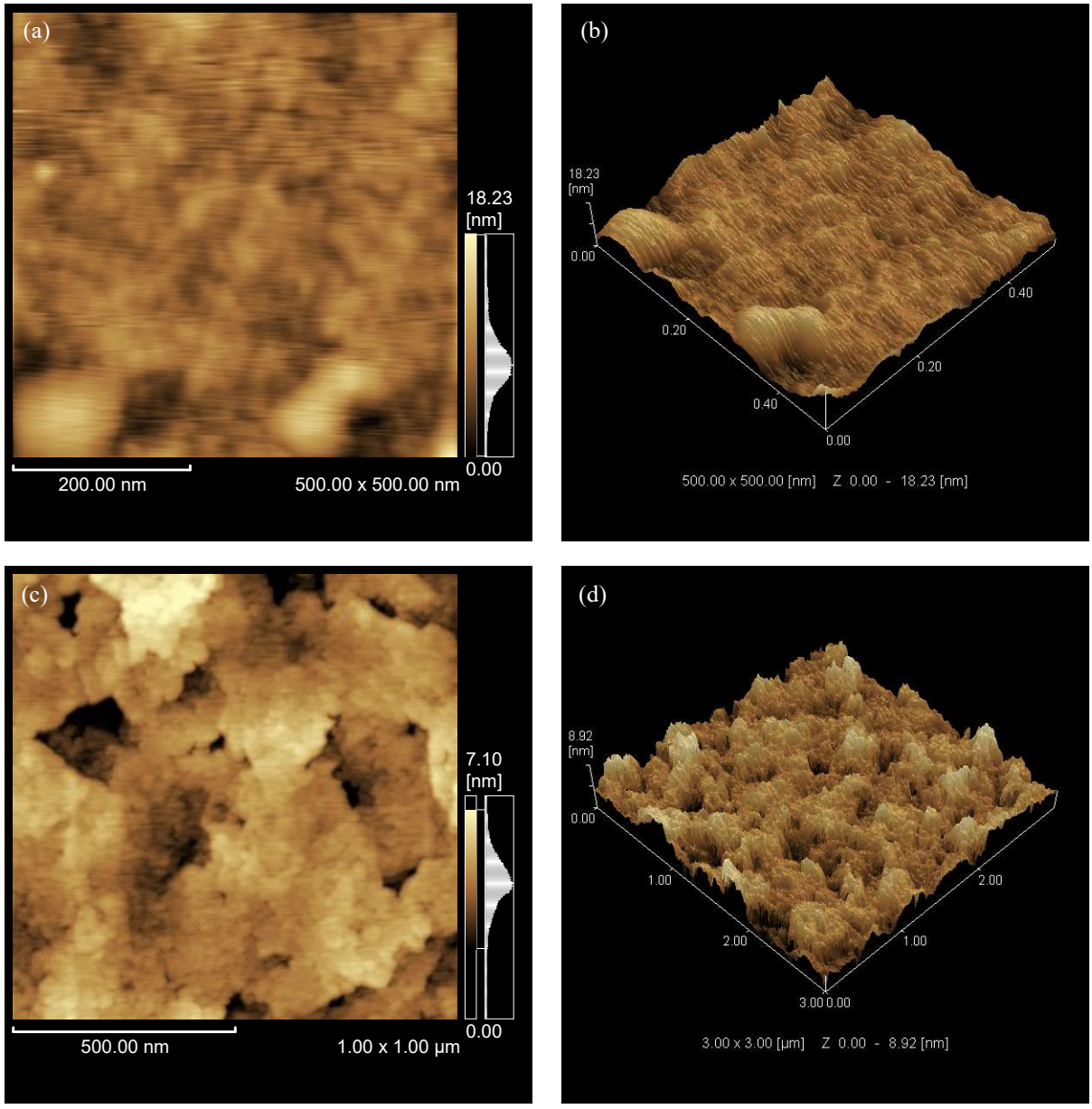

Fig. 34 B-doped $BaSi_2$ surface morphology of as-grown samples at (a)-(b) T_B=1450 ºC, having AFM images size 0.5 µm × 0.5 µm and (c)-(d) T_B=1550 ºC, having AFM image size of 1 µm × 1 µm in size.

3.2.2.2 Microstructure by Transmission Electron microscopy (TEM) observation.

Figure 35(a) shows a bright-field (BF) plan-view TEM image of the B-doped *p*-$BaSi_2$ grown at T_B=1450 ºC, and Ts=600 ºC. The incident electron beam direction was approximately parallel to the $BaSi_2$ [100] zone axis, but was slightly tilted in order to clearly see the GBs. After magnification of the image, it was observed that in the B-doped polycrystalline $BaSi_2$ thin film the B-clusters (nano-clusters) of approximately 3 nm were distributed equally over the sample. Because GBs are parallel to the surface normal, their contrast vanishes in the exact [100] zone axis. The $BaSi_2$ grain size is approximately 0.1–0.3 µm.

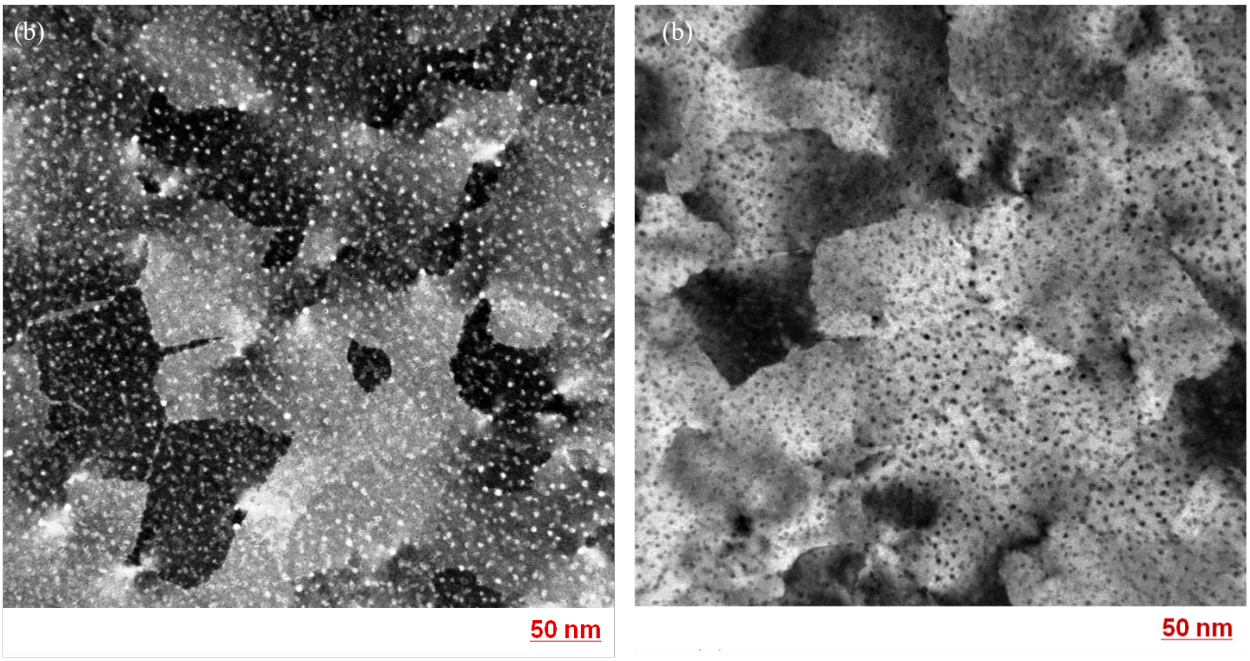

Fig. 35 (a) BF TEM image near the [100] zone axis of B-doped $BaSi_2$, and (b) Plan-view BF TEM image near the [100] zone axis of B-doped $BaSi_2$ with off-brag's condition for sample grown at T_B=1450 ºC, and Ts=600 ºC.

Figure 35(b) shows the BF image in the $BaSi_2$ [100] crystal zone axis neighborhood. Many fine particles of approximately 3 nm were also observed here, but show black contrast because crystallographic orientation (off Bragg conditions) is different from the field of vision for the image shown in Fig. 35(a). It can be speculated that these B-microstructures (black spot) could possibly arises due to the precipitation of B-atoms above the solid solubility limit in $BaSi_2$. There is no report available about the solid solubility limit for impurity doping into $BaSi_2$.

Figure 36(a) gives the comparison of DF TEM images among three different diffraction conditions. The middle diffraction pattern shown in Fig. 36(a), shows the SAED of $BaSi_2$ DF image in the exact $BaSi_2$ [100] crystal zone axis. In the crystallographic orientation of each crystal grain, there is a 120 degree rotation symmetry relation that cannot be distinguished on the diffraction pattern because the plane separation of the (011) side and the (002) side is extremely close.

Figure 36 presents the SAED pattern obtained from the area, including several $BaSi_2$ grains in the [100] zone axis. Considering that the GBs are caused by three different *a*-axis-oriented $BaSi_2$ epitaxial variants rotated from each other by 120 degrees with respect to the surface normal, the

(002),(011), and (020) spots can be grouped into threes, shown in blue, green, and red colors, respectively in Figs.36(b)-36(d). Considering the green and blue epitaxial variants, for example, the green (011) plane is parallel to the blue (002) plane. It is difficult to distinguish the green (011) plane from the blue (002) plane in the SAED pattern because the lattice spacing, d, are almost the same, with, $d_{(011)}$ =0.586 nm and $d_{(002)}$ = 0.579 nm.

The g vector shows contrast such that only <004>, namely crystal grain that satisfying the {004} diffraction electron condition, is bright in a dark field image (with a different field of vision for each diffraction vector).

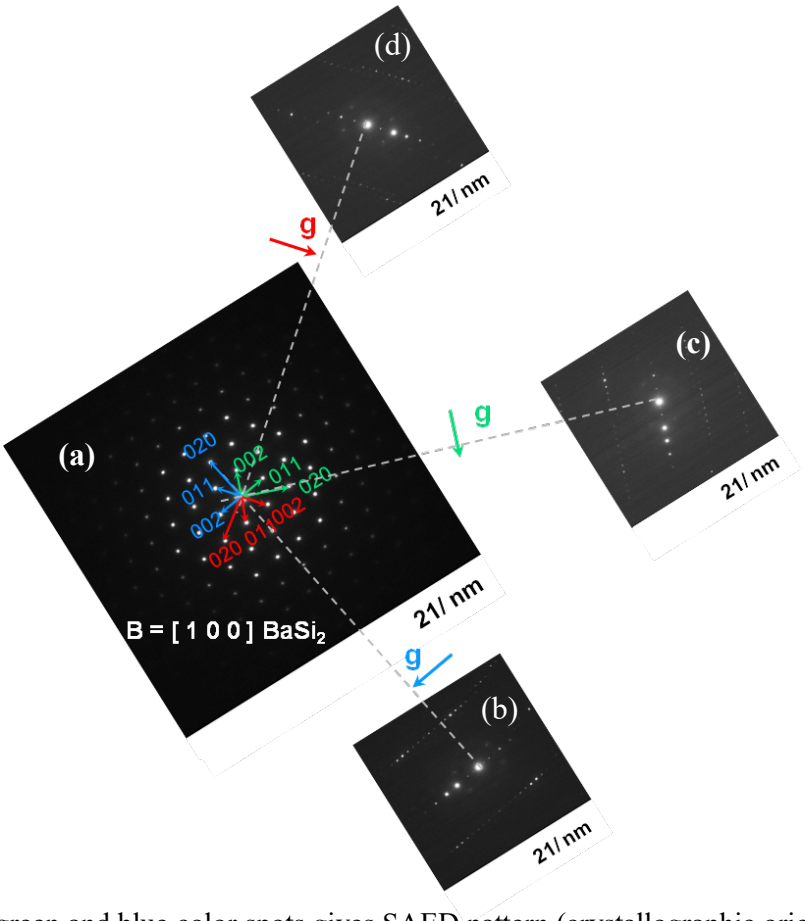

Fig. 36(a) red, green and blue color spots gives SAED pattern (crystallographic orientation) obtained from the area including several $BaSi_2$ grains in the exact [100] zone axis. SAED patterns obtained from single grain regions under two-beam diffraction conditions, where the diffraction vectors g were set to three different <004> directions as shown in Fig. 37(a), (b) and (c) respectively.

Figures 36(a)-(c) show SAED patterns obtained from single grain regions under two-beam diffraction conditions. The diffraction vectors g were set to be <004> for the three epitaxial variants shown by blue, red and green in Fig. 36(a). Under these conditions, the diffraction spot corresponding to the (004) plane becomes bright, as seen in Figs. 36(b)-(d), while others spots denoted by (00n) (n= ±1, ±2, ±3,…) can also be seen. These facts can help to distinguish the (002) plane from the (011) plane.

Figures 37(a)–(c) show DF plan-view TEM images using <004> plane reflections observed in the same sample region. The diffraction conditions of these DF images are the same as those in

Fig. 36. Under these conditions, B-doped $BaSi_2$ grains satisfying Bragg's condition of diffraction, indicated by the blue, red, or green-colored domain, are represented as being bright in these images. In other words, one of the three $BaSi_2$ epitaxial variants becomes bright in each figure corresponding to Fig. 37(d), which shows three epitaxial variants in $BaSi_2$. It should be noted that the superposition of bright regions in Figs. 37(a)–(c), cover the whole surface of B-doped $BaSi_2$. Contrast accomplished only with a bright crystal grain such that the g vector corresponds to <004> is shown, and the particle diameter is within the range of 0.2-0.3 nm. The B-doped $BaSi_2$ grain size is approximately 0.1–0.3 μm. The grain boundary is an infinite form and it shows that the clear crystal face could not be seen in this sample.

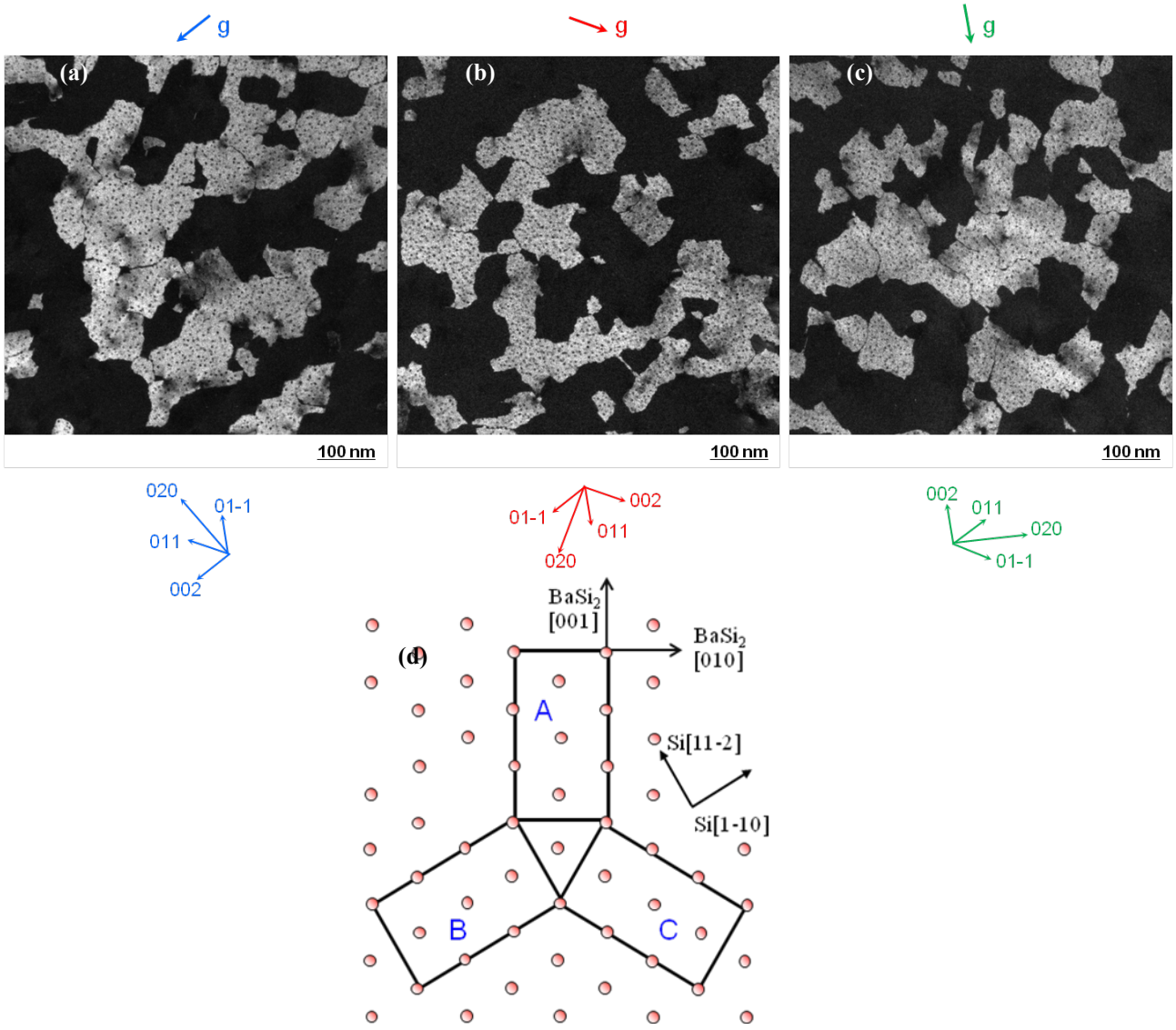

Fig. 37(a)–(c) DF TEM images under a two-beam diffraction condition. The diffraction vector g was set to be <004> for each epitaxial variant. Schematics of three epitaxial variant sof $BaSi_2$ are shown for the sample grown at T_B=1450 ºC, and Ts=600 ºC and (d) shows three epitaxial variant planes.

Figure 38 shows the BF image in the $BaSi_2$ [100] crystal zone axis neighborhood, for sample grown at T_B=1550 ºC, and Ts=600 ºC. Many fine particles of slightly larger size around 5 nm, were

observed here, as compared to the size of particles in Fig. 35, grown at T_B=1450 ºC and Ts=600 ºC. It can be speculated that size expansion of the B-microstructure (black regions) could possibly arises due to further increases of B-source temperature, which in return increases the precipitation of Boron atoms above the solid solubility limit in B-doped $BaSi_2$ this can be seen in the out-of-plane XRD pattern.

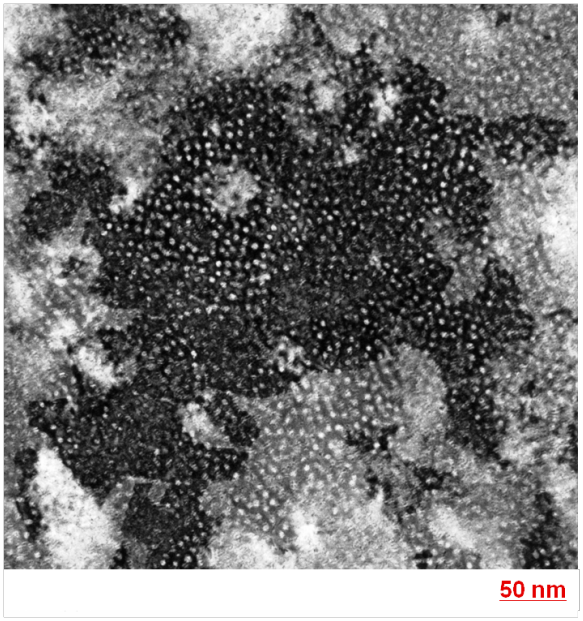

Fig. 38 Plan-view BF TEM image near the [100] zone axis of B-doped $BaSi_2$, for the as-grown sample at T_B=1550 ºC and Ts=600 ºC.

3.2.2.3 B-atomic concentrations in $BaSi_2$ as-grown samples by SIMS

Figure 39(a) shows the SIMS profiles of B atoms in samples A, C, and E. SIMS measurements revealed that the doped B atoms have relatively uniform distribution within the $BaSi_2$ layers. The average B concentration, N_B, was approximately 3×10^{20}, 2×10^{21} and 1×10^{22} cm^{-3} for samples A, C, and E, respectively.

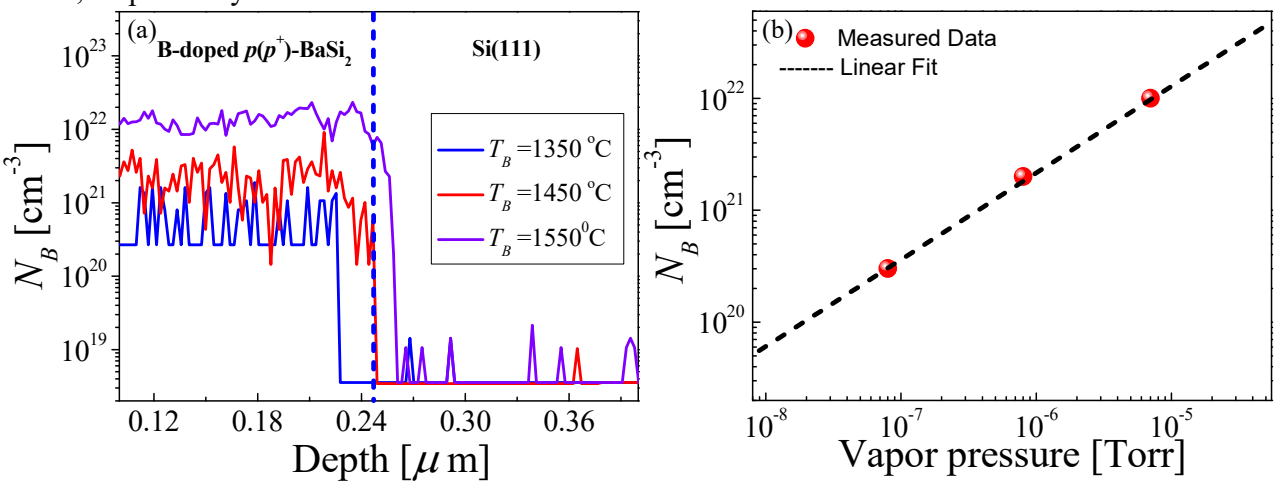

Fig. 39 (a) SIMS depth profiles of B-atoms and (b) B-density Vs vapor pressure in samples A, C and E, grown at T_B= 1350, 1450, and 1550 °C, respectively.

B concentrations in the SIMS profiles were corrected using reference samples, where a controlled number of B atoms were doped in the $BaSi_2$ films by ion implantations. The obtained B

concentrations are explained relatively well by the difference in vapor pressure of B as shown in Fig. 39(b). The N_B value in sample E was larger than that in sample C by 6 or 7 times. It is reasonable to think that the vapor pressure of B at 1550 °C is approximately 7 times larger than that at 1450 °C [13]. There is no diffusion tendency toward the substrate and very sharp edges were obtained at the hetro-interface.

3.2.2.4 Electrical Properties of B-doped $BaSi_2$ as-grown samples

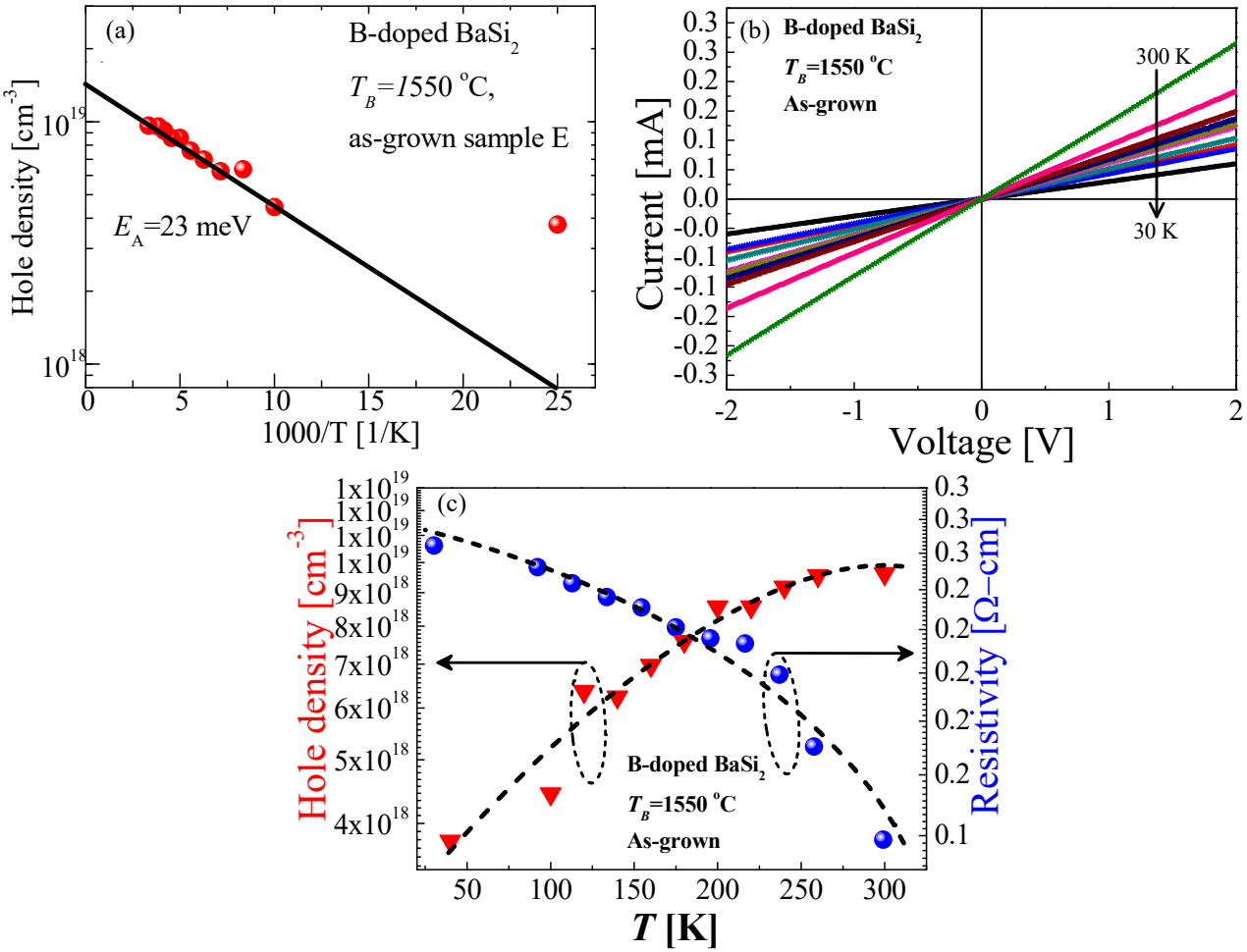

Fig. 40(a) hole concentration vs temperature for B-doped *p*-$BaSi_2$ as-grown sample grown at T_B=1550 °C (sample H), (b) Temperature dependence of *I-V* characteristics and (c) Temperature dependence of resistivity as well as hole concentration for B-doped $BaSi_2$ films grown at T_B=1550 °C.

B-doped as-grown $BaSi_2$ showed *p*-type conductivity for samples E-G. But the sample grown at T_B=1575 °C (G) is heavy-doped and might contain more precipitation than the sample grown at T_B=1550°C (E). Therefore, sample E was chosen for electrical investigation. Figure 40(a) shows temperature dependence of hole concentrations in as-grown sample E. The hole concentration reached 1.0×10^{19} cm^{-3} at RT, and then decreased with decreasing temperature until 27 K. The acceptor level, E_A, calculated using Eq. (6) was 23 meV.

$$p \propto \exp(-\frac{E_A}{2k_B T}) \qquad (6)$$

In equation 6, k_B is the Boltzmann's constant, and T the absolute temperature. The E_A value is much

smaller than those in Al-doped $BaSi_2$ (E_A=50, and 140 meV).[11] Such a shallow acceptor level of 23 meV could be the reason for heavily *p*-type doping in sample E as well.

Figure 40(b) gives the resistance between the two electrodes, which consists of contact resistance at the $BaSi_2$/AuCr and $BaSi_2$ bulk resistance. The resistance decreases by a factor of 3 when the temperature decreases from 300 K to 27 K during I-V measurement. This change can also be explained by the change in resistivity of B-doped $BaSi_2$ as shown in Fig. 40(c). This means that the contact resistance is smaller than the bulk resistance in this temperature range, thereby showing that good electrical contacts are formed on the surface.

For other as-grown samples other than E-G, however, it was difficult to obtain reliable carrier concentrations and mobilities due to difficulties in forming ohmic contacts on the surface. During TEM investigation the nano-microstructures of the B-crystals were found and conduction of RTA treatment for a limited number of samples was decided. In the next section the RTA experiments and the detailed investigations of the RTA treated samples are discussed.

3.3 RTA TREATMENT OF *in-situ* B-DOPED $BaSi_2$ GROWN AT T_S=600 °C, T_B=1350-1550°C

According to what was previously established about the as-grown samples other than E-G, it is difficult to obtain reliable carrier concentrations and mobilities due to the difficulties in forming ohmic contacts on the surface. During the XRD pattern and TEM observation the nano-structure of precipitated B-crystal were found and was realized by using the RTA for B-activation in the B-doped $BaSi_2$ thin film.

3.3.1 Experimental Procedures

RTA was performed for samples A, C, E and G under Ar at 800 °C for 0.5, 1 and 2 min for electrical activation of B-atoms in $BaSi_2$. The heating rate was 40 °C/s during RTA treatment. The electrical properties were characterized by Hall measurements using the van der Pauw method. The applied magnetic field was 0.7 T, normal to the sample surface. A few samples were also investigated by XRD, AFM and TEM to see the influence of RTA on the crystalinity and boron precipitation.

3.3.2 *Crystallininty by XRD and AFM*

After RTA treatment, the crystalline quality of the B-doped $BaSi_2$ thin films was uncertain and therefore XRD measurement was conducted. Figure 4 shows the θ-2θ XRD patterns of B-doped $BaSi_2$ films grown with T_B=1550 °C after RTA treatment. The diffraction peaks of (100)-oriented $BaSi_2$, such as (200), (400) and (600), are dominant in the grown sample even after RTA treatment.

Figures 42(a)-(b) show that RTA gives rise to the isolated, large size islands, which are vertically aligned and more regular in nature compared to the as grown sample shown in Figs. 34 (c)-(d). This indicates that RTA is a good technique to improve the crystalline quality of the grown sample.

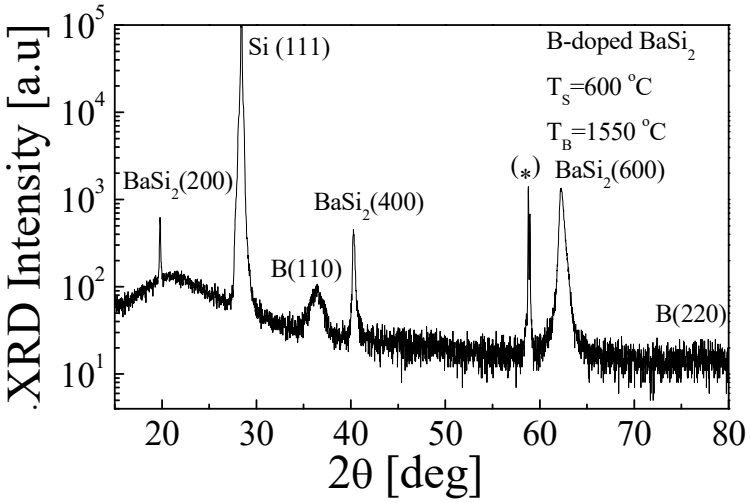

Fig. 41 θ-2θ XRD patterns of B-doped p-$BaSi_2$ for, the sample grown with T_B=1550 °C and T_S=600 °C after RTA treatment.

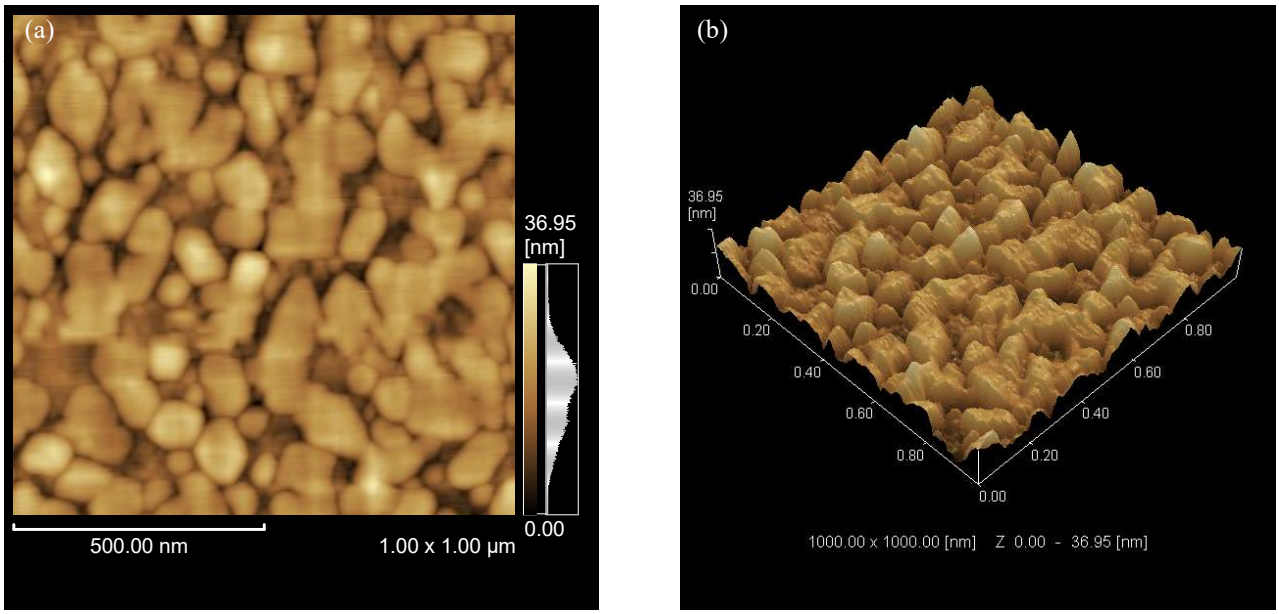

Fig. 42 B-doped $BaSi_2$ surface morphology: after RTA treatment, of the grown sample at T_B=1550 °C, T_S=600 °C having AFM images size 1 µm × 1 µm and (b), 3D-AFM image of the same sample.

3.3.3 *Microstructure Characterization by TEM*

In Fig. 43(a) cracks and curvature were found in some part of thin-film during TEM, observation in the [110] direction of $BaSi_2$ and therefore complete observation could not be accomplished. It can be speculated that the cracks were caused by RTA due to the difference between thermal expansion coefficient of Si and $BaSi_2$ at the hetro-interface. However, the particles of the dark contrast of Fig. 43(a) are in [1-10] direction (SAED reference, Fig 44(a)), and the large grain size of $BaSi_2$ can be estimated at about 0.5 micrometer from these results, as indicated by the "A" and "B" zones in Fig. 43(b).

Figure 44(a) gives the SAED pattern in [1-10] zone axis of B-doped p^+-$BaSi_2$ after treatment. The bright diffraction spot oriented in {111} sides is also observed, and it is considered that the cluster origin containing boron and the same could be seen in the XRD peaks like B(110)

and B(220) as shown in Fig. 33. Precipitation free B-doped *p*-layer of $BaSi_2$ is inevitable for solar cells.

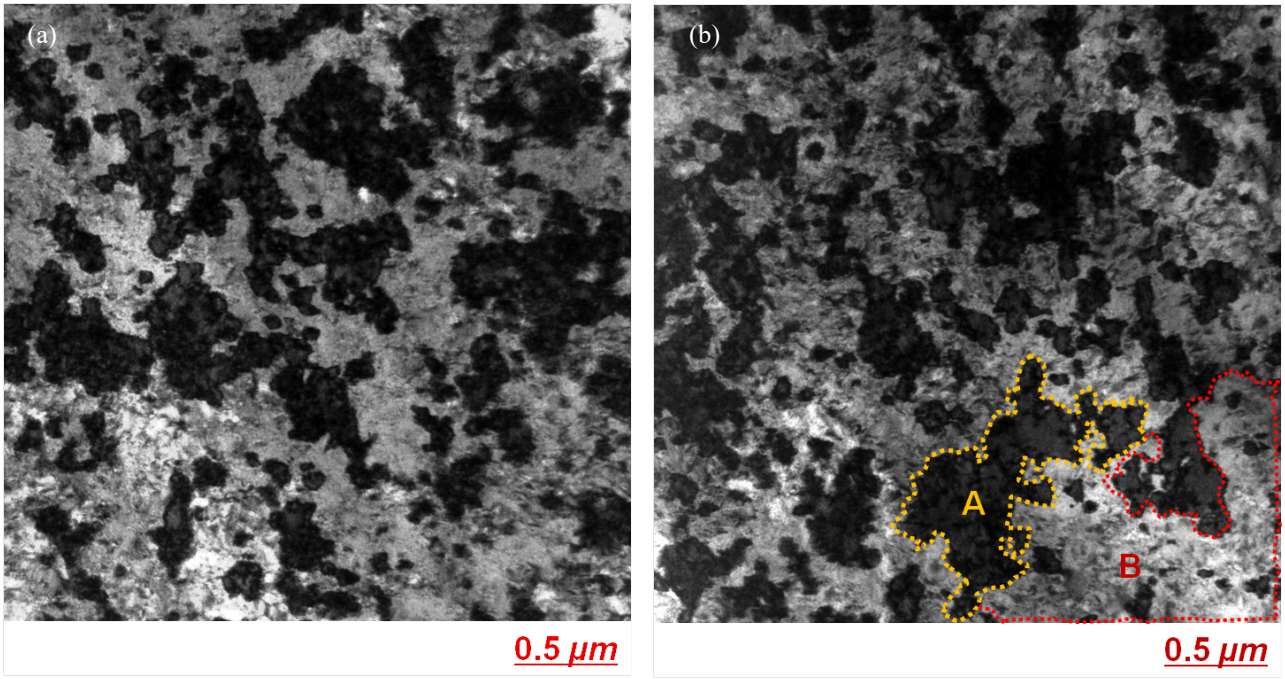

Fig. 43(a) plane-view DF TEM image near the[1-10] zone axis of $BaSi_2$, grown with T_B=1550 ºC, T_S=600 ºC after RTA and (b) Plan-view DF TEM image near the[100] zone axis of $BaSi_2$ with off Bragg condition.

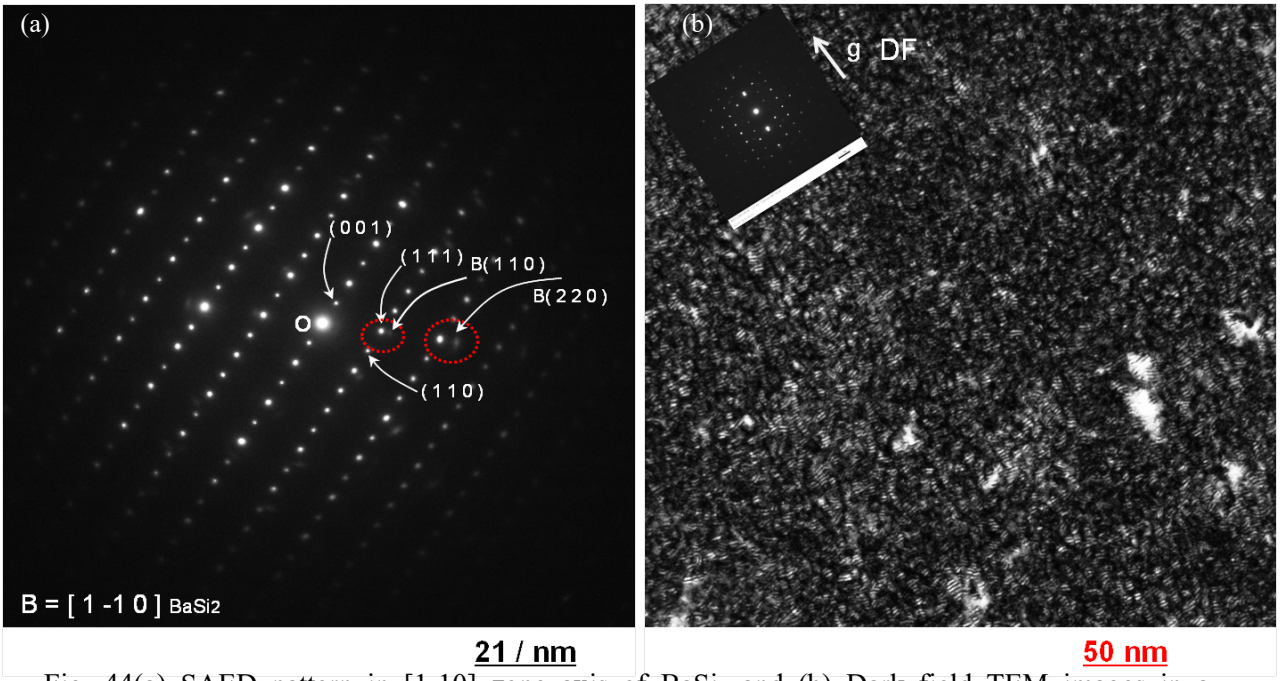

Fig. 44(a) SAED pattern in [1-10] zone axis of $BaSi_2$ and (b) Dark field TEM images in a two-beam diffraction condition in case of sample prepared with T_B=1550 ºC, T_S=600 ºC after RTA.

Figure 44(b) gives the DF image using {020}-{013} reflection from p^+-$BaSi_2$. In this image the p^+-$BaSi_2$ sample was kept a little tilted from the Bragg conditions during observation and emphasized on the diffraction pattern originated from the precipitated boron cluster, having diameter of 5 nm. The inset of Fig. 44(b) gives the SAED pattern in [1-10] zone axis of the same

sample. The TEM observation implies that we still have the precipitated boron atoms in the grown sample even at T_B=1450ºC and T_S=600 ºC. Therefore, it was realized to estimate the B-activation efficiency under these growth conditions. In the next subsection, the detailed model of activated B-atoms in $BaSi_2$ is presented.

3.3.4 Electrical Properties of in-situ B-doped $BaSi_2$ after RTA Treatment

For boron particle density estimation, we suppose that the inter-particle (precipitated boron) distance is the same in the 3D directions. From this the distance L can easily be estimated by using nm-scale ruler. The density of such particles $d_{B\text{-}particle}$ can also be approximated by a $1/L^3$ formulism, as shown in Fig. 45.

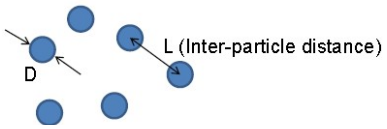

Fig.45 model of Boron particles (Cluster) in B-doped *p*-$BaSi_2$.

The net volume (V) containing inactivated boron (cluster particle) as well as activated Boron in $BaSi_2$ can be written as:

$$N_B = V \times d_{B(SIMS)} = V_B \times d_{B\text{-}particle} + V_{BaSi_2} \times d_{B\text{-}in\text{-}BaSi_2}$$
$$\text{where, } V_{BaSi_2} = V - V_B, \text{and } V_B = 4\pi \tfrac{4\pi}{3}(\tfrac{D}{2})^3 \times d_{B-particle} \times V$$
$$\text{and, } d_{B-particle} \approx \tfrac{1}{L^3}, \text{and } V_B = \tfrac{4\pi}{3}(\tfrac{D}{2})^3 \times d_{B-particle} \times V$$
$$d_{B-in-BaSi_2} = \frac{[V \times d_{B(SIMS)} - V_B \times d_{B-in-particle}]}{V - V_B} \quad (7)$$

In equation 7, $d_{B(SIMS)}$ is the density of holes measured by SIMS and $d_{B\text{-}in\text{-}particle}$ is the number of boron atoms in the unit cell. In equation 7 D is the Boron particle dia (5nm), L is the Inter-particle distance (7nm), p is hole concentration=2×10^{20} cm^{-3}, $V_{B(SIMS)}$=2×10^{21} cm^{-3}, $d_{B\text{-}in\text{-}particle}$=36/0.706 nm^{-3} and it is considered that 36 Boron atoms in a unit cell have a volume of 0.706 nm^{-3}. The activation efficiency of boron was calculated using these data in Eq. (7), and it was found that approximately 10 % the boron atoms was activated in the grown sample.

Table II Sample preparation: Growth temperature (T_S), B-source temperature (T_B), measured hole concentration (p) and mobility (μ_p) are shown.

Sample	T_S (°C)	T_B (°C)	p (cm^{-3})	μ_p ($cm^2/V\cdot s$)
A	600	1350	-	-
B	600	1400	-	-
C	600	1450	-	-
D	600	1500	-	-
E	600	1550	1.0×10^{19}	6.3
F	600	1575	2.5×10^{18}	8.3
G	650	1450	6.5×10^{19}	0.8

Figure 46(a) presents the dependence of hole concentrations on RTA duration, t_{RTA}, for samples A, C, E, and G. The growth conditions of these samples are given in the same figure. The hole concentration increased from 8.5×10^{16} to 6.0×10^{17} cm^{-3} for sample A when t_{RTA} was increased

from 0.5 to 2 min. This behavior was similarly observed from 5.0×10^{17} to 1.6×10^{19} cm^{-3} for sample C. These results revealed that RTA is a very effective means to activate the B atoms in $BaSi_2$, as reported in other materials such as Si, GaAs, GaN, and ZnO [45-48].

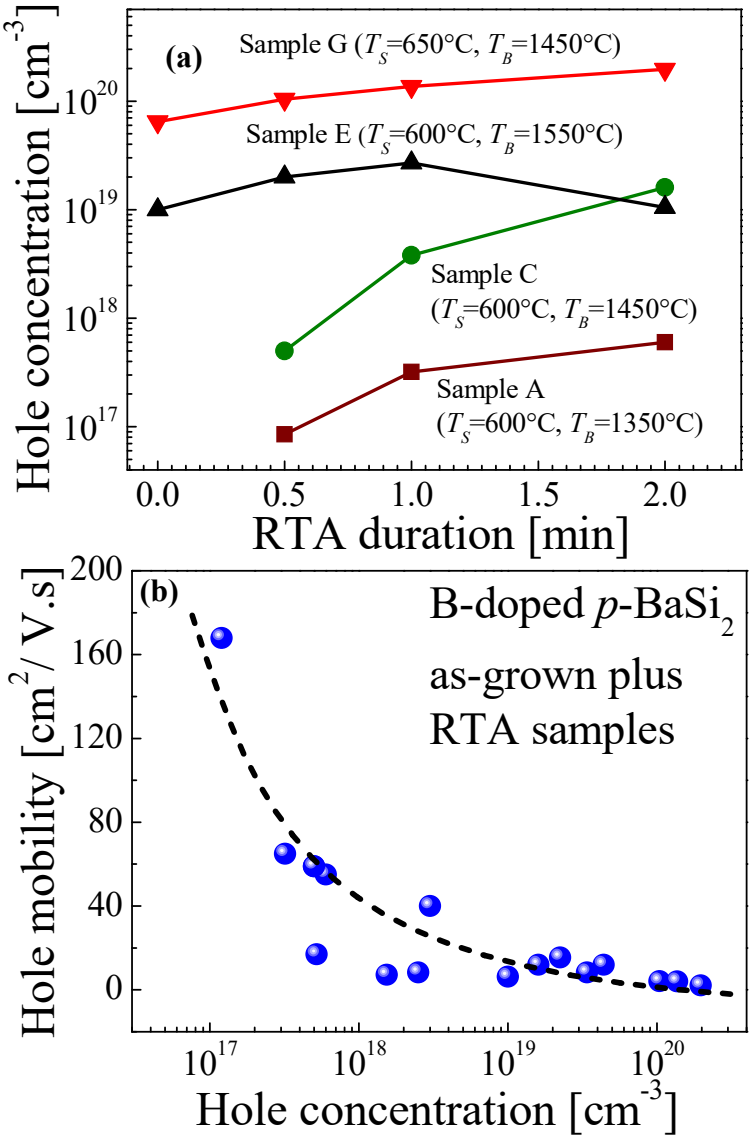

Fig. 46(a) dependences of hole concentration on t_{RTA} for samples, A, C, E, and G and (b) relationship of measured mobilities and hole concentrations for B-doped p-$BaSi_2$, grown at T_B=1350-1575 °C.

For sample E, the hole concentration increased from 1.0×10^{19} to 2.7×10^{19} cm^{-3} after a 1 min RTA, but decreased down to 1.1×10^{19} cm^{-3} by further annealing. This might be caused by low T_S for too large N_B in sample E. We therefore decided to increase T_S from 600 to 650 °C, and decrease N_B from 1×10^{22} to 2×10^{21} cm^{-3} for sample G. As shown in Fig. 46(a), the hole concentration was increased further up to 2.0×10^{20} cm^{-3} after the 2 min RTA in sample G. This value is the highest ever achieved for $BaSi_2$, indicating that a higher T_S value improved the electrical activation efficiency of B atoms. The activation efficiency of B atoms in sample G can thus be estimated to, p/N_B $=2.0\times10^{20}/2\times10^{21}\cong 10\%$ after the 2 min RTA. The obtained p and hole mobility μ_p were summarized in Fig. 46(b). As the hole concentration increases, the mobility decreases and this trend is usually predicted by ionized impurity scattering in conventional semiconductors. The hole

concentration of B-doped $BaSi_2$ is well controlled in the range between 10^{16} and 10^{20} cm^{-3} at RT by changing the temperature of the B-Knudsen cell crucible and RTA treatment.

CHAPTER 4: CONDUCTION MECHANISMS IN IMPURITY-DOPED $BaSi_2$ FILMS

In this chapter detailed studies about the conduction mechanisms and carrier transport mechanisms are discussed. The most suitable and optimized samples from each impurity-doped $BaSi_2$ thin film based on the crystalline quality and electrical characterization at RT, were chosen. It was not clear, whether carrier transport mechanisms in impurity doped $BaSi_2$ could be well explained by Shklovskii-Efros (SE)-type and Mott-type variable range hopping (VRH) conduction. Therefore, the conduction mechanisms were studied in impurity-doped $BaSi_2$ to quantify the existence of defects levels in the forbidden energy band gap.

4.1 BACKGROUND OF HOPPING CONDUCTION IN SEMICONDUCTOR

It is very common in semiconductors that exhibit intrinsic conductivity from the valence band to the conduction band at sufficiently high temperatures caused by thermal activation of carriers. But in case of a wide band gap material a rapid decrease of this kind of conduction process at lower temperatures could happen. Therefore, shallow impurities levels can be the most important provider of free carriers as their ionization energy is much lower than the band gap energy, as shown in Fig. 47(a).

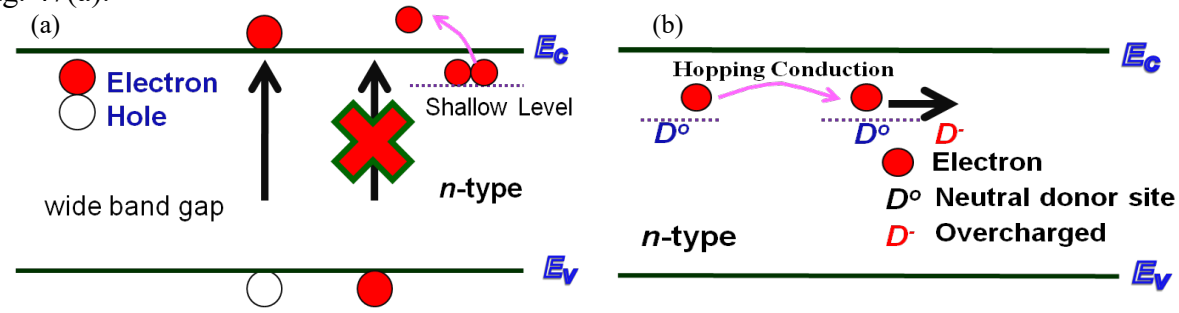

Fig. 47(a) transport mechanism at low temperature and (b), Nearest neighbor hopping illustrated in a *n*-type semiconductor. The electron is transferred from a (D^o) donor to a neighbor (D^o) donor by creating an overcharged impurity (D^-).

At low temperatures the thermal activation energy is so small that the carriers are re-captured by the impurities atoms. This is a gradual process known as freeze-out process.

If we further decrease the temperature, then the impurities are completely frozen out and the only prominent transport phenomenon could be possible due to hopping conduction. In case of non-compensated *n*-type semiconductor the hopping conduction could be happen, and the electron is removed from a neutral donor site (D^o) and moves to a neighboring neutral donor site, where it creates an overcharged impurity (D^-) [49], as shown in Fig. 47 (b).

The conductivity σ caused by this kind of thermally activated process, can be characterized by an activation energy ε_2 as:

$$\sigma = \sigma_2 \exp(-\frac{\varepsilon_2}{k_B T}) \tag{8}$$

In Equation 8, σ_2 and ε_2 depend on the average distance between the impurities atoms.

When the donor concentration is slightly compensated by a frozen acceptor doping in *n*-type semiconductor then another type of hopping conduction mechanism can happen in the energy band gap. In this mechanism, the acceptors are ionized with carriers from the impurity band, and leaving behind positively charged donor sites in the impurity band even at the lowest temperature. In such situation carrier hopping effect can be observed, where the electron of a neutral donor site is transferred to a positively charged neighbor donor site. This process is assisted by the absorption and emission of a phonon, lifting the electron to an excited intermediate state as illustrated in Fig. 48(a).

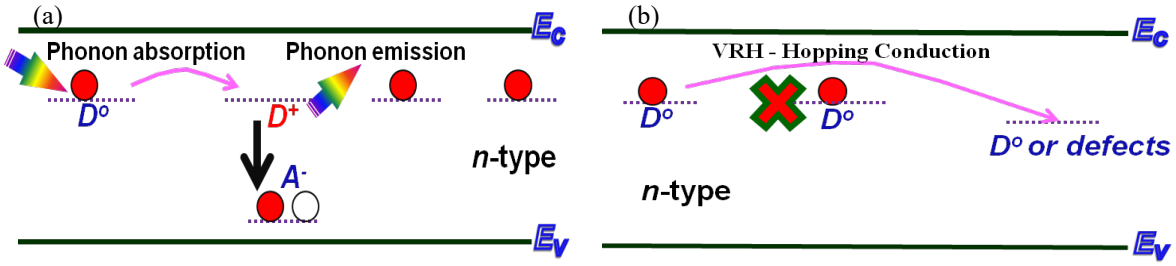

Fig. 48(a) nearest neighbor hopping conduction illustrated in a *n*-type semiconductor band gap. The electron is transferred from a (D^o) donor to a (D^+) donor by the assistance of a phonon absorption and emission process and (b) variable range hopping (VRH) conduction illustrated in a *n*-type semiconductor. The electron is transferred from a (D^o) donor to a distant site (D^o) donor by creating an overcharged impurity (D^-).

Figure 47(a) transport mechanism at low temperature and (b) nearest neighbor hopping illustrated in a *n*-type semiconductor. The electron is transferred from a (D^o) donor to a neighbor (D^o) donor by creating an overcharged impurity (D^-).

The conductance of Fig. 48 (a), can be well described by thermal activation energy (ε_3) [50,51] as:

$$\sigma = \sigma_3 \exp(-\frac{\varepsilon_3}{k_B T}) \qquad (9)$$

This nearest neighbor hopping process is the most important hopping conduction mechanism within the semiconductor devices.

At very low temperatures another important hopping transport process can be occurred, it is known as variable-range hopping mechanism. When the thermal energy (k_BT) becomes very low then the hopping carrier may not find a suitable energy state within the possible range at neighbor impurity sites. In this situation the carrier may be transferred to a more distant site (range) despite of the small wave-function overlap [51,52] as shown in Fig. 48(b). The variable-range hopping mechanism is very important to be investigated in impurity doped regions of Si-thin film solar cells and $BaSi_2$ thin film solar cells.

The conduction mechanism can be investigated from the temperature dependence of resistivity ρ, of impurity-doped $BaSi_2$ thin films. In general, at low temperatures, carriers in a system having disorder caused by, for example, careers are thought to hop from one impurity atom to the next, and the Coulomb potential around the impurity atom is overcome by means of thermal

energy. The conductivity in such a system is determined by a hopping transport, where the resistivity ρ has been found to follow the law $\log \rho = (\frac{T^*}{T})^{\frac{1}{q}}$, where T^* is the characteristic temperature, and q is the parameter determining the Mott-type (q=2) or the Shklovskii–Efros (SE) type (q=4) variable-range hopping (VRH) conduction [51–53].

4.2 CONDUCTION MECHANISMS IN IMPURITY –DOPED $BaSi_2$ THIN FILMS

Conduction mechanisms at low temperature, is an interesting technique to find the clue of defects levels as well as hopping conduction in the forbidden energy band gap. However, the number of experimental reports available on the subject of conduction mechanism in doped $BaSi_2$ has been nil. The main objective of this research is to discuss about the conduction mechanisms in impurity doping of Sb, In, Ga, Al, Ag, Cu, and B into $BaSi_2$ thin films and then to qualify some of the impurity-doping candidates for Solar cell application. In the next subsection experimental procedures are discussed.

4.2.1 Experimental Procedures

An ion-pumped MBE system equipped with standard Knudsen cells was used for Ba, Al, Ga, In, Sb, Ag, Cu, and B and an electron-beam evaporation source was used for Si. Electrical measurements were conducted using high-resistivity floating-zone *p*-Si(111) (ρ=1000–6000 Ω·cm) substrates. All the substrate were washed and cleaned by standard procedure as mentioned in section 2.1. After cleaning the Si(111) substrate at 850 °C for 30 min in ultrahigh vacuum, a well-developed 7×7 reflection high-energy electron diffraction (RHEED) pattern was confirmed. RHEED patterns were observed along the [1–10] azimuth of the Si(111) substrate.

MBE growth of Cu- or Ag-doped $BaSi_2$ films was carried out as follows. First, a 10 nm thick $BaSi_2$ epitaxial film was formed on Si(111) at 550 °C by RDE, which was then used as a template for the $BaSi_2$ over layers. Next, Ba, Cu (or Ag), and Si were co-evaporated to form Cu (or Ag)-doped $BaSi_2$ at 600 °C by MBE. The thickness of the grown layers including the template was 230-310 nm. The amount of Cu (or Ag) atoms doped in $BaSi_2$ was varied by changing the temperature of the Cu (T_{Cu}) and Ag (T_{Ag}) sources. The ratio of the Cu to Ba vapor pressure (Cu/Ba ratio) was varied from approximately 10^{-4} to 1 by changing T_{Cu} from 800 to 1200 °C. The ratio of the Ag to Ba vapor pressure (Ag/Ba ratio) was varied from approximately 10^{-5} to 1 by changing T_{Ag} from 600 to 900 °C. The Ba source temperature was fixed at around 500 °C and Sb, In, Al, and Ga-doped $BaSi_2$ films were also prepared for transport studies using various source temperatures. Details on the procedures for the MBE growth of Sb, In, Al, and Ga-doped $BaSi_2$ films have been reported elsewhere [17,18]. Table III summarizes the carrier types and carrier concentrations in the impurity-doped $BaSi_2$ films used for the transport studies. One sample was selected from each impurity-doped $BaSi_2$ film, as shown in Table III, and the temperature dependence of resistivity was measured at temperatures between 20 and 300 K.

The crystal quality of the grown layers was characterized using X-ray diffraction (XRD) and RHEED. The diffraction peaks of (100)-oriented $BaSi_2$, such as (200), (400) and (600), are dominant in the θ-2θ XRD patterns, and other diffraction peaks other than those of (100)-oriented

for all impurity doped-$BaSi_2$ thin film samples. For electrical measurement, 1 mm diameter Au/Cr electrodes were evaporated on the sample film. The carrier type, carrier concentration and mobility were characterized by Hall Effect measurements using the van der Pauw method. A magnetic field of approximately 0.2 T was applied normal to the sample surface. Ba source temperature was fixed at around 500 °C. Sb, In, Ga, and Al-doped $BaSi_2$ films were also prepared for transport studies using various source temperatures. Details on the procedures for the MBE growth of Sb, In, Al, and Ga-doped $BaSi_2$ films have been reported sec 2.1. The Ag, Cu and B-doped $BaSi_2$ samples growth procedure are given in section 2.1, 2.2 and 3.2 respectively. Table III summarizes the carrier types and carrier concentrations in the impurity-doped $BaSi_2$ films used for the transport studies. The conductivity type of the Si substrates and the temperatures of impurity sources were also described.

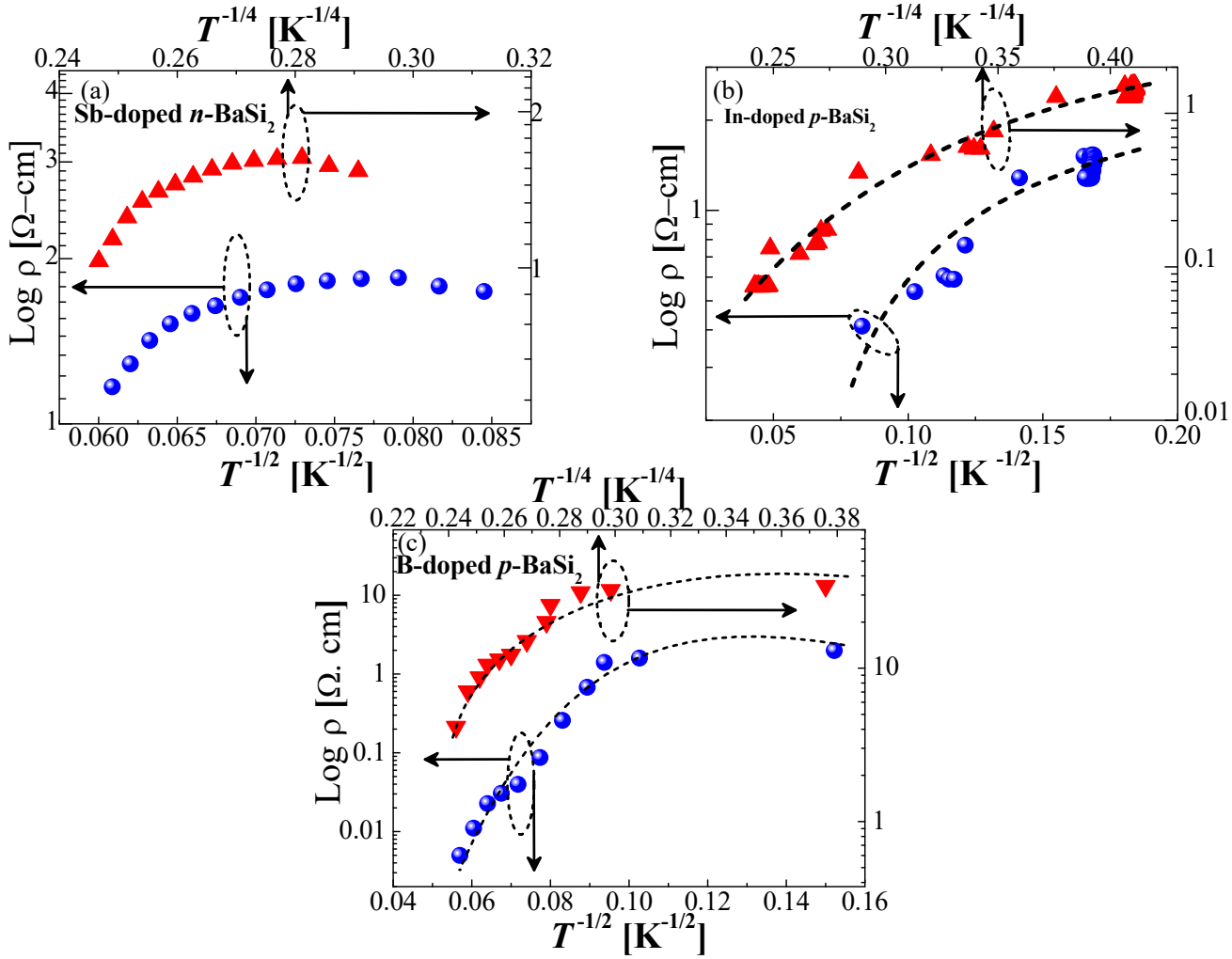

Fig. 49, Logarithmic dependence of resistivity on $1/T^{1/2}$ and $1/T^{1/4}$ for (a) Sb-doped *n*-type (b) In-doped *p*-type and (c) B-doped *p*-type $BaSi_2$, which depict non-linear behavior.

One sample was chosen from each impurity-doped $BaSi_2$ films, as shown in Table III, and the temperature dependence of resistivity was measured at temperature between 20 and 300 K. In order to clarify the influence of the high-resistive thick (500 µm) FZ-Si substrates on the measured electrical properties of impurity-doped $BaSi_2$ films, we also fabricated silicon-on-insulator (SOI) substrates with approximately 0.7-µm-thick Si layers with a (111) orientation.

Here, the SOI substrate was formed by bonding together the n-FZ-Si(111) substrate (ρ=1000–6000 Ω·cm) and a quarts substrate. Following bonding, the Si substrate was thinned to approximately 0.7 μm by grinding mechanically and by chemical mechanical polishing processes. Detailed data of electrical characterizations of the samples are given in Table III for impurity (Sb, In, Ga, Al, Ag, and Cu)-doped $BaSi_2$ films at RT. Each sample was selected from each impurity-doped $BaSi_2$ film, Sb, In, Ga, Al, Cu, Ag and B-doped $BaSi_2$, and the temperature dependence of resistivity was measured at temperatures between 20 and 300 K.

4.2.2 Results and Discussion

As a beginning, we examined the results on Al-doped $BaSi_2$ films on the *n*-type SOI substrate.

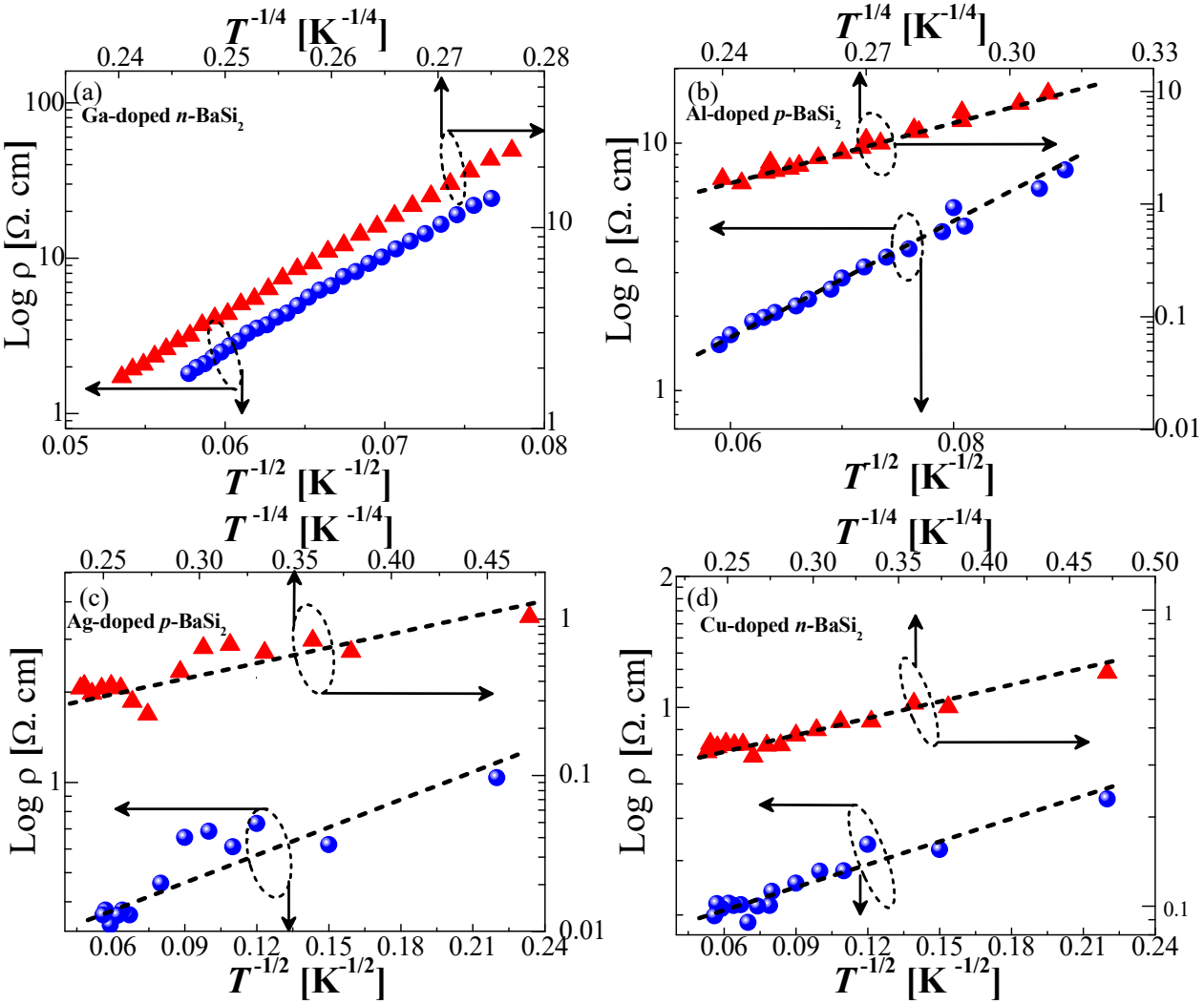

Fig. 50, Logarithmic dependence of resistivity on $1/T^{1/2}$ and $1/T^{1/4}$ for (a) Ga-doped *n*-type (b) Al-doped *p*-type, (c) Ag-doped *p*-type and (d) Cu-doped *n*-type $BaSi_2$, which depict linear behavior.

Since the resistance of the 0.7-μm-thick *n*-Si layers on the SOI substrate is approximately 700 times greater than that of the 500-μm-thick *n*-type FZ-Si, we would expect to see differences among the samples if the influence of current flow in the *n*-Si substrate is significant.

As shown in Table III, the difference in the measured hole concentrations between samples D and G is small. It is true that we cannot exclude all the influences of the 500-μm-thick FZ-Si

substrate on the measured values in samples A–F; however it is reasonable to suppose that the influence is not so significant.

Table III Carrier type and concentration of impurity (Sb, In, Ga, Al, Ag, Cu& B)-doped $BaSi_2$ films.

Sample	Impurity	Carrier type	Carrier concentration at RT (cm^{-3})
A	Sb	n	3×10^{19}
B	In	p	2×10^{17}
C	Ga	n	1×10^{16}
D	Al	p	7×10^{16}
E	Ag	p	3×10^{16}
F	Cu	n	1×10^{19}
G	B	p	1×10^{19}

Figures 49(a)-(c) shows the logarithmic dependence of resistivity on both $1/T^{1/2}$ and $1/T^{1/4}$ for Sb, In, B-doped $BaSi_2$, respectively, where non-linear behaviors were observed for Sb, In and B-doped $BaSi_2$, which confirmed that the carrier transport could not be explained SE-type and VRH conduction. In contrast, the linear behaviors were observed for Ga, Al, Ag and Cu as shown in Figs. 50(a), (b), (c) and (d) which indicates that the carrier transport in the films can be explained by SE-type and VRH conduction. However, both types of hopping conduction are observed in Ga, Al, Ag, and Cu-doped $BaSi_2$, which suggests that there is a certain amount of defect levels in the forbidden energy gap. Both types of conduction mechanism have been extensively studied [33,34].

CHAPTER 5: OPTMIZATION OF B-DOPING AND *P-N* JUNCTION OF $BaSi_2$ THIN FILM SOLAR CELLS

Kobayashi *et al.* established that the electron concentration of Sb-doped *n*-$BaSi_2$ was well controlled in the range between 10^{17} and 10^{20} cm^{-3} at RT [18]. In chapter 3 it was also established that the hole concentration of B-doped *p*-$BaSi_2$ was controlled in the range between 10^{16} and 10^{20} cm^{-3}. It is also established that the B-doped $BaSi_2$ could be a good choice for different region of *p-n* junction of $BaSi_2$ Solar cells from Group-III-A. However, previous studies have been encumbered by the presence of precipitated boron cluster from elemental boron doping source with low substrate temperature as well as high B-source temperature. These two factors led to incorporation of defects, precipitation and impairing of crystalline quality (Deterioration of electrical properties with small activation efficiency of B-doped $BaSi_2$)**.** It is also important to grow high quality of *p-n* junction having no precipitation of B-clusters and large grain. Diffusion as well as segregation phenomena are also important to be investigated. It is therefore necessary to find, the optimum growth condition, for B-doped $BaSi_2$, so that B-precipitation free p^+-layer could be accomplished. The influences of B-doping on the energy band gap shrinkage and acceptor energy level in B-doped BaSi2 are useful information for *p-n* junction solar cell application

5.1 BACKGROUND

Conversion efficiency is theoretically determined by the energy band gap of the semiconductor materials used. The band gap strongly depends on the careers concentration and good crystalline quality. In this persuasion, the detailed investigation of B-doped $BaSi_2$ thin films ware accomplished in chapter-3. It has been established that the hole concentration of B-doped *p*-$BaSi_2$ was well controlled in the range between 10^{16} and 10^{20} cm^{-3} and the highest hole concentration over 10^{20} cm^{-3} were achieved fist ever. However, the B-precipitated sample gives acceptor energy level of about 23 meV, but we need the acceptor energy level having no B-precipitation.

Therefore, it was observed by TEM observation, that B-doped $BaSi_2$ shows precipitation of B-atoms and B-atoms were not fully activated as well. These precipitated B-atoms could possibly degrade the electrical properties of the thin film solar cell. Therefore it was seriously realized to overcome the B-precipitation and find solid solubility limit of B-atoms in the host $BaSi_2$ thin films. Fully activated B-atoms in $BaSi_2$ could give most reliable energy band gap, acceptor energy level and hole concentrations for solar cell application. In the next section, the sample preparation for band gap measurement is presented in detail.

5.2 MBE Growth of B-doped *p*-$BaSi_2$ on SOI for Energy Band Gap Measurement

Recent achievements in elucidation of the photoresponse properties of $BaSi_2$ epilayers on Si(111) and polycrystalline $BaSi_2$ layers on SiO_2 have increased our interest in this material [14,16]. However, uncertainties remains in the experimentally obtained band gap values and absorption coefficient of un-doped $BaSi_2$ as well as impurity doped $BaSi_2$. In the case of B-doped and Sb-$BaSi_2$ on a Si(111) substrate, however, reliable absorption measurements and energy band gap have yet to be conducted because the thick Si substrate absorbs most of the incident light in a transmission

configuration. In our previous work, polycrystalline $BaSi_2$ film on a transparent fused silica substrate covered with polycrystalline Si layers was prepared. It was reported that the absorption coefficient value could exceeds 10^4 cm^{-1} at 1.5 eV and the indirect optical absorption edge is approximately 1.3 eV [4]. Although there have been a few reports on the optical properties of bulk $BaSi_2$, these samples were not single crystalline but rather polycrystalline $BaSi_2$ [55, 56]. However, there is no report about the energy band gap measurement of impurity-doped $BaSi_2$. In order to ensure both high quality B-doped *p*-$BaSi_2$ epitaxial films and transparency of the substrate at the same time, we used a transparent silicon-on-insulator (SOI) substrate with (111)-oriented Si layers with submicron thickness.

5.2.1 Experimental Procedures

SOI substrates were fabricated by using wafer bonding at RT as well as chemical mechanical polishing (CMP) process. During processing, first, 500-μm-thick high-resistive Si(111) ($\rho > 1000$ Ω-cm) and 500-μm-thick fused silica wafers were bonded at RT. Then, the Si wafer was mechanically ground and polished by CMP down to about 0.7 μm approximate thickness. Oxide layers on the surface of the SOI substrate were etched away by diluted hydrofluoric acid, just before loading the substrates into the MBE chamber and then thermal treatment was performed at 590 ºC for 20 min in ultrahigh vacuum environment to clean the hydrogen-terminated surface. A 20-nm-thick $BaSi_2$ template layer was then formed at 506 ºC using RDE, prior to the deposition of 208-nm-thick B-doped $BaSi_2$ sample-Eg by MBE, where B, Ba and Si atoms were co-deposited at 650 ºC by an electron-beam gun and a Knudsen cell, respectively.

RHEED and θ-2θ-XRD patterns were utilized to evaluate the crystalline quality of the B-doped *p*-$BaSi_2$ layers both in-plane and out of plane orientation. A JASCO U-best 570 spectrophotometer was employed to measure the transmission spectra of the samples.

5.2.2 Results and Discussion

(1×1) streaky pattern of Si(111) on SOI after thermal cleaning at 590 ºC, were confirmed, as shown in Fig. 51(a). Figure 51(b) shows spot and streaky RHEED patterns after RDE-growth of $BaSi_2$ template layer along Si[11-2] azimuth. After MBE growth of B-doped $BaSi_2$, the incident electron beam was set along Si[1-10], shown in Fig. 52(a) and along Si[11-2] directions, as shown in Fig. 52(b).

Fig. 51(a) 1×1 RHEED pattern after thermal cleaning of Si on SOI at 590 ºC, observed along <11-2> azimuth and (b) RHEED pattern after RDE growth along Si[11-2] azimuth.

B-doped $BaSi_2$ epitaxial growth on the Si layer of the SOI substrates was successfully accomplished after the RDE growth, as shown in Figs. 52(a) and 52(b). Since all these RHEED patterns results before and after MBE growth determined that the B-doped *p*-$BaSi_2$ thin film was successfully grown on Si layer of the SOI substrate.

Fig. 52(a) RHEED patterns after MBE growth along Si[11-2] and (b) along Si[1-10] azimuth.

Figure 53 shows the θ-2θ XRD patterns of the B-doped $BaSi_2$ films grown on the SOI and Si(111) substrates, respectively. The diffraction peaks originated from (100)-oriented $BaSi_2$ planes, such as (200), (400), (600) planes are dominant. For the B-doped *p*-$BaSi_2$ epitaxial film on the SOI substrate, the peak intensities of these planes were almost the same as those in the $BaSi_2$ epitaxial film on the Si(111) substrate. These results indicate that the crystalline quality of the B-doped *p*-$BaSi_2$ film on the SOI substrate was equivalent to that on the single-crystalline Si(111) substrate. The transmission spectrum for the B-doped *p*-$BaSi_2$/SOI structure is given in Fig. 54(a). It is can be thought that this spectrum was significantly influenced by an interference effect within the 0.7-μm-thick Si layers. The Si layers were very thin and flat due to the CMP process, so that these interference fringes were superimposed on the spectrum. To derive interference-free transmission spectrum, the well know equation given in [57], were used:

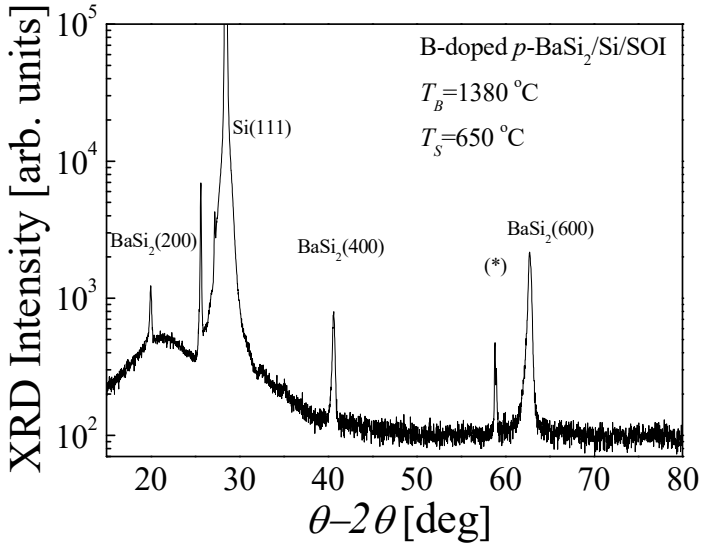

Fig.53 θ-2θ XRD patterns for the B-doped $BaSi_2$ epitaxial film grown on Si layer of the SOI substrates, at T_B= 1380 °C and T_S= 650 °C.

As shown in Fig. 54(a), the transmission spectrum was fitted by the maximal extremes of the interference fringes (T_M) and also by their minimal extremes (T_m). The interference-free transmission spectrum T_α, including the absorption in the Si layer can be calculated by taking geometric mean of T_M and T_m using Eq.(10) as:

$$T_\alpha = \sqrt{T_M T_m} \tag{10}$$

Equation 10 can employed over the entire region of the transmission spectrum [57].

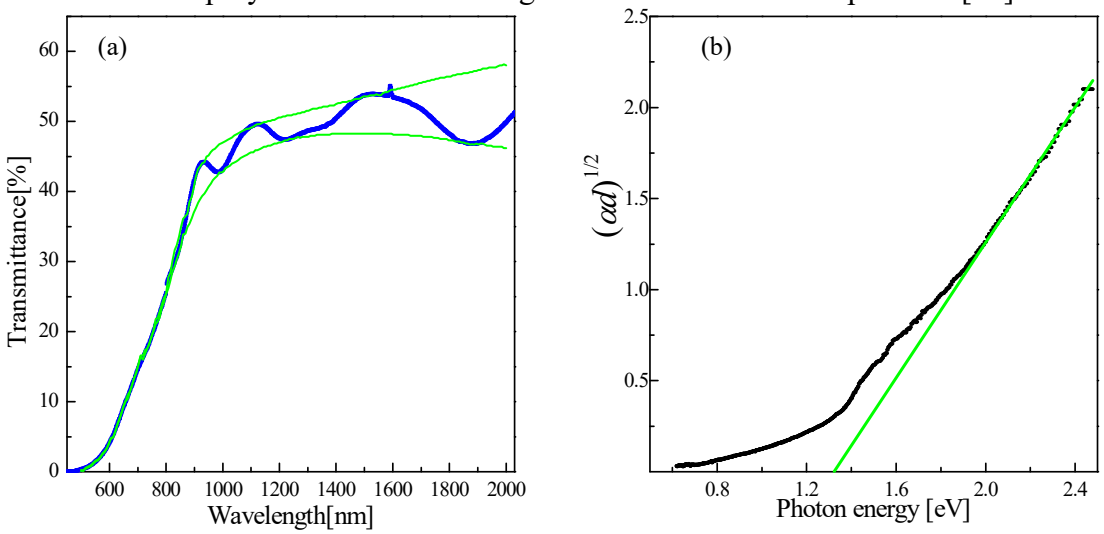

Fig. 54(a) transmittance versus wavelength, and (b) gives $(\alpha d)^{1/2}$ versus hv plot for deriving the indirect optical absorption edge.

Figure 54(b) shows the $(\alpha d)^{1/2}$ versus (hv) plot for deriving the indirect optical absorption edge. The transmission spectrum was fitted by the maximal extremes of the interference fringes (T_M) and also by their minimal extremes (Tm) as shown in Fig. 54(a). Assuming that the Si layers have a certain absorption coefficient on a transparent substrate, the interference-free transmission spectrum T_α can be expressed as just the geometric mean of T_M and Tm using Eq.10, over the entire region of the transmission spectrum [14]. The T_α values were calculated by using the T_M and T_m curves, and sing T_α, we could obtain the absorption spectrum. The straight line fitting intersects the horizontal axis at 1.23 eV. Thus, the indirect absorption edge with phonon emission was about 1.23 eV. It is found that the absorption edge decreases by approximately 0.1 eV in heavily B-doped $BaSi_2$ compared to undoped $BaSi_2$. Thus, it shows that the B-doped $BaSi_2$ does not influence the shrinkage of energy band gap for solar cell application.

5.3 MBE Growth of B-doped *p*-$BaSi_2$ on Si with New Growth Condition

In chapter 3, the TEM observation shows the presence of precipitation of B-atoms and it was not fully activated in the $BaSi_2$. First an effort was made to get the desire amount of B-atoms as well as hole concentration as a function Knudsen cell temperature. In this case it was found that RTA can enhance the hole concentrations but could not reduce strongly the precipitation of B-clusters. These precipitated B-atoms could possibly degrade the electrical properties of the thin film solar cell. Therefore it was seriously realized to overcome the B-precipitation and find solid solubility limit of B in $BaSi_2$. Fully activated B-atoms in $BaSi_2$ could give most reliable energy band gap, acceptor energy level and hole concentration for solar cell application. It is possible to reduce the defects levels in the forbidden band gap of $BaSi_2$.

It was therefore realized that there could be certain limit of Knudsen cell temperature as

well as substrate temperature in MBE growth, where, we can enhance the career concentration without compromising on crystalline quality, precipitation of B-cluster and diffusion tendency in B-doped $BaSi_2$. That novel p^+-layer of $BaSi_2$ having highest hole concentration, good crystalline quality, low diffusion tendency and low B-precipitation could bless us with profound enhancement in solar cell's efficiency.

The influence of both, growth temperature optimization as well as RTA treatment for B activation, precipitation and B-solubility limit determination will be discussed. At the end the most optimized growth condition and hole enhancement along with activation ratio will were discussed. At last but not the least, a novel p-n junction of $BaSi_2$ thin film solar cell will be attempted.

5.3.1 Experimental Procedures

Details of the growth procedure for impurity-doped $BaSi_2$ films have been previously described for In, Sb, Al, Cu and Ag-doped $BaSi_2$ [4,18,20,39,40]. For electrical measurements, high-resistivity FZ-*n*-Si(111) (ρ>1000 Ω·cm) substrates, having thickness about 380 μm were used. Substrates prior to each experiment were washed by the same standard procedure as given in Sec.2.1 for Ag-doped $BaSi_2$. Briefly, MBE growth of B-doped $p(p^+)$-$BaSi_2$ films was carried out as follows. Firstly, a 10-nm-thick $BaSi_2$ epitaxial film was grown on Si(111) at 505 °C by RDE, and this was used as a template for the $BaSi_2$ overlayers. Next, Ba, Si, and B were co-evaporated at 650 °C onto the $BaSi_2$ template to form impurity-doped $BaSi_2$. The temperature of B, T_B, was varied from 1350 to1380 °C in samples-X and-Y. The thickness of the grown layers including the template was approximately 210 nm. Rapid thermal annealing (RTA) was also performed at 800 °C for 0.5 min, 1 min and 2 min in an Ar atmosphere (samples-X and-Y). We also focused on the detailed crystalline structure as well as B-precipitation peaks of B-doped $BaSi_2$ by using, RHEED and XRD. In XRD both in-plane and out of plane surface were observed.

Hole concentration and resistivity of B-doped *p*-$BaSi_2$ epilayers were obtained from conductivity and Hall measurements using the van der Pauw configuration [59]. Hall measurements were performed under a magnetic field of 0.7 T, normal to the sample surface. Samples for Hall measurements have a minimum epilayer thickness of 210 nm. To determine the most reliable and optimize Acceptor energy level, the low temperature Hall measurement were accomplished in the temperature range [50-300 K].

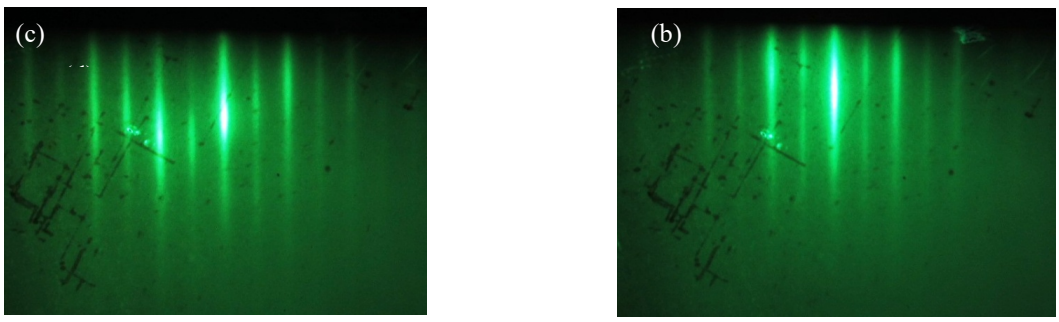

Fig. 55 a RHEED patterns of B-doped $BaSi_2$ samples grown at *Ts*= 650 °C when T_B is (a), 1350°C (sample-X) and (b) 1380°C (sample-Y), observed along the Si[11-2] azimuth.

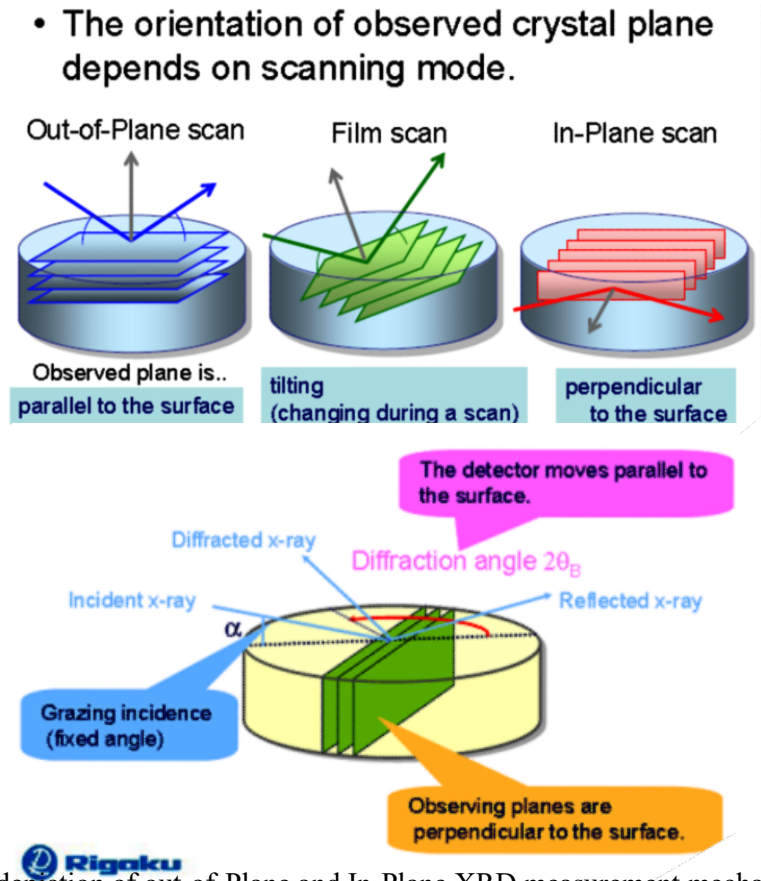

Fig. 56 depiction of out-of-Plane and In-Plane XRD measurement mechanisms.

Figure 56, gives the conceptual idea of out-of-Plane and in-Plane XRD measurement mechanism.

5.3.2 RESULTS AND DISCUSSION

5.3.2.1 *Crystallinity by RHEED and XRD*

Figures 55(a)-(b) show streaky RHEED patterns, observed along the Si[11-2] azimuth of B-doped as-grown $BaSi_2$ films prepared at T_B=1350-1380 °C, T_S=600 °C, which indicates that the

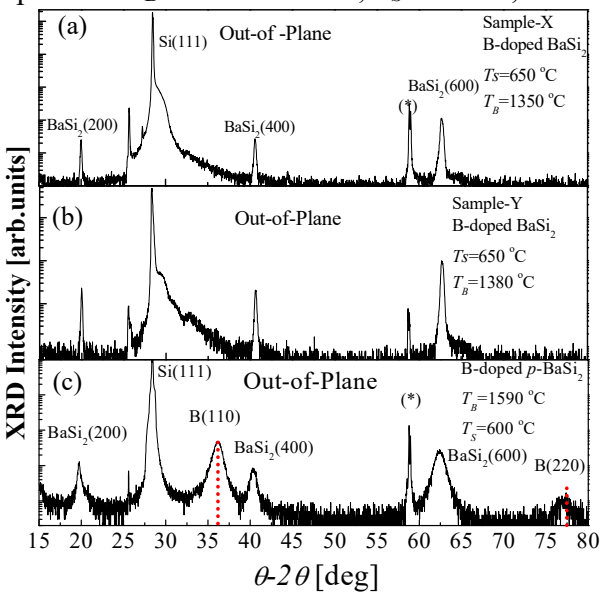

Fig. 57 gives θ-2θ XRD out-of-Plane patterns of B-doped $BaSi_2$ films grown at (a), T_S=650°C T_B=1350 °C (Sample-X), (b), T_S=650°C T_B=1380 °C (Sample-Y) and (c) heavily B-doped at T_S=600°C T_B=1590 °C (heavily B-precipitated reference sample).

the epitaxial growth of B-doped $BaSi_2$ films were grown successfully. In both sample epitaxial growth by MBE were achieved.

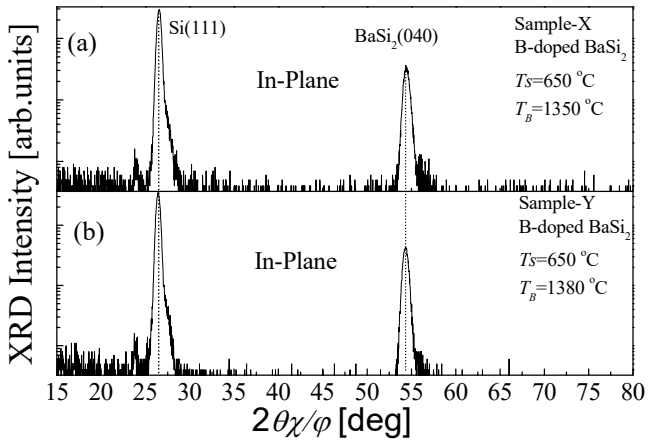

Fig. 58 gives $2\theta\boldsymbol{\chi}/\boldsymbol{\varphi}$-XRD In-Plane patterns of B-doped $BaSi_2$ films grown at (a), T_S=650°C T_B=1350 °C, (Sample-X), and (b), T_S=650°C T_B=1380 °C (Sample-Y).

Figures 57(a)-(b) show the θ-2θ XRD Out-Of-Plane patterns of B-doped as-grown $BaSi_2$ films at T_S=650°C. T_B=1350-1380 °C, where diffraction peaks of (100)-oriented $BaSi_2$, such as (200), (400) and (600), are dominant, which confirmed the epitaxial relationships between $BaSi_2$ and Si, without any extra peaks originated from B-nano clusters (precipitation). Out-Of-plane XRD measurement shows no precipitated B-peaks in Sample-X and-Y respectively.

But in contrast Fig. 57(c) shows the θ-2θ out-of-Plane XRD patterns of heavily B-doped as-grown $BaSi_2$ films with T_S=600°C. T_B=1590 °C, where two new diffraction peaks of rhombohedral B(110) around 2θ=36° and B(220) at 2θ=77°, were appeared in addition to (100)-oriented $BaSi_2$, such as (200), (400) and (600) . This means that the crystalline quality starts to deteriorate with increasing B- atomic concentrations beyond T_B=1400 °C, even with T_S=600°C. This confirmed that the out-of-plane XRD for sample-X and sample-Y has no B-nano clusters (B-precipitation free).

We were not sure about the existence of extra peaks originated from B-cluster in the in-Plane XRD measurement. It can be believed that the in-Plane XRD measurement is very sensitive for any unusual peaks. Therefore, we conducted in-Plane XRD-measurement of sample-X and sample-Y to confirm and verify the precipitation exclusion in these two novel samples.

Figures 58(a)-(b) give $2\theta\boldsymbol{\chi}/\boldsymbol{\varphi}$-XRD In-Plane patterns of B-doped $BaSi_2$ films grown at (a), T_S=650°C T_B=1350 °C, (Sample-X), and (b) T_S=650°C T_B=1380 °C, (Sample-Y), respectively.
In both sample, diffraction peaks of Si (111) and $BaSi_2$ (040) are dominant, which confirmed the exclusion of any extra peaks originated from B-nano clusters (precipitation). This new peak of $BaSi_2$ (040) was observed for the first time in the in-plane XRD measurement. On the basis of these results, it can be concluded that the precipitation free epitaxial growth of B-doped $BaSi_2$ with the new growth condition T_S=650°C T_B=1350-1380 °C were successfully achieved for the p^+-layer of $BaSi_2$ thin film solar cell. In the next section electrical characterization at RT as well as at low

temperature dependence of Sample-X will be presented.

5.3.2.2 Electrical Properties by Hall measurement

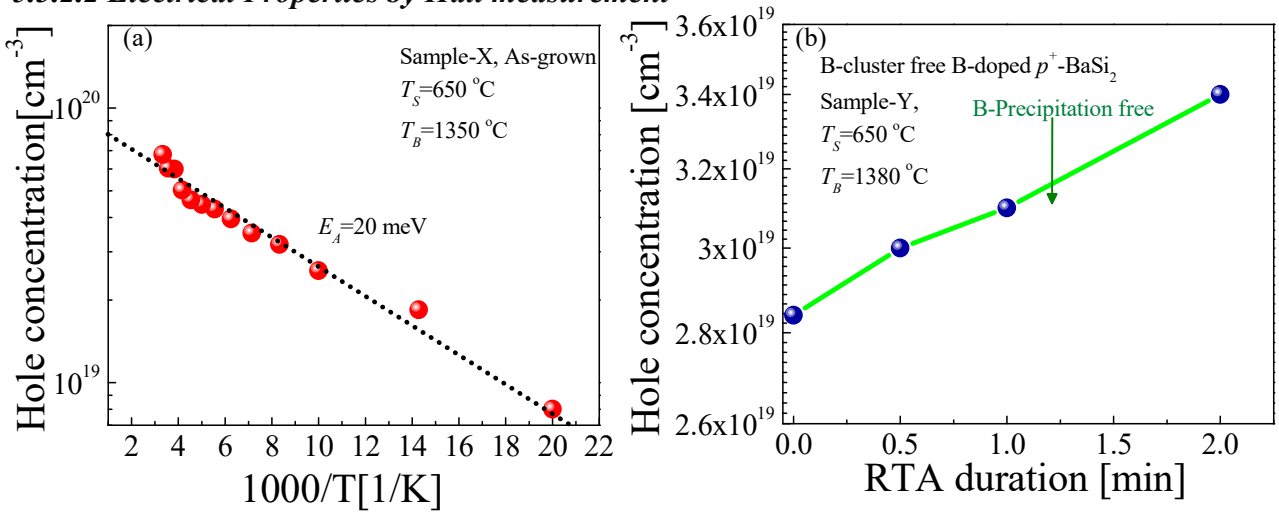

Fig. 59(a) hole concentration Vs temperature for B-doped *p*-$BaSi_2$ as-grown sample grown at T_B=1350 °C (sample-X), and (b) gives dependence of hole concentration on t_{RTA} for sample-Y.

B-doped as-grown $BaSi_2$ showed *p*-type conductivity for sample-X by using Hall measurement at RT. Figure 59(a) shows temperature dependence of hole concentrations in as-grown sample-X. The hole concentration reached 8×10^{19} cm^{-3} at RT, and then decreased to 7×10^{18} cm^{-3} with decreasing temperatures until 50 K. The acceptor level, E_A, was calculated to be 20 meV using Eq. (11).

$$p \propto \exp(-\frac{E_A}{2k_BT}) \qquad (11)$$

In equation 11, k_B is the Boltzmann's constant, and T the absolute temperature. This E_A value is almost the same as-grown B-precipitated sample, grown at T_S=600°C T_B=1550 °C, as discussed in Chapter-3. The precipitated grown sample gives acceptor level of 23 meV. This $E_{A=}$ 20 meV for the as-grown sample-X could be more reliable acceptor level in the *p-n* junction. The activation efficiency of B atoms in sample-X can thus be estimated, that is, $p/N_B = 8\times10^{19}/2\times10^{20} \cong 40\%$.

Figure 59(b) gives hole concentration enhancement from 2.8×10^{19} to 3.4×10^{19} cm^{-3} after 0.5, 1 and 2 min RTA time for sample-Y. This value is the highest ever achieved for p^+-$BaSi_2$, having no B-precipitation shown by XRD and indicating that higher T_S value as well as RTA treatment improved the electrical activation efficiency of B-atoms in $BaSi_2$. It is worthwhile to mention further that the B-atoms may be substituted into Si atomic site instead of Ba-atomic site or interstitial site in $BaSi_2$. Energetically there is some analogy between B- and In-atomic behaviors in the $BaSi_2$. In the next section electrical characterization of novel *p-n* junction will be presented first.

5.4 MBE Growth of *p-n* junction of $BaSi_2$ Thin Film Solar Cell

After finding solubility limit of B-atoms in $BaSi_2$ by using new growth condition, we grow *p-n* junction structure first to check the diffusion and segregation phenomenon and then to grow *p-n* structure for efficiency measurement in the near future. In the next section detail about the experimental procedures are given.

5.4.1 Experimental Procedures

For SIMS measurements, low-resistivity CZ-*n*-Si(111) ($\rho \leq 0.005\ \Omega\cdot cm$) substrates were used. Substrates prior to each experiment were washed by the same standard procedure as given in Sec.2.1 for Ag-doped $BaSi_2$. Briefly, MBE growth of B-doped *p-n* junction of $BaSi_2$ films was carried out as follows. Firstly, a 10-nm-thick $BaSi_2$ epitaxial film was grown on Si(111) at 500 °C by RDE, and this was used as a template for the undoped $BaSi_2$ overlayers. Next, Ba, and Si, were co-evaporated at 580 °C onto the $BaSi_2$ template to form undoped $BaSi_2$ absorption layer. Lastly Ba, Si, and B were co-evaporated at 580 °C onto the $BaSi_2$ template to form B-doped $BaSi_2$ (60nm)/un-doped $BaSi_2$ (280nm)/Si(111) structure. The temperature of B, T_B, was kept at 1350 °C in samples Z. The thickness of the grown layers including the template was approximately 350 nm. The crystalline structure of sample Z were investigated by using, RHEED and XRD.

The diffusion and segregation tendency were characterized by SIMS measurement.

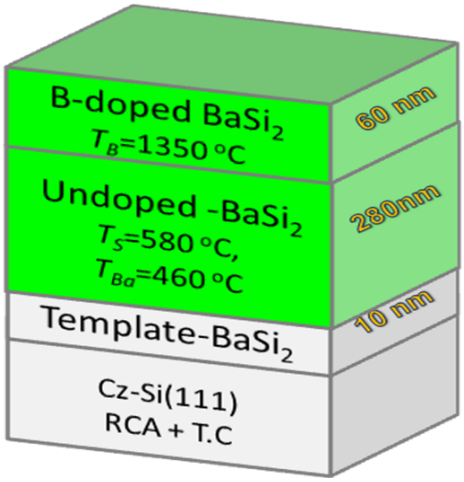

Fig. 60 *p-n* structure B-doped $BaSi_2$ (60nm)/un-doped $BaSi_2$ (280nm)/Si(111).

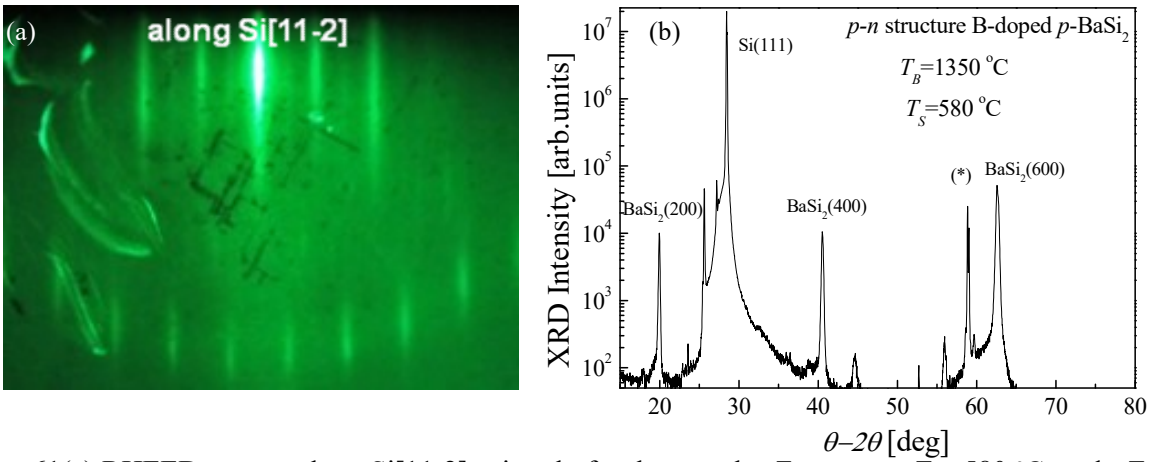

Fig. 61(a) RHEED pattern along Si[11-2] azimuth, for the samples Z grown at T_S= 580 °C, and , T_B= 600 °C and (b) gives XRD pattern after MBE growth.

5.4.2 RESULTS AND DISCUSSION

Figure 60 gives the overall *p-n* structure based on B-doped $BaSi_2$ thin film. Figure 61(a), shows the RHEED patterns after MBE growth of sample Z along Si[11-2] azimuth and streaky pattern were observed, which indicates that samples with *a*-axis oriented $BaSi_2$ were successfully grown.

Figure 61(b) shows the dominant diffraction peaks of *a*-axis oriented-Si $BaSi_2$ (200), (400), and (600) of B-doped $BaSi_2$ on un-doped $BaSi_2$/ Si in the as grown sample Z.

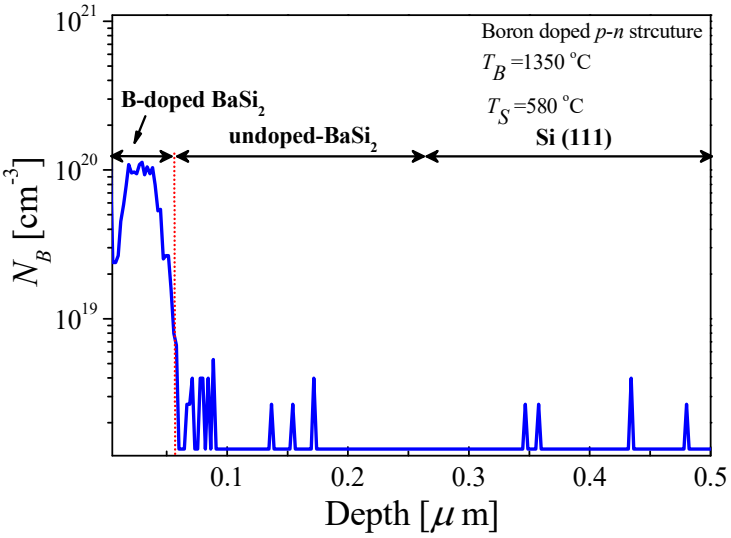

Fig. 62 SIMS depth profiles of B-doped $BaSi_2$ (60nm)/un-doped $BaSi_2$ (280nm)/Si(111) structure.

SIMS measurements revealed that the doped B atoms are almost uniformly distributed within the $BaSi_2$ layers and no segregation was found toward the un-doped $BaSi_2$ as shown in Fig. 62. The average B-atomic concentration (N_B) was found to be approximately 4×10^{19} cm^{-3}. The relationship between B atoms could be confirmed from the Hall measurement data Fig. 46(a). In this case very sharp edges were obtained at the hetro-interface and no diffusion tendency toward the un-doped $BaSi_2$/Si was found. It shows that the diffusion coefficient of B-doped $BaSi_2$ might be small and the *p*-layer could be qualified for the *p-n* junction of solar cells. The future *p-n* junction of $BaSi_2$ thin film solar cell will be attempted and theoretical models about the front and back side illumination of the cell is given in Apindix-A. The diffusion coefficient of B-doped $BaSi_2$ is small and could possibly give small segregation tendency in $BaSi_2$ [61]. In the next section ionization energies of donor and acceptors impurity levels in $BaSi_2$ will be presented.

5.5 IONIZATION ENERGY CHART OF IMPURITY DOPED $BaSi_2$ THIN FILMS

The good quality of *p-n* junction of solar cell that require abrupt doping profiles, an additional requirement is a small diffusion rate of the dopant, which minimizes profile smearing during subsequent thermal processing steps and electrical properties. It is important to study and understand the impurity doping influence on activation level or incorporation mechanism in $BaSi_2$. The chart of the potential donors and acceptors levels of impurity (In, Sb, Al, Cu, Ag, P and B) in $BaSi_2$ is summarized in Fig. 63. Based on the electrical properties and precipitation the B-doped $BaSi_2$ and Sb-doped $BaSi_2$ gives shallow levels. For the above reasons, Sb has become the best

choice for heavy *n*-type doping of $BaSi_2$ and B has become the best choice for heavy *p*-type doping of $BaSi_2$.

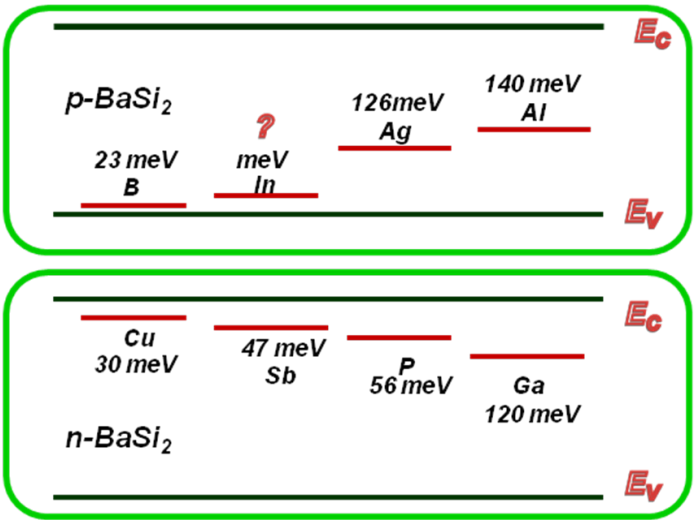

Fig. 63 Ionization energy values chart for various dopants in $BaSi_2$.

CHAPTER 6: SUMMARY AND FUTURE WORK

The demand for low cost, eco-friendly and high efficiency energy resources imposes strict requirements on the choice of material selection. The impurity incorporation into the *p-n* junction as well as TJ of $BaSi_2$ epitaxial layers without compromising the crystalline quality, precipitation of impurity atoms (nano-cluster) and diffusion tendency as well as maintaining good electrical properties of such materials are important issues for new generation thin film solar cells. Novel p^+-layer of $BaSi_2$ having highest hole concentration, good crystalline quality, low diffusion tendency and low B-precipitation could bless us with profound enhancement in solar cell efficiency. This dissertation has contributed to the understanding of all these issues one by one. This chapter focuses on the major contributions of this research work and also to discuss future avenues and challenges. Some un-addressed research problems will be considered in this chapter.

6.1 PAST RESEARCH WORK

Many semiconductor technologies and photovoltaic devices rely on the ability to fabricate two different types of electrically conducting layers: *n*-type and *p*-type. An electrically active dopant atom provides a free carrier to the conduction or valence band by creating an energy level that is very close to one of the bands (shallow levels). In other words good quality *p-n* junction diodes can be formed by impurity doping, where the electric field around the *p-n* junction can separate the photo-excited electron-hole pairs for photovoltaic power generation. An ideal dopant should therefore have a shallow donor/acceptor level and high solid solubility limit as well as minimum precipitation of impurity atoms. Control and optimization of carrier concentration is essential for any semiconductor devices. Some devices require moderate level of doped layers and some required heavily doped layers, which depends on the nature of device application and structure. For example in case of $BaSi_2$ solar cell structure, heavily doped p^+-layer is needed for both TJ and top layer of solar cells to form ohmic contact.

Some investigations were conducted to study both theoretically and experimentally the epitaxial growth, crystalline quality and detail of electrical characterization by using 13-15th group impurity candidates like Sb, Ga, In and Al into $BaSi_2$. Surface segregation and diffusion are two major problems that have been encountered during dopant incorporation in $BaSi_2$ epitaxy. Crystallization of impurity atoms in the $BaSi_2$ crystal were studied extensively. Special focus was given to the impurity atoms crystallization sites. During the MBE growth both Knudsen cell temperature and substrate temperature were used to control atomic concentrations and carrier concentrations along with crystalline investigation. The mechanism for impurity diffusion was investigated in the absence of other interfering factors, such as precipitation, solid solubility limit and dangling bond defects. Some thermodynamic problems, which in turn creates cracks in the grown samples of $BaSi_2$ having thickness more than 250 nm during MBE growth as well as after RTA treatment could be possibly due to strain and stress relaxation phenomena. The understandings of root causes of this issue are very important for the fabrication of $BaSi_2$ films.

Electron concentration in Ga doped *n*-$BaSi_2$ could not be controlled and it behaves contrary to the theoretical conductivity, which is *p*-type. The actual status of Ga-doping into the $BaSi_2$ is still unresolved research issue for the both experimental as well as theoretical physicists. The other impurity candidates like In, Al and Sb in $BaSi_2$ thin films give a similar type of conductivity after theoretical and experimental investigation.

MBE (*In-situ)* epitaxial growths of Sb-doped $BaSi_2$ were successfully accomplished. The electron concentration was controlled in the range from 10^{16} and 10^{20} cm^{-3} in Sb-doped *n(n$^+$)*-type $BaSi_2$, thin films. Sb-atoms show low diffusion tendency in $BaSi_2$ both toward the Si substrate as well as toward the undoped *n*-$BaSi_2$ layer, after introducing delta-layer by SPE. Sb-doped $BaSi_2$ activation energy level measurements were not attempted and the ohmic contact at low temperature was not resolved. The measurement of NDR effect across the TJ was not successful due to the existence of some defects level in the band gap of Sb-doped *p-n* structure. The determination of solid solubility limit of Sb-atoms in $BaSi_2$ is still an open research problem.

MBE (*In-situ)* epitaxial growths of In, and Al-doped $BaSi_2$ were also successfully accomplished, where hole concentration were limited to $10^{17}cm^{-3}$. Al-doped $BaSi_2$ showed a severe diffusion tendency toward the Si substrate. It is necessary to have heavy hole concentration, shallow energy levels and low diffusion tendency for *p-n* junction application. This was extensively investigated to see the influence of both growth temperature as well as Knudsen cell temperature variation on the impurity atomic incorporation in the crystallized $BaSi_2$. This means that the important *n*(*n*$^+$) aspect of the $BaSi_2$ *p-n* junction was successfully achieved but the remaining *p(p$^+$)* aspect yet to be achieved.

Therefore an effort was made in this dissertation to find more suitable impurity doping candidates for the formation *p*$^+$-layer for the *TJ* as well as for the top layer of $BaSi_2$ solar cells.

6.2 THIS RESEARCH WORK

6.2.1 SILVER (Ag) , COPPER (Cu) AND ANTIMONY (Sb) - DOPED $BaSi_2$

During the impurity doping in the MBE growth, Cu and Ag were used as potential impurity candidates and aimed to form *p* & *p*$^+$-$BaSi_2$ thin film layers for different regions of *p-n* junctions of the efficient solar cell structure. *a*-axis-oriented Ag and Cu-doped *p*(*n*)-type $BaSi_2$ films were grown successfully on Si(111) by MBE technique, where SIMS shows no diffusion of Cu atoms toward the Si(111) substrate or the un-doped region in case of Cu-doped $BaSi_2$. However, in case of Ag-doped $BaSi_2$ diffusion tendency was found. A comparative study of Al and Cu as dopants to make *p*-type $BaSi_2$ layers was carried out at first place. It was found from the SIMS measurements that Al atoms doped in $BaSi_2$ layers were segregated at both the surface and $BaSi_2$/Si interface regions. On the other hand, a clear cut depth profile of Cu atoms and heavily *n*-type doping was realized for Cu-doped $BaSi_2$. Yet, the electron concentration in Cu-doped $BaSi_2$ remained unchanged, even when the Cu temperature was increased to 950 ^oC. Instead, the electron concentration increased sharply up to more than 10^{20} cm^{-3} at around 1000 ^oC. These results suggest that control of electron

concentrations in Cu-doped $BaSi_2$ is difficult. In contrast, Ag-doped $BaSi_2$ show *p*-type conductivity, but the hole concentration was limited to 10^{16} cm^{-3}. From the temperature dependence Hall measurements, acceptor and donor energy level of Ag, and Cu-doped $BaSi_2$ were found to be E_A=0.12 eV, E_D=0.035 eV respectively.

The temperature dependent Hall measurement of Sb-doped $BaSi_2$ gives an electron density of about 3.3×10^{18} cm^{-3} at 300K, which then decreases with decreasing temperature to 2.8×10^{17} cm^{-3} at 27 K. The approximate donor level E_D=47 meV was achived for the first time. In this experiment it was found that the resistivity increases gradually with temperature. This behavior was further supported by temperatures dependent I-V characterization where the I-V characteristic maintains ohmic behavior, over the wide range of temperature from 27K to 300K. This change in I-V characterization can be explained by the change in resistivity of Sb-doped $BaSi_2$ accordingly. This means that the contact resistance is smaller than the bulk resistance in this temperature range, thereby showing that good electrical contacts are formed on the surface.

Temperature dependent I-V characterization across the TJ yields small NDR effect, which further shows that a small amount of tunneling current is flowing across the TJ.

6.2.2 CONDUCTION MECHANISMS

To quantify the defect levels in the impurity doped-$BaSi_2$, the carrier transport mechanism is reported in this dissertation. Many temperature dependent experiments were conducted for each impurity doped $BaSi_2$. The temperature dependence of resistivity indicated that the carrier transport in Ga, Al, Ag, and Cu-doped $BaSi_2$ can be well explained by both SE-and Mott-type VRH conduction. This further means that there is certain level of defects in the band gap of Ga, Al, Ag and Cu-doped $BaSi_2$.

In contrast, temperature dependent resistivity in Sb, In and B-doped $BaSi_2$ gives a non-linear behavior, which confirms that the carrier transport cannot be explained by SE-& Mott-type VRH hopping conduction mechanism. This further means that a very small level of defects in the band gap of Sb, In and B-doped $BaSi_2$ could exist. However after precipitation studies as well as solid solubility limit of impurity doped $BaSi_2$, one can get more credible information about the conduction mechanism of this novel material.

6.2.3 BORON (B) - DOPED $BaSi_2$

In conclusion, we have successfully grown *a*-axis-oriented lightly, medium and heavily B-doped *p(p^+)*-type $BaSi_2$ films on Si(111) by MBE. SIMS measurement shows that the average N_B for $BaSi_2$ prepared with T_B=1350 °C is approximately 3×10^{20} cm^{-3}, while that with T_B=1450 °C is 2×10^{21} cm^{-3} and T_B=1550 °C is approximately 1×10^{22} cm^{-3}. This result can explained relatively well by the difference in vapor pressure of B. The vapor pressure of B at 1550 °C is approximately 7 times larger than that at 1450 °C. This means that the concentration of B atoms in the $BaSi_2$ can be controlled by T_B.

We have also successfully achieved heavy *p*-type doping over 10^{20} cm^{-3} in B-doped $BaSi_2$ by MBE growth. The acceptor level was estimated to be approximately 23 meV. The RTA treatment at 800 °C enhanced the electrical activation of doped B atoms, thereby increasing the hole concentrations up to 2.0×10^{20} cm^{-3}. But, B-doped $BaSi_2$ epilayers grown at low growth temperature, exhibit partial deactivation of B-atoms in the host *p*-layer of $BaSi_2$. The electrical properties are also degraded, indicating the presence of B-clusters and precipitation. RTA annealing recovers the hole electrical properties as well as improving grain island.

The hole concentration in the range from 10^{16} to $2\times10^{20}cm^{-3}$ with increasing T_B and varying T_S was controlled for the first time after RTA treatment. The B-clusters having sizes within the range of 3-5 nm were observed in the TEM image. It was also found from the TEM results that the precipitated B-cluster size increases with Knudsen cell temperature. The grain size in the $BaSi_2$ films was found to be approximately 0.5 μm, which is the highest value ever reported for doped-$BaSi_2$. From TEM, SIMS and RTA treatment electrically active Boron atomic concentrations upto 10 % in the B-doped p^+-$BaSi_2$ were calculated. The B-precipitation and B-solid solubility limit were unclear problems.

6.2.3 Optimized B-DOPED p^+- layer of $BaSi_2$ by New Growth Technique

TEM observation shows precipitation of B-atoms and which were not fully activated in the $BaSi_2$. First an effort was made to get the desire amount of B-atoms as well as hole concentration as a function Knudsen cell temperature. In this case it was found that RTA can enhance the hole concentrations up to $2\times10^{20}cm^{-3}$ but could not well reduce the precipitation of B-clusters. These precipitated B-atoms could possibly degrade the electrical properties and photocurrent performances of the semiconducting $BaSi_2$ thin film solar cell. Therefore it was greatly necessary to overcome the B-precipitation and find the solid solubility limit of B in $BaSi_2$. Fully activated B-atoms in $BaSi_2$ could potentially give the most reliable energy band gap, acceptor energy level and hole concentration for solar cell application. It is also possible to reduce the defect levels in the forbidden band gap of $BaSi_2$. Therefore, we tested many samples through substrate temperature optimization like 650 °C in the MBE, keeping Knudsen cell temperature between 1350 to 1380 °C we found new growth conditions, which has B-free precipitation in the grown samples. By using these new growth conditions, approximately 208-nm-thick B-doped *p*-$BaSi_2$ epitaxial layers were first grown by RDE and MBE on transparent SOI substrates. RHEED and θ-2θ-XRD patterns exhibited epitaxial growth of the B-doped *p*-$BaSi_2$ on the SOI substrate for the first time in measuring the energy band gap of the B-doped $BaSi_2$. In conclusion, we have successfully achieved heavily *p*-type doping over 10^{19} cm^{-3} in B-doped $BaSi_2$ by MBE, having no B-precipitation and segregation issues. The acceptor level was estimated to be approximately 20 meV. The RTA treatment at 800 °C enhanced the electrical activation of doped B atoms, thereby increasing the hole concentrations up to 3.4×10^{19} cm^{-3}. It was found from the transmission spectrum that the indirect optical band edge with phonon emission of approximately 1.23 eV, and it's giving 0.1 eV shrinkage of energy band gap of B-doped $BaSi_2$. This means that B-doped $BaSi_2$ does influence lightly to the shrinkage of band gap for solar cell application**.**

We have also successfully grown *a*-axis-oriented *p*-type $BaSi_2$ films on Si(111) by *in situ* B-doping using MBE. The highest hole concentration in B-doped $BaSi_2$ above 10^{19} cm^{-3} at RT were achieved in samples having no diffusion and precipitation problems. The acceptor level was estimated to be approximately 20 meV. This new growth condition defines the solid solubility limit of B in $BaSi_2$ host materials. Activation efficiency were enhanced from 10% to 40 % by optimized New growth condition of B-doped $BaSi_2$ p^+-layer having hole density $8\times10^{19}cm^{-3}$ (B-Precipitation free sample)**.** SIMS depth profiles of B-doped $BaSi_2$ (50nm)/un-doped $BaSi_2$ (300nm)/Si(111) structure does not show any diffusion tendency as well as segregation of B-atoms toward un-doped $BaSi_2$/Si.

In this dissertation, we have successfully achieved approximate ionization energy values chart for the case of impurity doped $BaSi_2$ thin film for *p-n* junction application. From this novel result, the fabrication of Sb-doped $n(n^+)$-type (10^{17}-$10^{20}cm^{-3}$) and B-doped $p(p^+)$-type (10^{16}-$10^{20}cm^{-3}$) regions of the next generation *p-n* junction in $BaSi_2$ solar cells will be attempted. The novel p^+-layer is one step behind the practical semiconducting $BaSi_2$ solar cell *p-n* junctions.

6.3 FUTURE RESEARCH WORK

The academic motivation of this of research problem is to solve the controversial behavior of Ga doped *n*-$BaSi_2$ which behaves contrary to the theoretical conductivity of p-type.

One other interesting and important problem to identify the solid solubility limit of Sb-atoms in $BaSi_2$ thin films and then grow TJ with new growth condition of Sb-doped $BaSi_2$. By this approach we can get rid of precipitation of Sb-atoms in the grown sample. Sb-cluster precipitation could possibly degrade the electrical properties as well as photocurrent flow across the *p-n* junction and TJ. This kind of study can improve the electrical properties and photoresponsivity of Sb-doped *n*- $BaSi_2$ films. This will further improve the NDR effect across the TJ. The poor tunneling current flow across the TJ could possibly be due to the precipitated Sb-clusters, which act like defects in the band gap. Band gap and valance band measurements of the Sb-doped $BaSi_2$ are necessary for the realization of $BaSi_2$ thin film solar cell engineering.

It is worthwhile to improve the *p-n* structure for single junction diode application and then to engineer multi junction $BaSi_2$ thin film solar cells for high efficiency demands. A measurement of the photoresponse properties of B-doped BaSi2 under new growth conditions is ultimately needed in the near future. The new growth condition of B-doped $BaSi_2$ could give reliable data on minority carrier life time and very low diffusion tendency.

Concept of selective reflector to overcome E_g limit for $BaSi_2$ and to enhance the band gap energy for the open circuit voltage requirements is unaddressed problem.

Regarding the undoped $BaSi_2$, the electrical characterization issue like ohmic contacts as well as difficulty in Hall measurement must be resolved. This can be most likey be solved by revisiting Ba-source temperature optimization as well as growth temperature of MBE for undoped-$BaSi_2$. The plane view from TEM investigation for both DF and BF investigation are important to focus on the nano-cluster in the $BaSi_2$. The in-plane XRD measurement gives very interesting results in case of B-doped $BaSi_2$. Furthermore, from in-Plane XRD view, we could not see the

$BaSi_2$ peaks. The thickness length of the grown-layers is also important for the engineering of efficient $BaSi_2$ solar cell structures. Optimization of the thickness of undoped $BaSi_2$ layer, B-doped $BaSi_2$ layer and Sb-doped $BaSi_2$ thin layers for the solar cell structure.

Some thermodynamic problems, which in turn creates cracks in the grown samples of $BaSi_2$ having thickness more than 250 nm during MBE growth as well as after RTA treatment could be possibly due to strain and stress relaxation phenomena. The understanding of root causes of this issue is very important for the fabrication of $BaSi_2$ thin films.

During handling of B-doped $BaSi_2$ thin film samples it can be speculated that the strength of this material may be high than the other impurity-doped $BaSi_2$ materials. We can go for the stress, strain analysis and fracture investigation of B-doped p^+-$BaSi_2$ to determine the hardness as well as other mechanical properties.

APPENDIX A

MODEL OF *p-n* JUNCTION UNDER ILUMINATION OF FRONT AND BACK SIDE

(1) Illumination on the front side of p^+-$BaSi_2$/*n*-$BaSi_2$

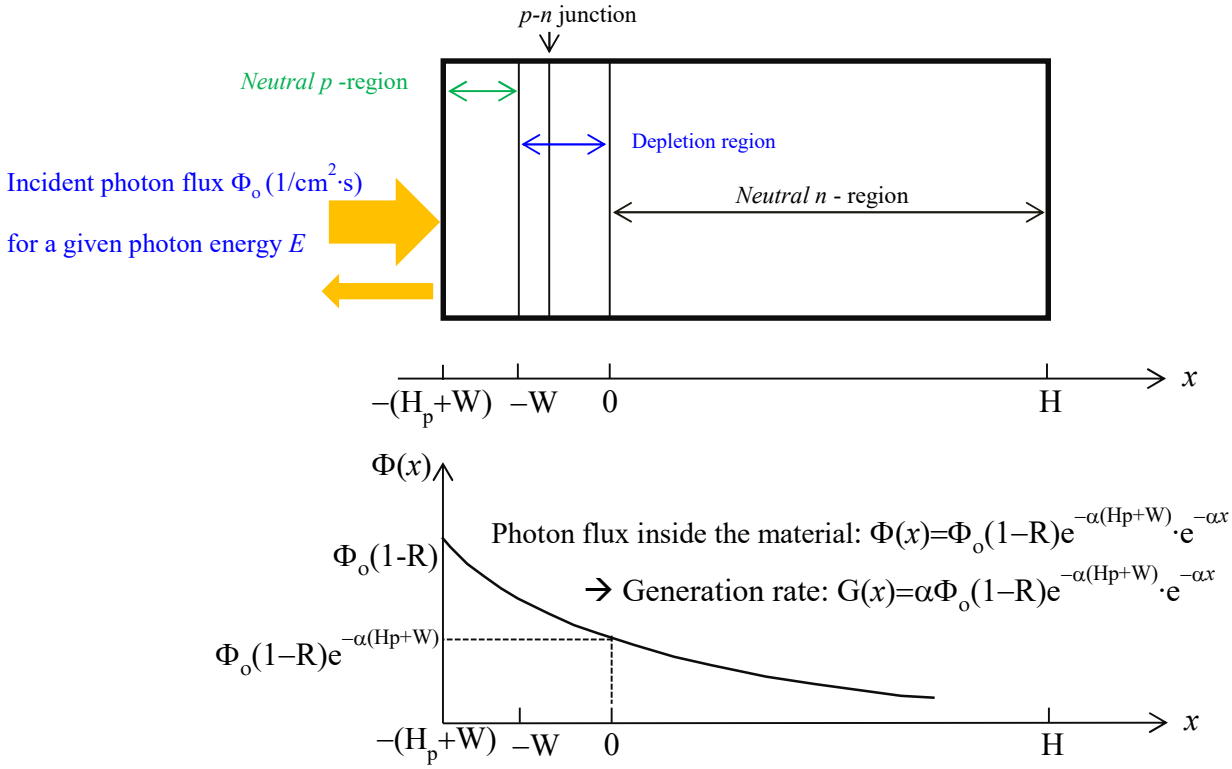

(2) Illumination on the back side of p^+-$BaSi_2$/*n*-$BaSi_2$

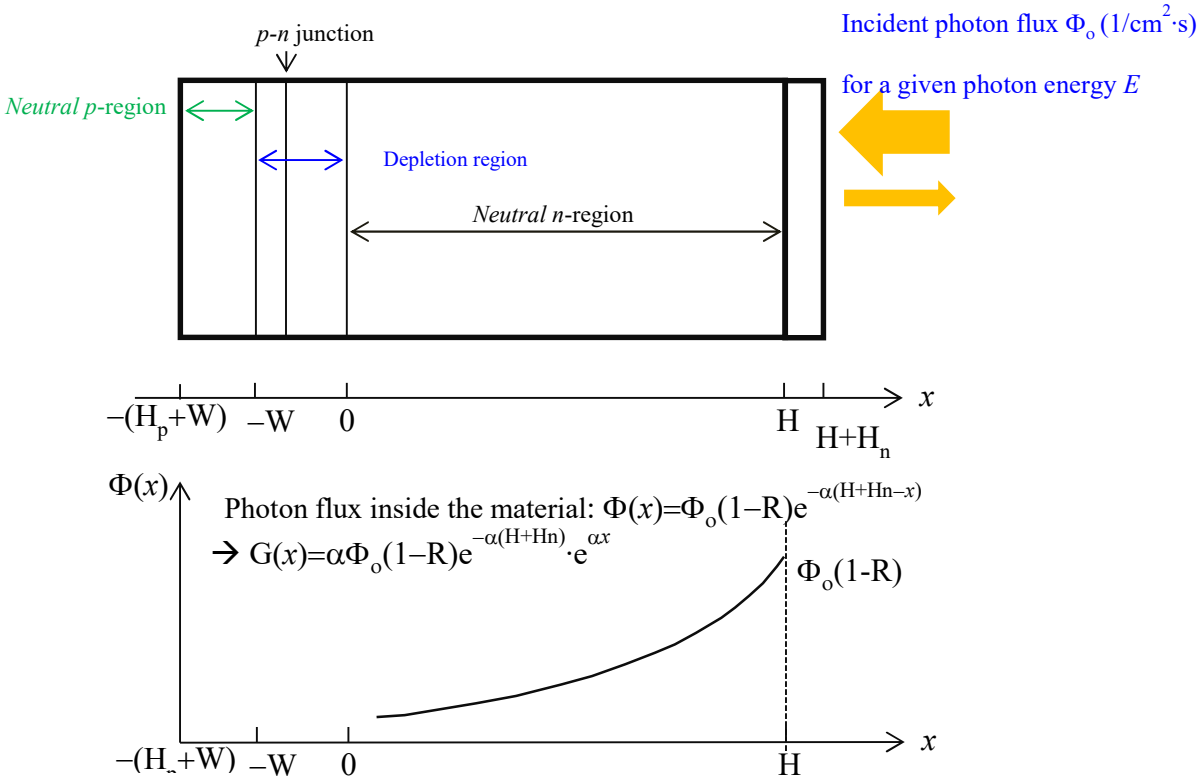

(1) Hole current due to photo-generated holes in the n-region under illumination on the front side.

We suppose that the forward voltage V is applied to the p-n junction due to the voltage drop at the load resistance. The photocurrent due to photo-generated electrons J_e in the p^+-type neutral region is negligibly small. Hence, we try to deduce only J_h.

The minority carrier (holes) distribution $p_n(x)$ in the neutral n-type region (x>0) is given by,

$$D\frac{d^2 p_n}{dx^2} + G - \frac{p_n - p_{no}}{\tau} = 0,\ G = \alpha(1-R)\Phi_o e^{-\alpha(H_p+W)} e^{-\alpha x}$$

$$\frac{d^2\Delta p_n}{dx^2} + \frac{G}{D} - \frac{\Delta p_n}{\tau D} = \frac{d^2\Delta p_n}{dx^2} + Ce^{-\alpha x} - \frac{\Delta p_n}{L^2} = 0 \qquad [1]$$

$$\text{where},\ C = \frac{\alpha(1-R)\Phi_o}{D} e^{-\alpha(H_p+W)}$$

The general solution of Eq.[1] is

$$\Delta p_n = Ae^{\frac{x}{L}} + Be^{-\frac{x}{L}} \qquad [2]$$

The particular solution of Eg.[1] is

$$\Delta p_n = De^{-\alpha x} \qquad [3]$$

From Eqs.[1] and [3],

$$D(-\alpha)^2 + C - \frac{D}{L^2} = 0、\ D = -\frac{L^2}{\alpha^2 L^2 - 1}C$$

$$p_n(x) = p_{no} + Ae^{\frac{x}{L}} + Be^{-\frac{x}{L}} - \frac{L^2}{\alpha^2 L^2 - 1}Ce^{-\alpha x} \qquad [4]$$

(i) Ideal case, that is, the following two boundary conditions should be satisfied,

$$At\ \ x = 0,\ p_n(0) = p_{no}e^{\frac{qV}{kT}} \qquad (A)$$

$$At\ \ x = H\ (>>\ L),\ \ p_n(H) = p_{no} \qquad (B)$$

As we all know, photocurrent density J_L is given by,

$$J_L = q\Phi_o(1-R)e^{-\alpha(H_p+W)}\frac{aL}{\alpha L+1}$$

(ii) More realistic case, that is, $p_n(H)$ is determined by a recombination velocity S at the back surface. This can be applied to a $BaSi_2$ *p-n* junction diode on Si as shown in the right figure.

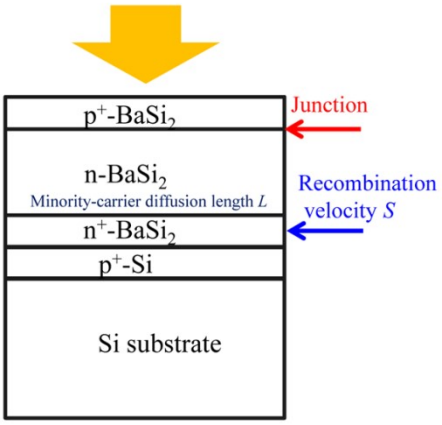

$$At\ x=0, p_{no}(0)=p_{no}e^{\frac{qV}{kT}} \qquad (A)$$

$$At\ x=H, -D\frac{dp_n}{dx}=S(p_n-p_{no}) \qquad (B)$$

From the boundary condition (A),

$$p_{no}+A+B-\frac{L^2}{\alpha^2L^2-1}C=p_{no}e^{\frac{qV}{kT}} \ 、\ A+B=p_{no}(e^{\frac{qV}{kT}}-1)+\frac{L^2}{\alpha^2L^2-1}C \qquad [5]$$

From the boundary condition (B),

$$\frac{dp_n}{dx}=\frac{1}{L}Ae^{\frac{x}{L}}-\frac{1}{L}Be^{-\frac{x}{L}}+\frac{\alpha L^2}{\alpha^2L^2-1}Ce^{-\alpha x}$$

$$S(p_n-p_{no})=S(Ae^{\frac{H}{L}}+Be^{-\frac{H}{L}}-\frac{L^2}{\alpha^2L^2-1}Ce^{-\alpha H})=-\frac{D}{L}(Ae^{\frac{H}{L}}-Be^{-\frac{H}{L}})-\frac{\alpha L^2D}{\alpha^2L^2-1}Ce^{-\alpha H}$$

$$(S+\frac{D}{L})e^{\frac{H}{L}}A+(S-\frac{D}{L})e^{-\frac{H}{L}}B=\frac{L^2}{\alpha^2L^2-1}Ce^{-\alpha H}(S-\alpha D) \qquad [6]$$

From Eqs.[5] and [6],

$$M\begin{pmatrix}A\\B\end{pmatrix}=\begin{pmatrix}\frac{L^2}{\alpha^2L^2-1}Ce^{-\alpha H}(S-\alpha D)\\ p_{no}(e^{\frac{qV}{kT}}-1)+\frac{L^2}{\alpha^2L^2-1}C\end{pmatrix},$$

$$\text{where } M=\begin{pmatrix}(S+\frac{D}{L})e^{\frac{H}{L}} & (S-\frac{D}{L})e^{-\frac{H}{L}}\\ 1 & 1\end{pmatrix}$$

$$\begin{pmatrix}A\\B\end{pmatrix}=\frac{1}{\det M}\begin{pmatrix}1 & -(S-\frac{D}{L})e^{-\frac{H}{L}}\\ -1 & (S+\frac{D}{L})e^{\frac{H}{L}}\end{pmatrix}\begin{pmatrix}\frac{L^2}{\alpha^2L^2-1}Ce^{-\alpha H}(S-\alpha D)\\ p_{no}(e^{\frac{qV}{kT}}-1)+\frac{L^2}{\alpha^2L^2-1}C\end{pmatrix}$$

where $\det M=(S+\frac{D}{L})e^{\frac{H}{L}}-(S-\frac{D}{L})e^{-\frac{H}{L}}=S(e^{\frac{H}{L}}-e^{-\frac{H}{L}})+\frac{D}{L}(e^{\frac{H}{L}}+e^{-\frac{H}{L}})=2\{S\sinh(\frac{H}{L})+\frac{D}{L}\cosh(\frac{H}{L})\}$

$$(\det M)A=\frac{L^2}{\alpha^2L^2-1}Ce^{-\alpha H}(S-\alpha D)-p_{no}(e^{\frac{qV}{kT}}-1)(S-\frac{D}{L})e^{-\frac{H}{L}}-\frac{L^2}{\alpha^2L^2-1}C(S-\frac{D}{L})e^{-\frac{H}{L}})$$

$$(\det M)B=-\frac{L^2}{\alpha^2L^2-1}Ce^{-\alpha H}(S-\alpha D)+p_{no}(e^{\frac{qV}{kT}}-1)(S+\frac{D}{L})e^{\frac{H}{L}}+\frac{L^2}{\alpha^2L^2-1}C(S+\frac{D}{L})e^{\frac{H}{L}}$$

$$J_h(x=0) = -qD\frac{dp_n}{dx}\Big|_{x=0}、$$

$$\frac{J_h}{-qD} = \frac{1}{L}(A-B) + \frac{L^2\alpha}{\alpha^2L^2-1}C$$

$$(\det M)\times(A-B) = 2\frac{L^2}{\alpha^2L^2-1}Ce^{-\alpha H}(S-\alpha D) - p_{no}(e^{\frac{qV}{kT}}-1)\{(S-\frac{D}{L})e^{-\frac{H}{L}} + (S+\frac{D}{L})e^{\frac{H}{L}}\}$$

$$-\frac{L^2C}{\alpha^2L^2-1}\{(S-\frac{D}{L})e^{-\frac{H}{L}} + (S+\frac{D}{L})e^{\frac{H}{L}}\}$$

$$= 2\frac{L^2}{\alpha^2L^2-1}Ce^{-\alpha H}(S-\alpha D) - p_{no}(e^{\frac{qV}{kT}}-1)\{S(e^{\frac{H}{L}}+e^{-\frac{H}{L}}) + \frac{D}{L}(e^{\frac{H}{L}}-e^{-\frac{H}{L}})\}$$

$$-\frac{L^2C}{\alpha^2L^2-1}\{S(e^{\frac{H}{L}}+e^{-\frac{H}{L}}) + \frac{D}{L}(e^{\frac{H}{L}}-e^{-\frac{H}{L}})\}$$

$$= 2\frac{L^2}{\alpha^2L^2-1}Ce^{-\alpha H}(S-\alpha D) - 2p_{no}(e^{\frac{qV}{kT}}-1)\{S\cosh(\frac{H}{L}) + \frac{D}{L}\sinh(\frac{H}{L})\}$$

$$-2\frac{L^2C}{\alpha^2L^2-1}\{S\cosh(\frac{H}{L}) + \frac{D}{L}\sinh(\frac{H}{L})\}$$

$$= 2\frac{L^2}{\alpha^2L^2-1}Ce^{-\alpha H}(S-\alpha D) - 2\{p_{no}(e^{\frac{qV}{kT}}-1) + \frac{L^2C}{\alpha^2L^2-1}\}\{S\cosh(\frac{H}{L}) + \frac{D}{L}\sinh(\frac{H}{L})\}$$

$$\therefore A-B = \frac{\frac{L^2}{\alpha^2L^2-1}Ce^{-\alpha H}(S-\alpha D) - \{p_{no}(e^{\frac{qV}{kT}}-1) + \frac{L^2C}{\alpha^2L^2-1}\}\{S\cosh(\frac{H}{L}) + \frac{D}{L}\sinh(\frac{H}{L})\}}{S\sinh(\frac{H}{L}) + \frac{D}{L}\cosh(\frac{H}{L})}$$

$$J_h = -q\frac{D}{L}(A-B) - qD\frac{L^2\alpha}{\alpha^2L^2-1}C$$

$$= -q\frac{D}{L}\frac{\frac{L^2}{\alpha^2L^2-1}Ce^{-\alpha H}(S-\alpha D) - \{p_{no}(e^{\frac{qV}{kT}}-1) + \frac{L^2C}{\alpha^2L^2-1}\}\{S\cosh(\frac{H}{L}) + \frac{D}{L}\sinh(\frac{H}{L})\}}{S\sinh(\frac{H}{L}) + \frac{D}{L}\cosh(\frac{H}{L})} - qD\frac{L^2\alpha}{\alpha^2L^2-1}C$$

$$= q\frac{D}{L}p_{no}(e^{\frac{qV}{kT}}-1)\frac{S\cosh(\frac{H}{L}) + \frac{D}{L}\sinh(\frac{H}{L})}{S\sinh(\frac{H}{L}) + \frac{D}{L}\cosh(\frac{H}{L})}$$

$$-qD\frac{\frac{L}{\alpha^2L^2-1}Ce^{-\alpha H}(S-\alpha D) - \frac{LC}{\alpha^2L^2-1}\{S\cosh(\frac{H}{L}) + \frac{D}{L}\sinh(\frac{H}{L})\}}{S\sinh(\frac{H}{L}) + \frac{D}{L}\cosh(\frac{H}{L})} - qD\frac{L^2\alpha}{\alpha^2L^2-1}C$$

$$= q\frac{D}{L}p_{no}(e^{\frac{qV}{kT}}-1)\frac{\frac{SL}{D}\cosh(\frac{H}{L}) + \sinh(\frac{H}{L})}{\frac{SL}{D}\sinh(\frac{H}{L}) + \cosh(\frac{H}{L})}$$

$$-qD\frac{L}{\alpha^2L^2-1}C[\frac{e^{-\alpha H}(S-\alpha D)\frac{L}{D} - \{\frac{SL}{D}\cosh(\frac{H}{L}) + \sinh(\frac{H}{L})\}}{\frac{SL}{D}\sinh(\frac{H}{L}) + \cosh(\frac{H}{L})} + \alpha L]$$

$$J_h = q\frac{D}{L}p_{no}(e^{\frac{qV}{kT}}-1)\frac{\frac{SL}{D}\cosh(\frac{H}{L}) + \sinh(\frac{H}{L})}{\frac{SL}{D}\sinh(\frac{H}{L}) + \cosh(\frac{H}{L})}$$

$$-q\frac{L}{\alpha^2L^2-1}\times\alpha(1-R)\Phi_o e^{-\alpha(H_p+W)}\times[\alpha L + \frac{e^{-\alpha H}(\frac{SL}{D}-\alpha L) - \{\frac{SL}{D}\cosh(\frac{H}{L}) + \sinh(\frac{H}{L})\}}{\frac{SL}{D}\sinh(\frac{H}{L}) + \cosh(\frac{H}{L})}]$$

$$J_L^h = q\frac{L}{\alpha^2 L^2 - 1} \times \alpha(1-R)\Phi_o e^{-\alpha(H_p+W)} \times [\alpha L + \frac{e^{-\alpha H}(\frac{SL}{D} - \alpha L) - \{\frac{SL}{D}\cosh(\frac{H}{L}) + \sinh(\frac{H}{L})\}}{\frac{SL}{D}\sinh(\frac{H}{L}) + \cosh(\frac{H}{L})}$$

When $\frac{S}{\alpha D} << 1$,

$$J_L^h \approx q\frac{\alpha^2 L^2}{\alpha^2 L^2 - 1} \times (1-R)\Phi_o e^{-\alpha(H_p+W)} \times (1 - \frac{S}{\alpha D})(1 - e^{-\alpha H})$$

$$\approx q\frac{\alpha^2 L^2}{\alpha^2 L^2 - 1} \times (1-R)\Phi_o e^{-\alpha(H_p+W)}(1 - e^{-\alpha H})$$

The photocurrent due to photo-generated electrons and holes within the depletion region J_L^{SCR} can be express as:

$$J_L^{SCR} = q(1-R)\Phi_o e^{-\alpha H_p} \times (1 - e^{-\alpha W})$$

$$J_{total}^{front} = J_L^{SCR} + J_L^h = q\frac{\alpha^2 L^2}{\alpha^2 L^2 - 1} \times (1-R)\Phi_o e^{-\alpha(H_p+W)}(1 - e^{-\alpha H}) + q(1-R)\Phi_o e^{-\alpha H_p} \times (1 - e^{-\alpha W})$$

$$= q(1-R)\Phi_o e^{-\alpha H_p}(1 + \frac{e^{-\alpha W}}{\alpha^2 L^2 - 1})$$

when $\alpha L >> 1$, this mean that L is large enough,

$$J_{total}^{front} = q(1-R)\Phi_o e^{-\alpha H_p}$$

From the above result, we can understand that the following conditions should be satisfied in order to achieve large J_{total}^{front}

- $\alpha^2 L^2 >> 1$ In case of $BaSi_2$, this condition is satisfied when $L > 1$ μm since $\alpha > 3 \times 10^4 cm^{-1}$
- $L >> H$ (~2μm)
  The above two conditions request us to achieve L exceeding 10μm.
- $S/\alpha D << 1$, meaning that the interface recombination velocity should be as small as possible.

(2) Hole current due to photo generated holes in the *n*-region under illumination on the back side.

We suppose that the forward voltage V is applied due to the voltage drop at the load resistance.

(i) Realistic case, that is, $p_n(H)$ is determined by front-surface recombination velocity S,

The minority carrier (holes) $p_n(x)$ in the neutral n-type region (x>0) is given by,

$$D\frac{d^2 p_n}{dx^2} + G - \frac{p_n - p_{no}}{\tau} = 0,$$

$$\Phi(x) = (1-R)\Phi_o e^{-\alpha H} e^{\alpha x},$$

$$G = \alpha(1-R)\Phi_o e^{-\alpha(H+Hn)} e^{\alpha x}$$

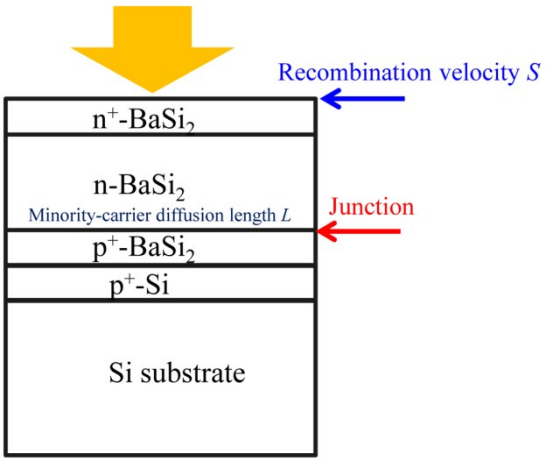

$$\frac{d^2\Delta p_n}{dx^2}+\frac{G}{D}-\frac{\Delta p_n}{\tau D}=\frac{d^2\Delta p_n}{dx^2}+Ce^{\alpha x}-\frac{\Delta p_n}{L^2}=0 \qquad [7]$$

where, $C=\dfrac{\alpha(1-R)\Phi_o}{D}e^{-\alpha(H+Hn)}$

The general solution of Eq.[7] is

$$\Delta p_n = Ae^{\frac{x}{L}} + Be^{-\frac{x}{L}} \qquad [8]$$

The particular solution of Eg.[7] is

$$\Delta p_n = Fe^{\alpha x} \qquad [9]$$

From Eqs.[7] and [9],

$$F(\alpha)^2+C-\frac{F}{L^2}=0、F=-\frac{L^2}{\alpha^2L^2-1}C$$

$$、p_n(x)=p_{no}+Ae^{\frac{x}{L}}+Be^{-\frac{x}{L}}-\frac{L^2}{\alpha^2L^2-1}Ce^{\alpha x} \qquad [10]$$

The above two undetermined A and B can be given by the following two boundary conditions.

$$At\ x=0, p_{no}(0)=p_{no}e^{\frac{qV}{kT}} \qquad (A)$$

$$At\ x=H, -D\frac{dp_n}{dx}=S(p_n-p_{no}) \qquad (B)$$

From the boundary condition (A),

$$p_{no}+A+B-\frac{L^2}{\alpha^2L^2-1}C=p_{no}e^{\frac{qV}{kT}}、A+B=p_{no}(e^{\frac{qV}{kT}}-1)+\frac{L^2}{\alpha^2L^2-1}C \qquad [11]$$

From the boundary condition (B),

$$\frac{dp_n}{dx}=\frac{1}{L}Ae^{\frac{x}{L}}-\frac{1}{L}Be^{-\frac{x}{L}}-\frac{\alpha L^2}{\alpha^2L^2-1}Ce^{\alpha x}$$

$$S(p_n-p_{no})=S(Ae^{\frac{H}{L}}+Be^{-\frac{H}{L}}-\frac{L^2}{\alpha^2L^2-1}Ce^{\alpha H})=-\frac{D}{L}(Ae^{\frac{H}{L}}-Be^{-\frac{H}{L}})+\frac{\alpha L^2D}{\alpha^2L^2-1}Ce^{\alpha H}$$

$$(S+\frac{D}{L})e^{\frac{H}{L}}A+(S-\frac{D}{L})e^{-\frac{H}{L}}B=\frac{L^2}{\alpha^2L^2-1}Ce^{\alpha H}(S+\alpha D) \qquad [12]$$

From Eqs.[11] and [12],

$$M\begin{pmatrix}A\\B\end{pmatrix}=\begin{pmatrix}\dfrac{L^2}{\alpha^2L^2-1}Ce^{\alpha H}(S+\alpha D)\\ p_{no}(e^{\frac{qV}{kT}}-1)+\dfrac{L^2}{\alpha^2L^2-1}C\end{pmatrix},$$

$$\text{where } M=\begin{pmatrix}(S+\dfrac{D}{L})e^{\frac{H}{L}} & (S-\dfrac{D}{L})e^{-\frac{H}{L}}\\ 1 & 1\end{pmatrix}$$

$$\begin{pmatrix}A\\B\end{pmatrix}=\frac{1}{det\,M}\begin{pmatrix}1 & -(S-\dfrac{D}{L})e^{-\frac{H}{L}}\\ -1 & (S+\dfrac{D}{L})e^{\frac{H}{L}}\end{pmatrix}\begin{pmatrix}\dfrac{L^2}{\alpha^2L^2-1}Ce^{\alpha H}(S+\alpha D)\\ p_{no}(e^{\frac{qV}{kT}}-1)+\dfrac{L^2}{\alpha^2L^2-1}C\end{pmatrix}$$

Where, $det\,M=(S+\frac{D}{L})e^{\frac{H}{L}}-(S-\frac{D}{L})e^{-\frac{H}{L}}=S(e^{\frac{H}{L}}-e^{-\frac{H}{L}})+\frac{D}{L}(e^{\frac{H}{L}}+e^{-\frac{H}{L}})=2\{S\sinh(\frac{H}{L})+\frac{D}{L}\cosh(\frac{H}{L})\}$

$$(det\,M)A=\frac{L^2}{\alpha^2L^2-1}Ce^{\alpha H}(S+\alpha D)-p_{no}(e^{\frac{qV}{kT}}-1)(S-\frac{D}{L})e^{-\frac{H}{L}}-\frac{L^2}{\alpha^2L^2-1}C(S-\frac{D}{L})e^{-\frac{H}{L}})$$

$$(det\,M)B=-\frac{L^2}{\alpha^2L^2-1}Ce^{\alpha H}(S+\alpha D)+p_{no}(e^{\frac{qV}{kT}}-1)(S+\frac{D}{L})e^{\frac{H}{L}}+\frac{L^2}{\alpha^2L^2-1}C(S+\frac{D}{L})e^{\frac{H}{L}}$$

$J_h(x=0)=-qD\left.\frac{dp_n}{dx}\right|_{x=0}$、

$$\frac{J_h}{-qD}=\frac{1}{L}(A-B)-\frac{L^2\alpha}{\alpha^2L^2-1}C$$

$$(det\,M)\times(A-B)=2\frac{L^2}{\alpha^2L^2-1}Ce^{\alpha H}(S+\alpha D)-p_{no}(e^{\frac{qV}{kT}}-1)\{(S-\frac{D}{L})e^{-\frac{H}{L}}+(S+\frac{D}{L})e^{\frac{H}{L}}\}$$

$$-\frac{L^2C}{\alpha^2L^2-1}\{(S-\frac{D}{L})e^{-\frac{H}{L}}+(S+\frac{D}{L})e^{\frac{H}{L}}\}$$

$$=2\frac{L^2}{\alpha^2L^2-1}Ce^{\alpha H}(S+\alpha D)-p_{no}(e^{\frac{qV}{kT}}-1)\{S(e^{\frac{H}{L}}+e^{-\frac{H}{L}})+\frac{D}{L}(e^{\frac{H}{L}}-e^{-\frac{H}{L}})\}$$

$$-\frac{L^2C}{\alpha^2L^2-1}\{S(e^{\frac{H}{L}}+e^{-\frac{H}{L}})+\frac{D}{L}(e^{\frac{H}{L}}-e^{-\frac{H}{L}})\}$$

$$=2\frac{L^2}{\alpha^2L^2-1}Ce^{\alpha H}(S+\alpha D)-2p_{no}(e^{\frac{qV}{kT}}-1)\{S\cosh(\frac{H}{L})+\frac{D}{L}\sinh(\frac{H}{L})\}$$

$$-2\frac{L^2C}{\alpha^2L^2-1}\{S\cosh(\frac{H}{L})+\frac{D}{L}\sinh(\frac{H}{L})\}$$

$$=2\frac{L^2}{\alpha^2L^2-1}Ce^{\alpha H}(S+\alpha D)-2\{p_{no}(e^{\frac{qV}{kT}}-1)+\frac{L^2C}{\alpha^2L^2-1}\}\{S\cosh(\frac{H}{L})+\frac{D}{L}\sinh(\frac{H}{L})\}$$

$$\therefore A-B=\frac{\frac{L^2}{\alpha^2L^2-1}Ce^{\alpha H}(S+\alpha D)-\{p_{no}(e^{\frac{qV}{kT}}-1)+\frac{L^2C}{\alpha^2L^2-1}\}\{S\cosh(\frac{H}{L})+\frac{D}{L}\sinh(\frac{H}{L})\}}{S\sinh(\frac{H}{L})+\frac{D}{L}\cosh(\frac{H}{L})}$$

$$J_h = -q\frac{D}{L}(A-B)+qD\frac{L^2\alpha}{\alpha^2L^2-1}C$$

$$= -q\frac{D}{L}\frac{\frac{L^2}{\alpha^2L^2-1}Ce^{\alpha H}(S+\alpha D)-\{p_{no}(e^{\frac{qV}{kT}}-1)+\frac{L^2C}{\alpha^2L^2-1}\}\{S\cosh(\frac{H}{L})+\frac{D}{L}\sinh(\frac{H}{L})\}}{S\sinh(\frac{H}{L})+\frac{D}{L}\cosh(\frac{H}{L})}+qD\frac{L^2\alpha}{\alpha^2L^2-1}C$$

$$= q\frac{D}{L}p_{no}(e^{\frac{qV}{kT}}-1)\frac{S\cosh(\frac{H}{L})+\frac{D}{L}\sinh(\frac{H}{L})}{S\sinh(\frac{H}{L})+\frac{D}{L}\cosh(\frac{H}{L})}$$

$$-qD\frac{\frac{L}{\alpha^2L^2-1}Ce^{\alpha H}(S+\alpha D)-\frac{LC}{\alpha^2L^2-1}\{S\cosh(\frac{H}{L})+\frac{D}{L}\sinh(\frac{H}{L})\}}{S\sinh(\frac{H}{L})+\frac{D}{L}\cosh(\frac{H}{L})}+qD\frac{L^2\alpha}{\alpha^2L^2-1}C$$

$$= q\frac{D}{L}p_{no}(e^{\frac{qV}{kT}}-1)\frac{\frac{SL}{D}\cosh(\frac{H}{L})+\sinh(\frac{H}{L})}{\frac{SL}{D}\sinh(\frac{H}{L})+\cosh(\frac{H}{L})}$$

$$-qD\frac{L}{\alpha^2L^2-1}C[\frac{e^{\alpha H}(S+\alpha D)\frac{L}{D}-\{\frac{SL}{D}\cosh(\frac{H}{L})+\sinh(\frac{H}{L})\}}{\frac{SL}{D}\sinh(\frac{H}{L})+\cosh(\frac{H}{L})}-\alpha L]$$

$$J_h = q\frac{D}{L}p_{no}(e^{\frac{qV}{kT}}-1)\frac{\frac{SL}{D}\cosh(\frac{H}{L})+\sinh(\frac{H}{L})}{\frac{SL}{D}\sinh(\frac{H}{L})+\cosh(\frac{H}{L})}$$

$$-q\frac{L}{\alpha^2L^2-1}\times\alpha(1-R)\Phi_o e^{-\alpha(H+H_n)}\times[\frac{e^{\alpha H}(\frac{SL}{D}+\alpha L)-\{\frac{SL}{D}\cosh(\frac{H}{L})+\sinh(\frac{H}{L})\}}{\frac{SL}{D}\sinh(\frac{H}{L})+\cosh(\frac{H}{L})}-\alpha L]$$

$$J_L^{back} = q\frac{L}{\alpha^2L^2-1}\times\alpha(1-R)\Phi_o e^{-\alpha(H+H_n)}\times[\frac{e^{\alpha H}(\frac{SL}{D}+\alpha L)-\{\frac{SL}{D}\cosh(\frac{H}{L})+\sinh(\frac{H}{L})\}}{\frac{SL}{D}\sinh(\frac{H}{L})+\cosh(\frac{H}{L})}-\alpha L]$$

When $L >> H$ and $S/\alpha D << 1$ are satisfied,

$$J_L^{back} \approx q\frac{\alpha^2L^2}{\alpha^2L^2-1}\times(1-R)\Phi_o e^{-\alpha(H+H_n)}\times(1+\frac{S}{\alpha D})(e^{\alpha H}-1)$$

$$\approx q\frac{\alpha^2L^2}{\alpha^2L^2-1}\times(1-R)\Phi_o e^{-\alpha H_n}\{1-e^{-\alpha H}\}$$

The photocurrent due to photo generated electron hole pair in the depletion region J_L^{SCR} is express as,

$$J_L^{SCR} = q(1-R)\Phi_o e^{-\alpha(H+H_n)}\times(1-e^{-\alpha W})$$

$$J_{total}^{back} = J_L^{SCR}+J_L^{h} = q\frac{\alpha^2L^2}{\alpha^2L^2-1}\times(1-R)\Phi_o e^{-\alpha H_n}(1-e^{-\alpha H})+q(1-R)\Phi_o e^{-\alpha(H+H_n)}\times(1-e^{-\alpha W})$$

$$= q(1-R)\Phi_o e^{-\alpha H_n}\times\{\frac{\alpha^2L^2}{\alpha^2L^2-1}(1-e^{-\alpha H})+e^{-\alpha H}(1-e^{-\alpha W})\}$$

$$\approx q(1-R)\Phi_o e^{-\alpha H_n}\times\frac{\alpha^2L^2}{\alpha^2L^2-1}(1-\frac{e^{-\alpha H}}{\alpha^2L^2}) = q(1-R)\Phi_o e^{-\alpha H_n}\times(1+\frac{1-e^{-\alpha H}}{\alpha^2L^2-1})$$

Since $H\sim$2μm and $\alpha > 3\times10^4$cm^{-1} , thus $1-e^{-\alpha H}\approx 1$.

Just for your information, J_{total}^{front} is given by,

$$J_{total}^{front} = q(1-R)\Phi_o e^{-\alpha H_p}(1+\frac{e^{-\alpha W}}{\alpha^2L^2-1})$$

BIBLIOGRAPHY

[1] J. Evers, G. Oehlinger, A. Weiss, Angew. Chem. Int. Ed. 16 (1977) 659.

[2] M. Imai, T. Hirano, J. Alloys Compd. 224 (1995) 111.

[3] D. B. Migas, V. L. Shaposhnikov, V. E. Borisenko, Phys. Status Solidi B 244 (2007) 2611.

[4] K. Morita, Y. Inomata, T. Suemasu, Thin Solid Films 508 (2006) 363.

[5] K. Toh, T. Saito, T. Suemasu, Jpn. J. Appl. Phys. 50 (2011) 068001.

[6] S. M. Sze. *Semiconductor devices; Physics and Technology,* 2nd Edition (2001).

[7] C. H. Henry, J. Appl. Phys. 51 (1980) 4494.

[8] K. Morita, Y. Inomata, T. Suemasu, Jpn. J. Appl. Phys. 45 (2006) L390.

[9] Y. Imai, A. Watanabe, Thin Solid Films 515 (2007) 8219.

[10] R. A. McKee, F. J.Walker, J. R. Conner, R. Raj, Appl. Phys. Lett. 63 (1993) 2818.

[11] M. Imai, T. Hirano, Phys. Rev. B 58 (1998) 11922.

[12] Y. Inomata, T. Nakamura, T. Suemasu, F. Hasegawa, Jpn. J. Appl. Phys. 43 (2004) 4155.

[13] F. Alharbi, J. D. Bass, A. Salhi, A. Alyamani, Ho-Cheol Kim, R. D. Miller, Renewable Energy 36 (2011) 2753.

[14] Y. Matsumoto, D. Tsukada, R. Sasaki, M. Takeishi, T. Suemasu, Appl. Phys. Express 2 (2009) 021101.

[15] D. Tsukada, Y.Matsumoto, R. Sasaki, M. Takeishi, T. Saito, N. Usami, T. Suemasu, Appl. Phys. Express 2 (2009) 051601.

[16] Weijie Du, Mitsushi Suzuno, M. Ajmal Khan, Katsuaki Toh, Masakazu Baba, Appl. Phys. Lett.100 (2012)152114.

[17] Y. Imai, A. Watanabe, Intermetallics 15 (2007) 1291.

[18] M. Kobayashi, K. Morita, T. Suemasu, Thin Solid Films 515 (2007) 8242.

[19] M. Kobayashi, Y. Matsumoto, Y. Ichikawa, D. Tsukada, T. Suemasu, Appl. Phys. Express 1 (2008) 051403.

[20] M. Takeishi, Y. Matsumoto, R. Sasaki, T. Saito, T. Suemasu, Physics Procedia 11 (2011) 27.

[21] Gabriela Bunea, SunPower Corporation, Oct, 2003.

[22] BP, "Statistical review of world energy." 2010.

[23] IPCC Third Assessment Report Climate Change 2001.

[24] US Environmental Protection Agency, 2012.

[25] Tom Burnett, "*Hawai'i News Daily"*. 28 March 2011.

[26] C. J. Campbell, "*World Oil Resources"*, Dec 2000.

[27] Presentation by LG company, PVSEC 2011, 21st International Photovoltaic Science and Engineering Conference (PVSEC-21)-2011, Fukouka, Japan.

[28] Sakurai, "*Blue Backs*", Japan, 2001.

[29] Hara *et al*., Jpn. J. Appl. Phys.50 (2011)121202.

[30] H. J. Gossmann, F. C. Unterwald, and H.S. Luftman, J. Appl. Phys. 73 (1993) 8237.

[31] H. Jorke, *Surf. Sci*. 193 (1988) 569.

[32]. D. J. Chadi, P.H. Citrin, C.H. Park, D.L. Adler, M.A. Marcus and H. J. Gosmann, Phys. Rev. Lett. 79(1997) 4834.
[33] O. D. Dubon, P.G. Evans, J.F. Chervinsky, M.J. Aziz, F. Spaepen, M. F. Chisholm, and D. A. Muller, Appl. Phys. Lett. 78 (2001) 1505.
[34] D. Nobili, "*EMIS Data Review"*, (1987), p.384, 394, 410.
[35] R. B. Fair, *in Impurity Doping Processes in Silicon*, Ed. F.F.Y. Wang (North Holland, Amsterdam, The Netherlands, 1981) p. 342, 344.
[36] L. Esaki, Phys. Rev. 109 (1958) 603.
[37] Chynoweth *e. al.,* PR. 121 (1961) 684. 22
[38] T. Suemasu, T. Saito, K. Toh, A. Okada and, M. Ajmal Khan, Thin Solid Films 519 (2011) 8501.
[39] M. Ajmal Khan, M. Takeishi, Y. Matsumoto, T. Saito, and T. Suemasu, Physics Procedia 11 (2011) 11.
[40] M. Ajmal Khan, T. Saito, M. Takeishi, T. Suemasu, Advanced Materials Research (Advanced Materials for Applied Science and Technology) 326 (2011) 139.
[41] K. Toh, K.O. Hara, N. Usami, N. Saito, N. Yoshizawa, K. Toko, T. Suemasu, J. Crystal Growth 345(2012) 16.
[42] Y. Inomata, T. Nakamura, T. Suemasu, F. Hasegawa, Japanese Journal of Applied Physics 43 (2004) L478.
[43] Chen, T. Sekiguchi, D. Yang, F. Yin, K. Kido, S. Tsurekawa, Journal of Applied Physics 96 (2004) 5490.
[44] M. Baba, K.Toh, K. Toko, N. Saito, N. Yoshizawa, K. Jiptner, T. Sekiguchi, K.O. Hara, N. Usami, T. Suemasu, J. Crystal Growth 345 (2012) 16.
[45]S. J. Pearton, K. D. Cummings, and G. P. Vellacoleiro, J. Appl. Phys. 58, 3252 (1985).
[46]T. H. Huang, H. Kinoshita, and D. L. Kwong, Appl. Phys. Lett. **65**, 1829 (1994).
[47] H. J. Yu, L. McCarthy, H. Xing, H. Waltereit, L. Shen, S. Keller, S. P. Denbaars, J. S. Speck, and U. K. Mishra, Appl. Phys. Lett. **85**, 5254 (2004).
[48]K. K. Kim, S. Niki, J. Y. Oh, J. O. Song, T. Y. Seong, S. J. Park, S. Fujita, and S. W. Kim, J. Appl. Phys. **97**, 066103 (2005).
[49] Nishimura, PRL., vol. 138, no. 3A, p-A815-A821, 1965
[50] A. L. Efros, B.I. Shklovskii, J. Phys. C8 (1975) L49.
[51] Shklovskii, and Efros., Springer, Berlin, 1984.
[52] A. L. Efros, J. Phys. C: Solid State Phys. 9 (1976) 2021.
[53] K. Yamaguchi, H. Tomioka, T. Yui, T. Suemasu, K. Ando, R. Yoshizaki, F. Hasegawa, Phys. Status Solidi C 2 (2005) 2488.
[54] E. Arushanov, K.G. Lisunov, H. Vinzelberg, G. Behr, J. Schumann, O.G. Schmidt, J. Appl. Phys. 104 (2008) 053720.
[55] T. Nakamura *et al.*: Appl. Phys. Lett. 81 (2002) 1032.
[56] M. Imai *et al.*: Intermetallics 18 (2010) 548.

[57] R. Swanepoel: J. Phys. E 16 (1983) 1214.
[58] T. Suemasu *et al*., J. Cryst. Growth 301–302 (2007) 680.
[59] L. J. Van Der Pauw, Philips Research Reports 20, 220 (1958) 34.
[60] M. Ajmal Khan, T. Saito, K. Nakamura, M. Baba, W. Du, K. Toh, K. Toko, and T. Suemasu, Thin Solid Films 522, 95 (2012).
[61] K. Nakamura, M. Baba, M. Ajmal Khan, W. Du, K. Toko, and T. Suemasu, Journal of Applied Physics 113 (2013) 05311.